



**Politecnico
di Torino**

Politecnico di Torino

Corso di Laurea in Ingegneria Aerospaziale

A.a. 2024/2025

Sessione di Laurea Marzo/Aprile 2025

Double-Hybrid Powertrain Modelling and Integration in the Conceptual Design Method

Relatori:

Prof. Paolo Maggiore
Dr. Alexander Heidebrecht
Dr. Francesco Orefice

Candidato:

Alessandro Borgia

Double-Hybrid Powertrain Modelling and Integration in the Conceptual Design Method



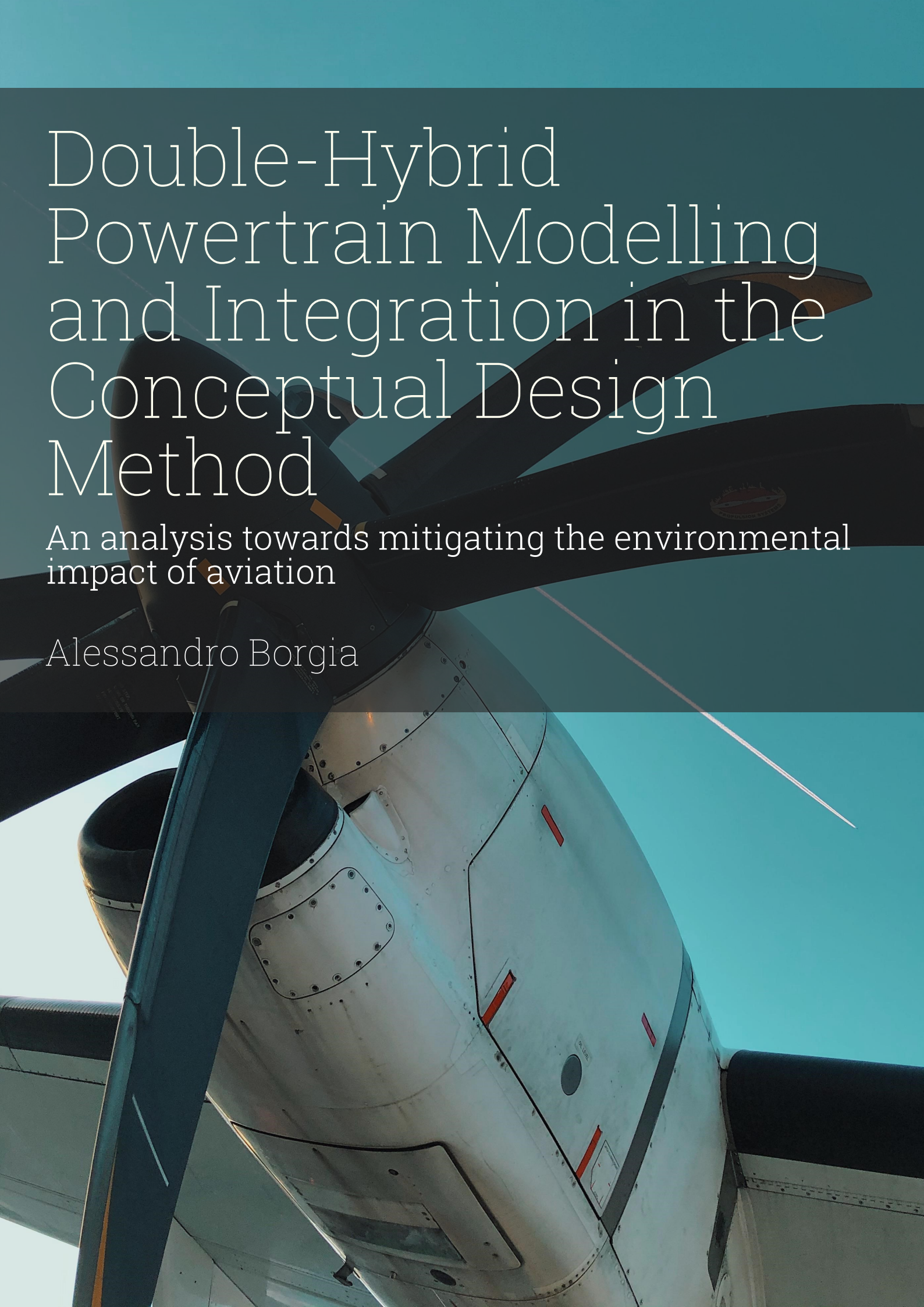
**Politecnico
di Torino**

An analysis towards mitigating the
environmental impact of aviation

by

Alessandro Borgia

Supervisors: P. Maggiore, A. Heidebrecht
Co-supervisor: F. Orefice
Academic year: 2024-2025



Double-Hybrid Powertrain Modelling and Integration in the Conceptual Design Method

An analysis towards mitigating the environmental
impact of aviation

Alessandro Borgia

Preface

*E siamo arrivati qui,
se stai leggendo questa pagina vuol dire che è successo davvero,
mi sono laureato!*

Con questa tesi si conclude il mio percorso al Politecnico. Sono stati anni ricchi di soddisfazioni, gioie ma anche di ansie e paure. Vorrei dedicare queste pagine alle persone che mi hanno accompagnato e senza le quali tutto questo non sarebbe stato possibile.

Vorrei iniziare questa pagina di ringraziamenti dal mio relatore al Politecnico di Torino, il Professor Paolo Maggiore. Oltre ad essere stato il docente di numerosi corsi, è stato senza dubbio il mio riferimento accademico degli ultimi anni. Non posso che esserle grato per la sua infinita disponibilità (soprattutto per le idee più "matte") e, soprattutto, per la sua fiducia riposta in me.

A huge thank you to Dr. Alexander Heidebrecht and Dr. Francesco Orefice, my supervisors at TU Delft during this thesis. First of all, I can't be more grateful to you for your welcome, your guidance and consideration. It really means a lot to me. Every meeting was a true occasion to learn something about aircraft design. Thanks also to Francesca for accepting me at TU almost a year ago and to Maurice for his advice on the Initiator.

Ai miei genitori, per il loro amore incondizionato e per avermi trasmesso la loro virtù più grande: il senso del dovere. Senza di voi questo percorso non sarebbe stato possibile. Grazie per i vostri pacchi da sù durante il periodo a Delft, che mi hanno fatto sentire a casa pur stando lontano.

Amici

Grazie a Giuliano, praticamente mio fratello, per essermi vicino da sempre (chiaramente tu sulla destra essendo mancino, ed io sulla sinistra essendo destro).

Matilde, grazie per avermi "adottato" a Porta Nuova il primo giorno di Università. Sei stata la mia prima vicina di banco al Poli e la prima (e ultima) persona celiaca che abbia mai "avvelenato". Grazie per esserci sempre.

Grazie a Micol per essere io stato l'eccezione del tuo odio (completamente giustificato) per gli aerospaziali, per essere la mia fashion personal advisor e per non smettere di starmi accanto anche con 6 ore di fuso e tanti chilometri a separarci.

A Marco e Riccardo per avere compiuto insieme fin da quando eravamo bambini ogni passo. Mi sembra assurdo che alle medie parlavamo di diventare ingegneri aerospaziali e ora ci siamo riusciti.

A proposito di questa tesi, ci tengo a dire un grazie a tutti i miei amici durante il periodo in Olanda, che in questi 6 mesi mi avete fatto anche da famiglia. Ad Ardemia per essere venuta ad Aerospaziale solo una volta ma con la tempesta. A Leo per tutti i caffè al tredicesimo piano e per aver fatto uno dei tiramisù più buoni che abbia mai mangiato. A Domenico per i pessimi gusti musicali che però si compensano con il tuo grande cuore. A Sofia grazie per avermi rubato la casa lo scorso anno ma averla poi resa il luogo di tante cene insieme. Spettegolare con te è di un altro livello. Ad Antonio grazie per essere venuto da Napoli per poter essere qui oggi. Alla tua ironia e al tuo ragù. Ad Edoardo per essere stato il mio gym bro e a Francesco per avermi condiviso il Raymer 30 secondi dopo avermi conosciuto. Un grazie va anche a tutti gli altri che mi sono stati accanto in questi mesi: Michelino, Michelone, Viola, Giacomo e Alissa.

Grazie ai miei amici di corso per avermi spronato e per aver condiviso insieme una quantità smisurata di insulti e auguri di scarsa forma fisica ad un discreto numero di professori. Grazie ad Antonio per i suoi consigli, ad Ilaria per la sua sensibilità, ad Achille per le partite a FIFA insieme, a Roberto e Alice per aver reso le lezioni un momento più divertente ed ad Alessio per essersi sorbito Astos.

Vorrei ringraziare tutti i ragazzi del Progetto RA del Team Icarus. Qui ho lasciato un pezzo di cuore dei miei anni al Politecnico. Con voi sono cresciuto come ingegnere, ma prima di tutto come persona. Tommaso, per essere stato non solo il vice che tutti vorrebbero avere, ma un amico con cui ho condiviso tanto. Grazie ad Angelo, Andrea, Alfredo, Luca, Maura, Fabrizio, Giovanni, Gilbert, Stefano Marco Giolo e Pietro per i momenti passati insieme. Infine grazie ad Ale Ercole, Ale D'Addosio, Diego per i sabati mattina insieme e per avermi insegnato per primi cosa fosse l'aerodinamica.

Grazie a chi c'è stato e ci sarà, o chi è passato anche solo per un piccolo periodo.

Con affetto,

Alessandro Borgia
Torino, 3 Aprile 2025

Summary

Achieving carbon net neutrality in aviation by 2050, as targeted by the Green Deal, necessitates the development of new propulsive technologies in respect to conventional kerosene-fuelled aircraft. This thesis explores novel hybrid powertrain solutions, introducing a threefold energy source powertrain, named the Double-Hybrid Powertrain Model. This powertrain aims to combine kerosene, hydrogen (used in both fuel cells and combustion) and battery and shall be integrated within the Conceptual Design Method. The resulting system is characterised by fourteen power flows and requires four power control parameters to be mathematically described. Double-Hybrid powertrain is then used for a regional aircraft case-study, exploring the power control parameters design space in a only cruise mission scenario. The results indicate that a power split characterised by fuel cells (80-90% of total energy), in conjunction with either a small battery or limited kerosene combustion, offers significant potential for reducing both total energy consumption and environmental impact. This is due to the higher efficiency of fuel cells compared to gas turbine engines. This configuration also shows promise for improved responsiveness to power transients and the possibility of cruise-optimized fuel cell sizing. While hydrogen combustion alone results in a slightly higher energy consumption than conventional kerosene-powered aircraft. This is caused by the additional weight related to the hydrogen storage, even with comparable take-off mass. Ultimately, a fully battery-electric aircraft is projected to be substantially heavier and require significantly more energy, even with a higher overall powertrain efficiency, unless substantial and currently unforeseen improvements in battery energy density are realised.

Contents

Preface	i
Summary	iii
Nomenclature	ix
1 Introduction	1
2 Hybrid-Electric Propulsion	3
2.1 Powertrain Architectures	3
2.2 Degree of Hybridization and Power Control Parameters	4
2.2.1 Degree of Hybridization	4
2.2.2 Power Control Paramters for Battery Electric Aircraft	7
2.3 Relevant Examples	9
2.3.1 Parallel Architecture	9
2.3.2 Turboelectric Architecture	11
2.4 All Electric Architecture	12
3 Study Objective	14
4 Fundamental of Hybrid Powertrain Components	15
4.1 Turboprop Engine	15
4.2 Fundamental of Hydrogen Combustion	17
4.3 Hydrogen Tank	20
4.4 Working Principles and Sizing of Fuel Cells	24
5 Double-Hybrid Powertrain Modelling	27
5.1 Architectures and Configurations	27
5.2 Operating Modes	32
5.3 Threefold Energy Storage Powertrain Descriptors	36
5.3.1 Power Control Parameters	36
5.3.2 Energy Control Parameters	36
5.4 Power Control Parameters along the Operating Modes	37
5.4.1 Battery Being Recharged	37
5.4.2 Engine Windmilling	40
5.5 Powertrain Equations	42
5.6 Powertrain Input Scenario	46
6 Conceptual design synthesis for a double hybrid aircraft	50
6.1 Matching Chart and Constraint Diagrams	50
6.2 Mission Analysis	52
6.3 Weight Estimation	53
7 Verification of the Double-Hybrid Conceptual Design Model	60
8 Emission Estimation Metodolody	63
8.1 Kerosene Combustion	63
8.1.1 Boeing Fuel Flow Method 2	64
8.1.2 Hydrogen Emissions	65
8.2 Emissions for Turboprop Engine	66
8.3 Cumulative Emissions Estimation	67
9 Double-Hybrid Sensitivity Analysis for a Regional Aircraft Application	68
9.1 TLAR and Powertrain Input Parameters	69

9.2 Power Ratio Design Space Analysis	70
10 Analysis of Future Trends for Double-Hybrid Aircraft Drivers	78
10.1 Brake Specific Fuel Consumption	78
10.2 Fuel Cell Efficiency	80
10.3 Battery Specific Energy	81
10.4 Gravimetric Index	82
11 Conclusion and Future Development	84
References	86

List of Figures

1.1	Projection of CO ₂ emissions from aviation. Source: [23]	1
1.2	CO ₂ emissions per segment and range. Source: [13]	2
1.3	Comparison of new technology and sustainable aviation fuels and new technologies. Source: [13]	2
1.4	Comparison of climate impact from H2 propulsion and synfuel. Source: [13]	2
2.1	Battery-electric propulsion architectures. Source: [50]	5
2.2	Example Representation of Parameter ω Over Flight Period (Source: [28])	6
2.3	Example of a Degree-of-Hybridization Trade Study Conducted for a Hypothetical Hybrid-Electric System Based on Kerosene and Batteries as Energy Carriers. Source: [28]	7
2.4	SUGAR propulsion group. Source: [4]	9
2.5	Amber propulsion system. Source: [11]	11
2.6	STARC ABL render in OpenVSP. Source:[51]	12
2.7	SkySpark configuration. Source: [45]	12
2.8	SkySpark electric bus. Source [45]	13
2.9	Universal Hydrogen propulsion system model. Source: [26]	13
4.1	Gas turbine engine on-design performance at sea level conditions. Souce: [25]	16
4.2	Turboprop off-design performance. Souce: [25]	16
4.3	Gas turbine engine performance at various throttle settings. Souce: [25]	17
4.4	Temperature Characteristics of a Combustor. Source [5]	18
4.5	Changes in combustion gas properties when using hydrogen. Source: [47]	19
4.6	Fuel tank structural arrangement [22]	21
4.7	Tank structure for the multi layer insulation. Source [7]	22
4.8	Tank integration onto aircraft structred proposed by Montellanp. Source: [37]	23
4.9	Gravimetric efficiency of a single tank option for a regional airliner [48]	24
4.10	PEM fuel cell diagram. Source: [14]	25
4.11	Fuel cell system architecture. Source: [32]	25
4.12	Fuel cell system efficiency curves as a function of power output. Source: [10]	26
5.1	Configurations 1-8	29
5.2	Configurations 9-16	30
5.3	Configurations 17-24	31
5.4	Configurations 25-28	32
5.5	Operating modes 1-6	34
5.6	Operating modes 7-10. The red rectangle represent an addition possible operating mode respect to the current literature	35
5.7	Qualitative graph of $\Phi_{Bat} = f(P_{Bat})$ in OM5 and OM10. a is assumed greater than 1 and b is positive.	38
5.8	Qualitative graph of $\Phi_{H2} = f(P_{Bat})$ in OM5 and OM10.	39
5.9	Qualitative graph of $\Phi_{Bat} = f(P_{Bat})$ in OM3, OM6, OM8, OM9. k is assumed positive.	39
5.10	Qualitative graph of $\Phi_{H2} = f(P_{Bat})$ in OM3, OM6, OM8, OM9. k is assumed positive.	40
5.11	Qualitative graph of $\varphi = f(P_{s2})$ in OM1 to OM6 and OM10. P_{s1} is assumed positive.	41
5.12	Qualitative graph of $\varphi(P_{s2})$ in OM7 to OM9. P_{s1} is assumed negative.	41
6.1	Flowchart of the conceptual design (Class 1) module. The outputs and inputs of the method are highlighted.	51
6.2	Methodology to derive the components' constraint diagram from the aircraft matching chart	52
6.3	Payload-range diagram for double-hybrid aircraft	53

6.4	Mission Analysis and Weight estimation flow chart	54
6.5	Segment mission analysis	55
6.6	Effect of EM/TOM fraction on the mass and mass breakdown of a 75 passenger single-aisle aircraft.	57
6.7	Weight estimation loop flowchart	59
8.1	Graphical representation of the Boeing Fuel Flow Method 2 steps to correlate in flight EI to reference conditions EI	64
8.2	EINO _x depending on throttle setting for PW150A engine	67
9.1	Graphical representation of power ratio design space for a Double-Hybrid Powertrain	68
9.2	Parallel powertrain configuration employed in this study	69
9.3	Total propulsive power constraint diagram	69
9.4	TOM results for varying H ₂ split fractions	71
9.5	Wing span for varying H ₂ split fractions	72
9.6	ZFM results for varying H ₂ split fractions	72
9.7	Effect of η_{PT}/TOM on total energy consumption	73
9.8	Total energy consumption results for varying H ₂ split fractions (normalised to the energy consumption for conventional kerosene aircraft)	74
9.9	Energy mass fraction results for varying H ₂ split fractions	74
9.10	Kerosene consumption results for varying H ₂ split fractions (normalised to the kerosene consumption for conventional kerosene aircraft)	75
9.11	NO _x emissions result for varying H ₂ split fractions (normalised to NO _x emissions for conventional kerosene aircraft)	76
9.12	Cumulative emissions results for varying H ₂ split fractions (normalised to the emissions for conventional kerosene aircraft)	77
10.1	Block fuel trend in the last 50 years for kerosene aircraft. Source: [54]	78
10.2	Total energy consumption minimum points- depending on brake specific fuel consumption - represented in power control parameters diagram	79
10.3	KPIs variation depending on BSFC, respect to $BSFC = 294 \text{ g/kWh}$	79
10.4	Total energy consumption minimum points- depending on fuel cell efficiency - represented in power control parameters diagram	80
10.5	KPIs variation depending on Fuel cell efficiency, respect to $\eta_{FC} = 50\%$	80
10.6	Specific Energy [Wh/kg] trend of EV Lithium-Ion Batteries (Blue line) from literature data (Orange dots). Source: [40]	81
10.7	Total energy consumption minimum points- depending on battery specific energy - represented in power control parameters diagram	81
10.8	KPIs variation depending on Battery Specific Energy, respect to $SE_{Bat} = 340 \text{ Wh/kg}$	82
10.9	Total energy consumption minimum points- depending on gravimetric index of the hydrogen fuel system- represented in power control parameters diagram	82
10.10	KPIs variation depending on Gravimetric Index, respect to $GI = 0.35$	83

List of Tables

2.1	Control Parameters for Different Powertrain Configurations	8
2.2	Powertrain equations. Source: [50]	8
2.3	Comparison of conventional aircraft, SUGAR High, Balanced configuration(Ref Hp 1750), and Core Shutdown Configuration (Ref Hp 7150). Source: [4]	11
4.1	Allowance for different components	21
4.2	Gravimetric indexes for the components of the electric propulsion system.	26
5.1	Number of possible configuration for each type of powertrain architecture	28
5.2	Operational Modes Associated with Aircraft Configurations	33
5.3	Power Control Parameters Range during Nominal Conditions (OM1, OM4)	37
5.4	Control Parameters for Operating Modes 1-4	42
5.5	Power Control Parameters for Operating Modes 5-7	42
5.6	Power Control Parameters for Operating Modes 8-10	42
5.7	Powertrain Equations for Extended Powertrain System	43
5.8	Power Control Parameters for Operating Modes 1-4	48
5.9	Power Control Parameters for Operating Modes 5-7	48
5.10	Power Control Parameters for Operating Modes 8-10	49
6.1	Coefficient for estimating OEM. Source:[46]	56
6.2	Fuselage Diameter and Weight per Meter based on Payload	58
7.1	TLAR of DO-228NG	60
7.2	Comparison among the three design methods	61
7.3	TLAR for hydrogen combustion aircraft	61
7.4	Comparison among the two design methods for hydrogen combustion aircraft	61
7.5	TLAR of battery-electric aircraft	62
7.6	Comparison among the two design methods for battery-electric aircraft	62
8.1	Emission Indices for Proportional Chemical Emissions	63
8.2	ICAO Standard for LTO Cycle Operating Mode Thrust Setting and Duration	64
8.3	Correction Factor Applied to Thrust Setting (BFFM2)	64
8.4	Emission Indices for Water	65
8.5	Throttle setting definition in LTO Cycle for Turboprop Engine	66
8.6	Predicted emission indices for the PW150A. All data are [g/kg].	66
8.7	Effective Radiative Forcing (ERF) for most relevant aviation emissions chemical species	67
9.1	TLAR of Case Study Aircraft	70
9.2	Parallel Powertrain Efficiency Parameters	70
10.1	Power control parameters for minimum energy consumption, depending on brake specific fuel consumption of the gas turbine engine	79
10.2	Power control parameters for minimum energy consumption, depending on fuel cell efficiency	80
10.3	Power control parameters for minimum energy consumption, depending on battery specific energy	81
10.4	Power control parameters for minimum energy consumption, gravimetric index of the hydrogen fuel system	82

Nomenclature

Abbreviations

Abbreviation	Definition
BSFC	Brake Specific fuel consumption
DOH	Degree of Hybridization
EI	Emission index [g/kg]
EM	Energy mass <i>or</i> Electric motor
EMF	Energy mass fraction
ERF	Effective radiative forcing
FC	Fuel cell
GI	Gravimetric index
GT	Gas turbine
ISA	International Standard Atmosphere
KPIs	Key performance indicators
LHV	Lower heating value
OEM	Operative Empty Mass
OM	Operating mode
PL	Payload mass
PMAD	Power management and distribution
PTIS	Powertrain input scenario
PW	Power to weight ratio
SAF	Sustainable aviation fuels
SE	Specific energy
SP	Specific power
SPPH	Serial parallel partial hybrid
TLAR	Top level aircraft requirements
TOM	Take-off mass
WS	Wing loading
ZFM	Zero fuel mass

Symbols

Symbol	Definition	Unit
δ	Relative pressure	[]
η_{comp}	Efficiency of <i>component</i>	[]
θ	Relative temperature	[]
E_a	Energy related to energy source <i>a</i>	J
P_a	Power related to power source <i>a</i>	W
W_f	Fuel flow	kg/s
W_f	Fuel flow	kg/s
W_{ff}	Fuel flow factor (referenced to SL conditions)	kg/s

Introduction

In December 2019, the European Commission presented its Green Deal, outlining the objective of achieving net carbon neutrality across all sectors and EU member states by 2050. For aviation, this target is even more ambitious than those set by the Air Transport Action Group (ATAG), which call for carbon-neutral growth from 2020 onwards and a 50 percent reduction of emissions by 2050 relative to 2005 levels. These targets place considerable pressure on the aviation sector to decarbonize rapidly.

As presented in the "Clean Aviation Report" [13] and illustrated in Fig. 1.1, the aviation sector has demonstrated notable improvements in carbon efficiency per passenger over the past three decades. Advanced technologies, operational enhancements, and strategies such as increased seat density and utilization have collectively improved fuel efficiency per passenger kilometer by approximately 1-1.5% per year.

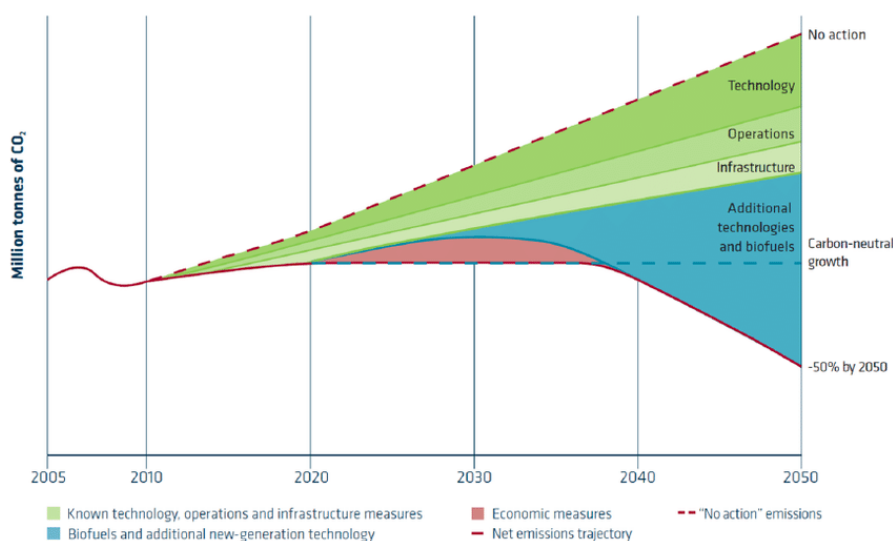


Figure 1.1: Projection of CO₂ emissions from aviation. Source: [23]

However, with continued population growth and economic development, air travel demand is projected to increase by 3-5% annually until 2050. This will lead to a substantial rise in direct CO₂ emissions from aviation, with a 34% increase observed in the past five years alone. Even with accelerated efficiency improvements reaching the ICAO target of 2% per year, aviation emissions are projected to double to approximately 1.5 to 2 gigatons of CO₂ by 2050.

This projection highlights the need for additional decarbonization measures, such as new technologies and biofuels (as indicated by the blue area in Fig. 1.1), to achieve the 50% emission reduction target

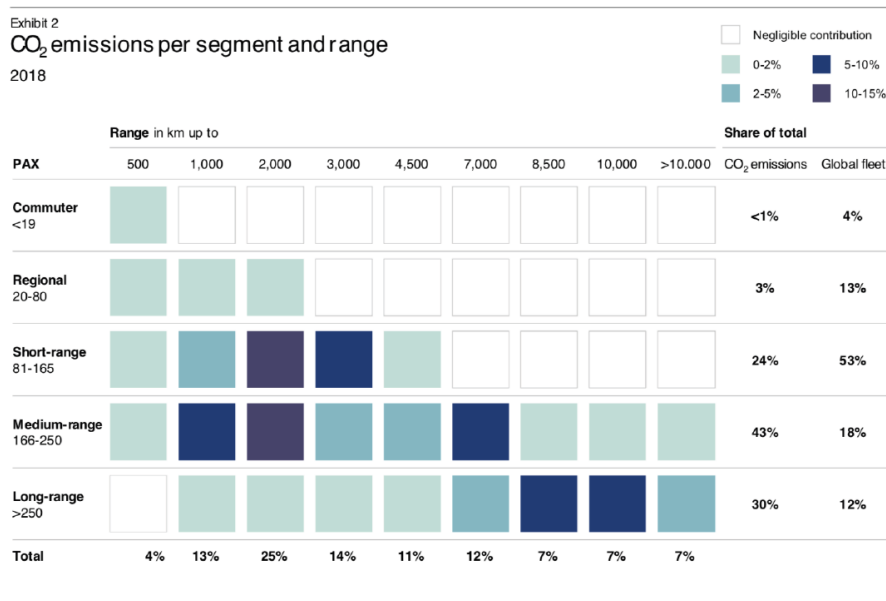


Figure 1.2: CO₂ emissions per segment and range. Source: [13]

set by ATAG.

Analyzing the CO₂ emission breakdown by passenger segment and range (Fig. 1.2), short- and medium-range aircraft (up to 2000 km) contribute most significantly to CO₂ emissions. Approximately two-thirds of the kerosene consumed in today's flights is used by these aircraft.

New technologies under consideration for decarbonizing aviation, besides sustainable aviation fuels (SAF), include battery-electric and hydrogen-powered aircraft.

- **Sustainable Aviation Fuels (SAF):** SAF encompasses alternative fuel sources designed to reduce aviation's environmental impact. The most advanced are biofuels (e.g., those produced via the hydroprocessed esters and fatty acids (HEFA) method from biomass or waste materials like cooking oils). Advanced biofuels, synthesized from solid feedstock, biomass (e.g., crops), or algae, are also being developed. Power-to-liquid fuels (synfuels), synthesized from hydrogen and carbon dioxide (sourced from industrial processes, biomass, or direct air capture), are another SAF option.
- **New Propulsive Technologies:** These include technologies based on batteries and turbogenerators, as well as the combustion of hydrogen in turbines and fuel cells powering electric motors.

Studies have assessed the viability of these technologies for different aircraft segments and ranges. SAFs are the easiest to implement across all segments and ranges, requiring no changes in aircraft or infrastructure.

While battery technology has advanced significantly, batteries remain a challenge due to their low gravimetric energy densities (0.2 to 0.5 kWh/kg) and limited lifespan, restricting their use as a sole power source to very short flights. Hydrogen can fuel aircraft by combustion in hydrogen-burning engines or by reacting in fuel cells that power electric motors. Despite hydrogen's gravimetric energy density being three times that of kerosene, its higher volume requires larger tanks, necessitating aircraft design modifications. The size and weight of hydrogen tanks pose a significant challenge for long-range flights with high energy demands, potentially impacting the economics of such aircraft.

Regarding the climate impact reduction potential (Fig. 1.4), SAFs, while not reducing direct emissions (due to the similar chemical reaction in gas turbines), can lead to a 30-60

For hydrogen, two scenarios exist: combustion in gas turbine engines and use in fuel cells. Both eliminate direct CO₂ emissions (due to the absence of carbon in the fuel) but increase water vapour emis-







Comparison vs. kerosene	 Biofuels	 Synfuels	 Battery-electric	 Hydrogen
Commuter <19 PAX	No limitation of range	No limitation of range	Maximum ranges up to 500-1,000 km due to lower battery density	No limitation of range
Regional 20-80 PAX				
Short-range 81-165 PAX			Not applicable	Revolutionary aircraft designs as efficient option for ranges above 10,000 km
Medium-range 166-250 PAX				
Long-range >250 PAX				
Main advantage 	Drop-in fuel – no change to aircraft or infrastructure	Drop-in fuel – no change to aircraft or infrastructure	No climate impact in flight	High reduction potential of climate impact
Main disadvantage 	Limited reduction of non-CO ₂ effects	Limited reduction of non-CO ₂ effects	Change to infrastructure due to fast charging or battery exchange systems	Change to infrastructure

Figure 1.3: Comparison of new technology and sustainable aviation fuels and new technologies. Source: [13]

sions. Fuel cells also enable near-zero NO_x emissions compared to the 50-80% reduction achieved with hydrogen combustion. Overall, both hydrogen approaches can significantly reduce climate impact, with fuel cells potentially achieving an 80% reduction.

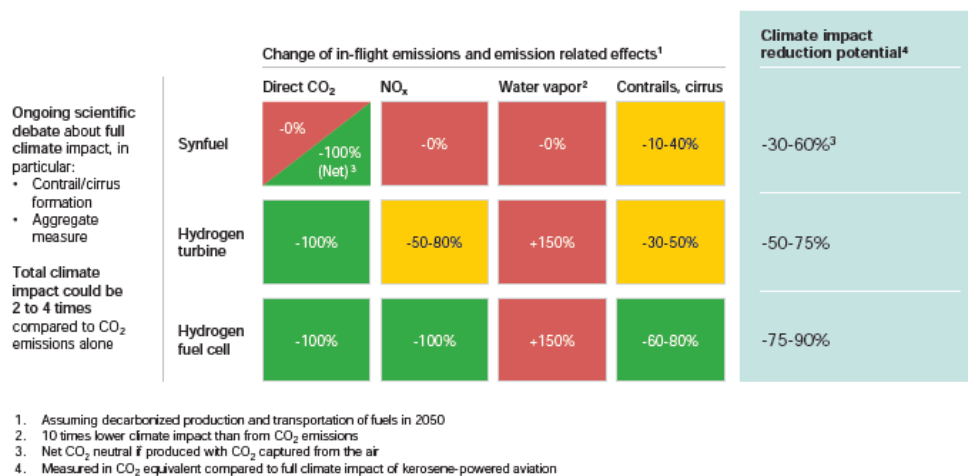


Figure 1.4: Comparison of climate impact from H₂ propulsion and synfuel. Source: [13]

2

Hybrid-Electric Propulsion

This chapter provides an overview of the current state of the art hybrid-electric propulsion architecture and modelling. The following architectures definitions are based on the National Academy of Engineering [34] that can be considered as the original classification of hybrid powertrain architectures. It comprehends six distinct architectures respectively one all-electric, three hybrid electric and two turboelectric. Many years later, the original classification was extended by De Vries [50] by adding a full electric configuration and a new full electric architecture.¹ As De Vries proposed [50], the term *hybrid system* is used to describe a system that incorporates both fuel combustion and full electric systems (i.e., batteries). Also, hybrid systems can employ gas turbine engines for propulsion and to recharge batteries, with the batteries also be able to supply energy for propulsion during one or more phases of flight.

2.1. Powertrain Architectures

The seven architectures mentioned before rely on different utilisation of conventional and hybrid-electric technologies, including gas turbines, batteries, electric motors and generators, and so forth. Below, a description of each hybrid-electric architecture is provided.

In a **Serial Hybrid** system, the electric motors are mechanically connected to the two propulsive lines, whilst the gas turbine is employed to drive an electrical generator. The output of this generator, along with the batteries power, provided electric power to the motors. Power produced by the electrical generator connected to the gas turbine can also charge the battery.

In a **Parallel Hybrid System**, a battery powered motor and a gas-turbine engine are mounted on the same shaft that drives a fan, enabling both or either to provide propulsion at any given time.

The **Series/Parallel Partial Hybrid System** comprises two propulsive lines that can be driven separately. The first line is driven directly by the gas turbine and electric motor, whereas the second line is driven exclusively by electrical motors. The motors can be powered by a battery or by a turbine-driven generator.

In both **Full and Partial Turboelectric** configurations, the battery is not employed as energy source during any phase of flight. Instead, gas turbine are utilised to drive electric generators, which power motors that drive the electric fans. A partial turboelectric system represents a variant of the full turboelectric system, whereby electric propulsion is employed to provide a portion of the propulsive power, with the remainder being provided by a turboprop driven by a gas turbine.

All-electric systems use batteries as the only source of propulsion power on the aircraft.

¹In this Thesis, the terms *powertrain architecture* and *configuration* denotes two different concepts. The term *powertrain architecture* is utilised to denote the classification as initially proposed by National Academy of Engineering [34] which is based on the manner in which the power sources are interconnected (serial, parallel, etc.). Conversely, a powertrain configuration signifies the manner in which a given powertrain architecture can utilise disparate energy sources or propulsion lines while maintaining the powertrain components interconnected consistently.

Figure 2.1 depicts the nine distinct architectures and configuration in graphical form. The representation is organised according to the functionality of the main components within the powertrain architecture. The energy sources are represented in a grey rectangular shape, with F or BAT denoting fuel or battery, respectively. Subsequently, the various powertrain components are illustrated, including the gas turbine (GT), gearbox (GB), electric motor/generator (EM), and propulsive lines (P). In accordance with the methodology proposed by De Vries [50], the powertrain elements can be classified into two distinct categories: primary and secondary components. The primary components are mechanically coupled to the gas turbine, either directly or indirectly. The secondary components encompass the devices that provide the necessary power for the electrically-driven propulsion system, namely the second propulsive line. It is assumed that the thrust produced by the gas turbine core exhaust is negligible in comparison to the total thrust, and therefore the thrust produced by the nozzle is not explicitly accounted for. The modelling of components such as converters or transformers is not explicitly undertaken, given that they do not result in a change to the type of power transmitted. Nevertheless, the impact of converters (i.e., inverters and rectifiers) can be incorporated by incorporating their weight correlations and efficiency losses into the associated electric motor/generator elements. Similarly, in the initial approximation, the weight and efficiency of the remaining electrical grid elements can be incorporated into the power management and distribution (PMAD) element.

A closer examination of each powertrain architecture illustrated in Fig. 2.1 reveals that they are, in essence, limit cases of the sixth (the Serial/Parallel Partial hybrid, SPPH). Consequently, with the appropriate parametrization, the SPPH architecture can be employed as a generic model, which can be solved for any other architecture. In other words, irrespective of the selected architecture, the same set of equations can be employed to calculate the powers of the constituent components, obviating the necessity for the derivation of architecture-specific equations, as is the case in other sizing methodologies.

2.2. Degree of Hybridization and Power Control Parameters

2.2.1. Degree of Hybridization

To describe a generic single hybrid system, it is essential to quantify the impact of the two sources in terms of energy and power.

Lorenz [30] defines the Degree of Hybridization descriptors DOH_E and DOH_P for any dual energy storage propulsion power system as the ratios between energy (or power) source a and the total energy (or power) of the dual-energy storage–propulsion–power system with sources a and b :

$$DOH_E = \frac{E_a}{E_a + E_b}; \quad DOH_P = \frac{P_a}{P_a + P_b} \quad (2.1)$$

For instance, considering available strategies for a hybrid-electric solution of transport aircraft, which would include the possibility of kerosene-only and universally electric options:

- Conventional kerosene-based gas-turbine aircraft, in which $DOH_P = 0$ and $DOH_E = 0$.
- Pure serial hybrid-electric architecture, where only electrical power is provided to the propulsive device(s), but energy storage is solely kerosene-based. In this configuration, $DOH_P = 1$ and $DOH_E = 0$.
- Full-electric aircraft, where electrical energy is stored in batteries. In this instance, both DOH_P and DOH_E are equal to 1.

Finding a formulation to relate these two parameters is essential for a better quantification of the dual energy storage system.

According to Isikveren [28] and following Lorenz [30] nomenclature, the overall efficiency η_{TOT} of any powertrain is defined as:

$$\eta_{TOT} = \eta_{EC} \cdot \eta_{TR} \cdot \eta_{PR} \quad (2.2)$$

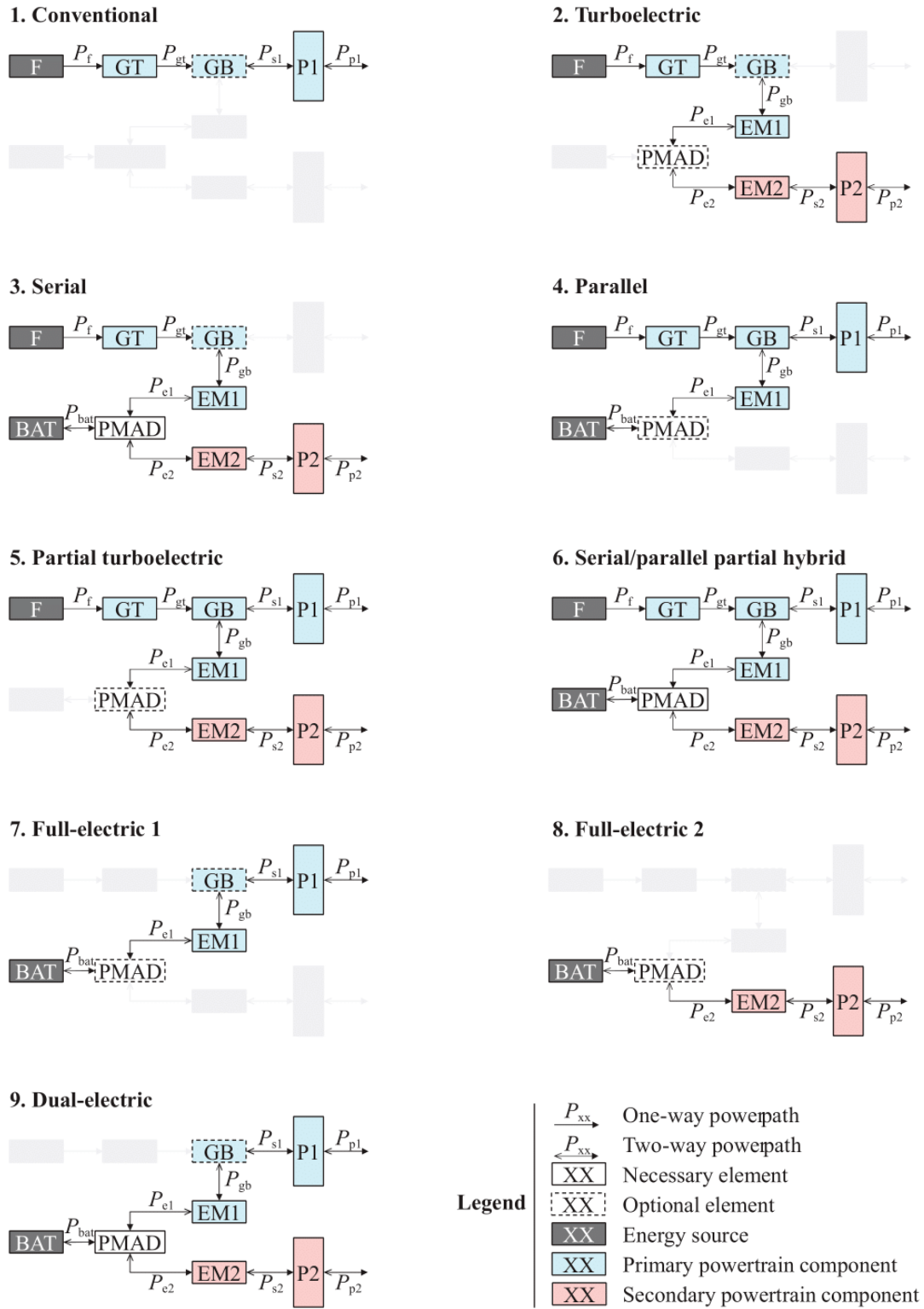


Figure 2.1: Battery-electric propulsion architectures. Source: [50]

where η_{EC} accounts for the entire conversion chain between any energy source (which provides supplied power P_{SUP}) and the propulsive devices (which provide installed power P_{INST}). In the case of a single-hybrid powertrain, it is defined as:

$$\eta_{EC} = \frac{P_{Inst,a} + P_{Inst,b}}{P_{Sup,a} + P_{Sup,b}} \quad (2.3)$$

In Equation 2.2, the terms η_{TR} and η_{PR} denote the transmission and propulsive efficiency, respectively. For a given operating time T , the total energy consumption can be evaluated as a function of the maximum supplied power for each energy source, weighted with the parameters $\bar{\omega}_a$ and $\bar{\omega}_b$, which account for the effective supplied power along the mission. They are defined as:

$$\bar{\omega}_a = \int_0^T \omega_a dt; \quad \bar{\omega}_b = \int_0^T \omega_b dt \quad (2.4)$$

A graphical illustration of a possible $\omega(t)$ pattern is shown below:

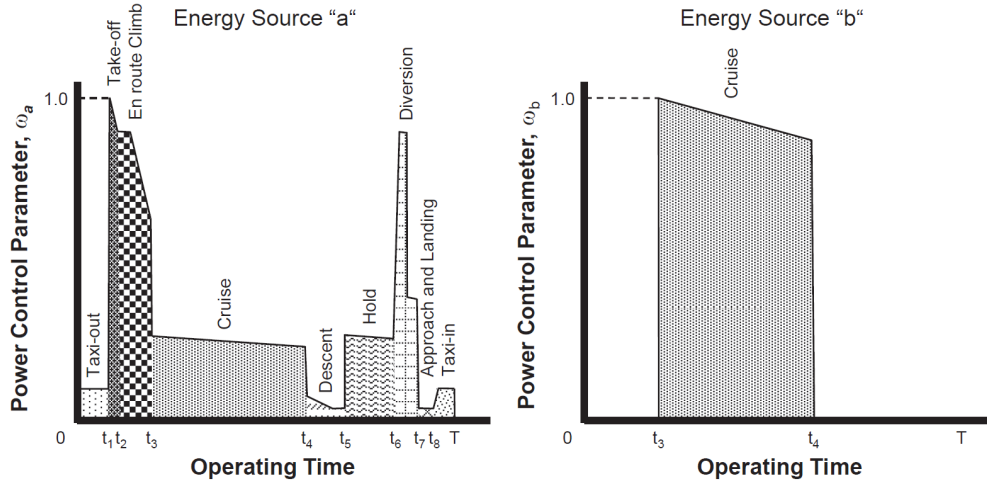


Figure 2.2: Example Representation of Parameter ω Over Flight Period (Source: [28])

Considering energy source b as the core descriptor, the *supplied power ratio* Φ for a double energy propulsion system can be defined as:

$$\Phi = \frac{P_{Sup,b}}{P_{Sup,a} + P_{Sup,b}} \quad (2.5)$$

Analogously, the activation ratio Ψ is defined as:

$$\Psi = \frac{\bar{\omega}_b}{\bar{\omega}_a + \bar{\omega}_b} \quad (2.6)$$

Both parameters vary between 0 and 1 if power (or energy) is totally accounted for by source a or energy source b , respectively.

Recalling the definition of Degree of Hybridization (Equation 2.1), it is useful to establish a relationship between the two Degree of Hybridization descriptors DOH_P and DOH_E . Then, Equation 2.1 becomes:

$$DOH_P = \frac{\Phi \cdot \eta_{EC,b}}{\eta_{EC,a} + \Phi \cdot (\eta_{EC,b} - \eta_{EC,a})} \quad (2.7)$$

$$DOH_E = \frac{\Phi \cdot \Psi}{(1 - \Phi) \cdot (1 - \Psi) + \Phi \cdot \Psi} \quad (2.8)$$

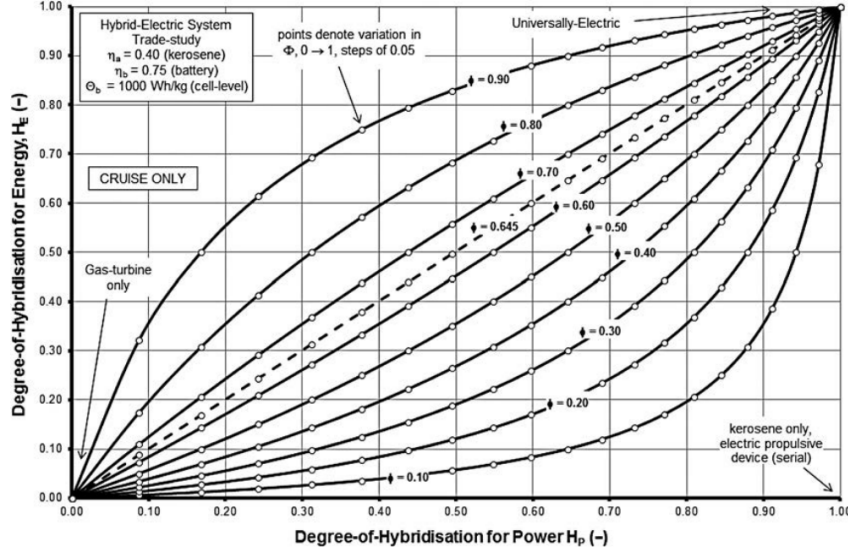


Figure 2.3: Example of a Degree-of-Hybridization Trade Study Conducted for a Hypothetical Hybrid-Electric System Based on Kerosene and Batteries as Energy Carriers. Source: [28]

2.2.2. Power Control Parameters for Battery Electric Aircraft

In the case of a battery electric dual-energy propulsion system, characterized by two propulsive lines, two parameters are necessary to describe hybrid architectures.

Coherently with the previous section and Isikveren [28], the *supplied power ratio* represents the fraction of the power supplied by the batteries in relation to the total amount of power used:

$$\Phi = \frac{P_{bat}}{P_{bat} + P_f} \quad (2.9)$$

The second parameter, called the *shaft power ratio*, was introduced by De Vries [50] and accounts for how the shaft power is split between the two propulsive lines. Saying that P_s represents the shaft power, the shaft power ratio φ is defined as:

$$\varphi = \frac{P_{s2}}{P_{s1} + P_{s2}} \quad (2.10)$$

These two parameters are understood to fall within the range of 0 to 1 during normal operational conditions. In the event that the fan is operating as a windmill, both parameters may assume negative values or exceed 1, thereby recharging the battery. The following table presents the values assumed for each configuration. A dot (·) represents that any value can be assumed.

In addition to the hybrid system power control parameters, the conventional gas turbine throttle setting is defined as the ratio of the power extracted by the gas turbine to the maximum power it can produce in the given flight condition:

$$\epsilon_{GT} = \frac{P_{GT}}{P_{GT,max}}. \quad (2.11)$$

Table 2.1: Control Parameters for Different Powertrain Configurations

Configuration	Φ	φ
Conventional	0	0
Turboelectric	0	1
Serial	.	1
Parallel	.	0
Partial TE	0	.
S/P Partial Hybrid	.	.
Full-Electric	1	0

An analogous coefficient is expressed for the electric motor throttle:

$$\epsilon_{EM} = \frac{P_{EM}}{P_{EM,max}} \quad (2.12)$$

Powertrain Equations The serial/parallel partial hybrid powertrain model presents ten unknowns in the power balance. De Vries [50] provided a solution to the systems in question.

The first seven can be obtained by applying a power balance across each component. In the case of a generic system, the equation on the left-hand side indicates the summation of power paths flowing "out" of the component, while the equation on the right-hand side represents the summation of power paths flowing "in" to the component, multiplied by the efficiency of the component. These correspond to the power balance equations across the gas turbine, gearbox, primary propulsor, primary electrical machine, PMAD, secondary electrical machine, and secondary propulsor, respectively. The power balance general equation is showed below, where η represent the efficiency of the component under consideration.

$$\Sigma P_{out} = \eta \cdot \Sigma P_{in} \quad (2.13)$$

The final three equations encompass the system architecture in its entirety, necessitating the utilisation of the power control parameters, designated as ϕ and φ . This is due to the fact that the value of ϕ defines the ratio between the power supplied by the battery and that supplied by the fuel, and also defines the ratio between the power delivered by the electric machine shaft and the total power delivered. Ultimately, the total propulsive power is determined.

This approach allows each configuration to be defined by making adjustments to the two powertrain parameters.

Component or Power Path	Equation
P_{GT}	$P_{GT} = \eta_{GT} P_f$
P_{GB}	$P_{GB} = \eta_{GB} P_{gt} - P_{s1}$
P_{p1}	$P_{p1} = \eta_{p1} P_{s1}$
P_{el1}	$P_{el1} = \eta_{em1} P_{gb}$
P_{el2}	$P_{el2} = \eta_{PMAD} (P_{el1} + P_{bat})$
P_{s1}	$P_{s1} = \eta_{gb} P_{GT} - P_{gb}$
P_{s2}	$P_{s2} = \eta_{em2} P_{e2}$
P_{p2}	$P_{p2} = \eta_{p2} P_{s2}$
P_{Bat}	$P_{Bat} = \frac{\Phi}{1-\Phi} P_f$
P_{s2}	$P_{s2} = \frac{\varphi}{1-\varphi} P_{s1}$
P_p	$P_p = P_{p1} + P_{p2}$

Table 2.2: Powertrain equations. Source: [50]

These equations can be represented in matrix form as:

$$\begin{bmatrix}
 -\eta_{GT} & 1 & 0 & 0 & 0 & 0 & 0 & 0 & 0 & 0 \\
 0 & -\eta_{GB} & 1 & 1 & 0 & 0 & 0 & 0 & 0 & 0 \\
 0 & 0 & 0 & -\eta_{P1} & 0 & 0 & 0 & 0 & 1 & 0 \\
 0 & 0 & -\eta_{EM1} & 0 & 1 & 0 & 0 & 0 & 0 & 0 \\
 0 & 0 & 0 & 0 & -\eta_{PMAD} & -\eta_{PMAD} & 1 & 0 & 0 & 0 \\
 0 & 0 & 0 & 0 & 0 & 0 & -\eta_{EM2} & 1 & 0 & 0 \\
 0 & 0 & 0 & 0 & 0 & 0 & 0 & -\eta_{P2} & 0 & 1 \\
 \Phi & 0 & 0 & 0 & 0 & (\Phi - 1) & 0 & 0 & 0 & 0 \\
 0 & 0 & 0 & \varphi & 0 & 0 & 0 & (\varphi - 1) & 0 & 0 \\
 0 & 0 & 0 & 0 & 0 & 0 & 0 & 0 & 1 & 1
 \end{bmatrix}
 \begin{bmatrix}
 P_f \\
 P_{gt} \\
 P_{gb} \\
 P_{s1} \\
 P_{e1} \\
 P_{bat} \\
 P_{e2} \\
 P_{s2} \\
 P_{p1} \\
 P_{p2}
 \end{bmatrix}
 =
 \begin{bmatrix}
 0 \\
 0 \\
 0 \\
 0 \\
 0 \\
 0 \\
 0 \\
 0 \\
 0 \\
 P_p
 \end{bmatrix}
 \quad (2.14)$$

The signs of the coefficient matrix were assumed to reflect the indicated power flows, as represented by the filled arrowheads. This implies that the values in the coefficient matrix are not constants, but rather depend on the direction of the power flows, that is, on the sign of the solution variables. A more detailed examination of the SPPH architecture reveals that there are, in fact, nine distinct operational modes. Accordingly, nine distinct coefficient matrices are required to accommodate all nine potential scenarios.

2.3. Relevant Examples

2.3.1. Parallel Architecture

SUGAR Volt One relevant example of a parallel hybrid is the SUGAR Volt project (Subsonic Ultra Green Aircraft Research), as outlined by Bradley and Droney [4]. This project was conducted by Boeing Research and Technology, Boeing Commercial Airplanes, General Electric, and Georgia Tech (NASA, 2011). The propulsion system for the SUGAR Volt is a hybrid electric engine architecture that employs an electric motor powered by batteries to distribute power to the low-pressure spool of the turbofan.

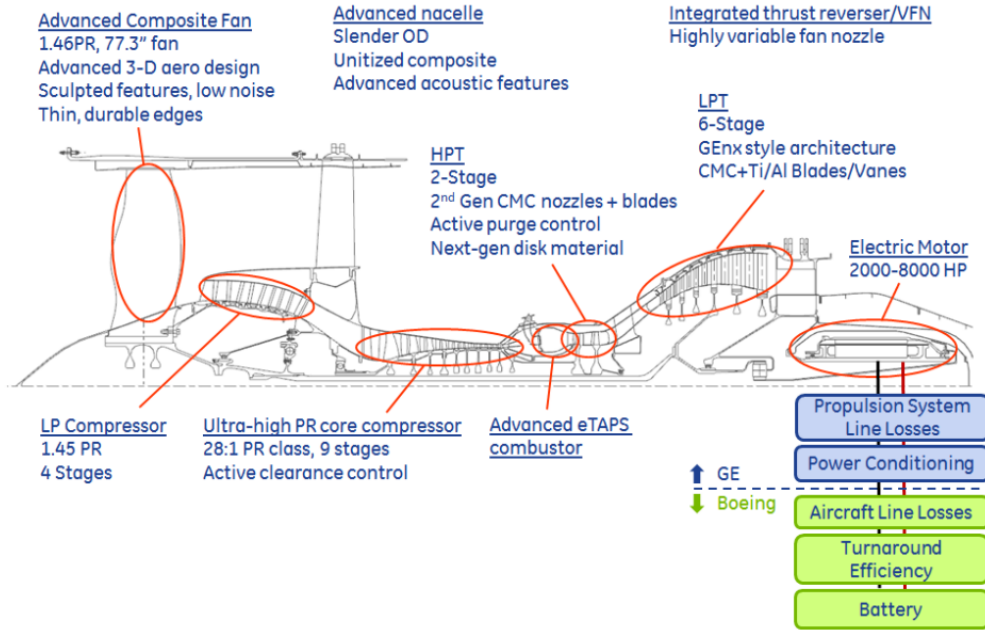


Figure 2.4: SUGAR propulsion group. Source: [4]

A series of performance and sizing tasks were conducted on hybrid electric versions of a conventional tube-and-wing aircraft. The configuration comprises a conventional turbofan engine augmented by an

electric motor and battery. The aircraft under consideration is a small, medium-range aircraft with a seating capacity of 154 passengers and a maximum range of 3,500 nautical miles.

Two different configurations in terms of electric power were considered, even though the basic hybrid configuration remained the same.

- Balanced (1750 HP);
- Core-shutdown (7150 HP).

This increase in electrical power would provide the option of utilising electric power to drive the low-pressure turbine, either partially or fully. Consequently, the core of the turbofan could be decelerated to an idle or windmill-like condition,

Table presents four different solutions for the aircraft under consideration. The first two represent aircraft with classic kerosene propulsion. The first with a classic CFM56 turbofan engine, while the second with an innovative turbofan designed by General Electric to enter into service in 2040. The last two shows different hybrid electric configurations, in terms of electric power were considered, even though the basic hybrid configuration remained the same.

The aforementioned increase in electrical power would provide the option of utilising electric power to drive the low-pressure turbine, either partially or fully. Consequently, the core of the turbofan could be decelerated to an idle or windmill-like condition. Table 1.3 presents four different solutions for the aircraft under consideration. The initial two cases illustrate aircraft equipped with conventional kerosene-based propulsion systems. The first employs a conventional CFM56 turbofan engine, while the second utilises an innovative turbofan design, developed by General Electric, which is scheduled to enter service in 2040. The final two examples illustrate various hybrid electric configurations with respect to the allocation of electric power, despite the underlying hybrid configuration remaining consistent.

- Balanced (1750 HP);
- Core-shutdown (7150 HP).

It is worthy of note that despite a notable reduction in fuel and energy consumption resulting from hybrid solutions, it is not possible to attribute the full extent of this reduction to the hybrid system itself. Indeed, the "SUGAR High," which is a high-span truss-braced tube and wing aircraft (similar to SUGAR Volt), exhibits a comparable energy consumption profile to that of the balanced hybrid configuration. It is evident that the fuel consumption of hybrid solutions is reduced as a consequence of the utilisation of batteries.

The results demonstrate that the balanced configuration exhibits a notable reduction in take-off weight, amounting to 21%, which is attributable to the lower weight of batteries (one-third). This, in turn, leads to a substantial decrease in overall energy consumption.

Model Sizing Level	Unit	765-093 FREE	765-095 SUGAR High	Balanced (Ref Hp 1750)	Core Shutdown (Ref Hp 7150)
Passengers / Class	-	154 / DUAL	154 / DUAL	154 / DUAL	154 / DUAL
Max Takeoff Weight	ton	82.8	62.8	63.4	86.2
Max Landing Weight	ton	67.8	61.5	63.2	85.9
Max Zero Fuel Weight	ton	63.7	57.9	59.6	82.2
Max Battery Weight	ton	-	-	7.6	21.7
Operating Empty Weight	ton	42.8	36.9	38.0	46.5
Fuel Capacity Req / Avil	L	36457 / 36457	15944 / 15944	15596 / 17429	16754 / 23996
Engine Model	-	CFM56	gFan+2	hFan+2	hFan+2
Fan Diameter	cm	157.5	167.6	170.2	200.7
Horsepower	kW	-	-	1120	5260
Boeing Equivalent Thrust (BET)	kN	124.2	85.9	80.1	92.1
Wing Area / Span	m ² / m	130.6 / 36.9	111 / 36.3	119.8 / 48.5	156.1 / 55.2
Aspect Ratio (Effective)	-	10.41	19.56	19.56	19.56
Optimum CL (SR / LR)	-	0.584	0.759	0.728 / 0.730	0.730 / 0.733
Cruise L/D @ Opt CL (SR / LR)	-	17.997	23.995	23.537 / 24.213	25.223 / 25.933
Long Mission Range	km	6815	6482	6482	6482
Performance Cruise Mach	-	0.79	0.70	0.70	0.70
Long Range Cruise Mach (LRC)	-	0.79	0.70	0.70	0.70
Thrust ICAC (MTOW, ISA) (SR / LR)	m	11033	11489 / 11582	12253 / 11490	11582 / 12771
Time/Dist (MTOW, 35k FT, ISA)	MIN / km	23 / 274	(23 / 147) / (148 / 274)	(22 / 28) / (241 / 319)	(17 / 23) / (185 / 250)
Opt. Altitude (MTOW, ISA) (SR / LR)	m	10638	11491 / 11490	11643 / 11674	11339 / 12527
Buffet ICAC (MTOW, ISA) (SR / LR)	m	11033	13084 / 12771	13503 / 13411	13202 / 14326
TOFL (MTOW, Sea Level, 86 Deg F)	m	2496	2493	2493	2054
Approach Speed (MLW)	km/h	233	196	196	202
Block Fuel / Seat (900 NM)	kg	41.5 (0%)	19.3 (-53.6%)	16.58 (-13.9%)	15.09 (-21.7%)
Block Energy / Seat (900 NM)	MJ	1795 (Base)	789 (-53.6%)	801 (-53.9%)	917 (-46.0%)
Fuel Energy Fraction	%	100%	87.8%	86.6%	67.3%

Table 2.3: Comparison of conventional aircraft, SUGAR High, Balanced configuration(Ref Hp 1750), and Core Shutdown Configuration (Ref Hp 7150). Source: [4]

AMBER: Advancing Hybrid-Electric Propulsion The Clean Aviation AMBER programme has the objective of developing a mature fuel cell-based propulsion system for regional aircraft, with the aim of creating an engine of MW-class. The parallel hybrid electric propulsion system comprises an existing state-of-the-art thermal turboprop engine, designated the Catalyst, which was developed by Avio Aero, and an electric motor powered by a hydrogen fuel cell.

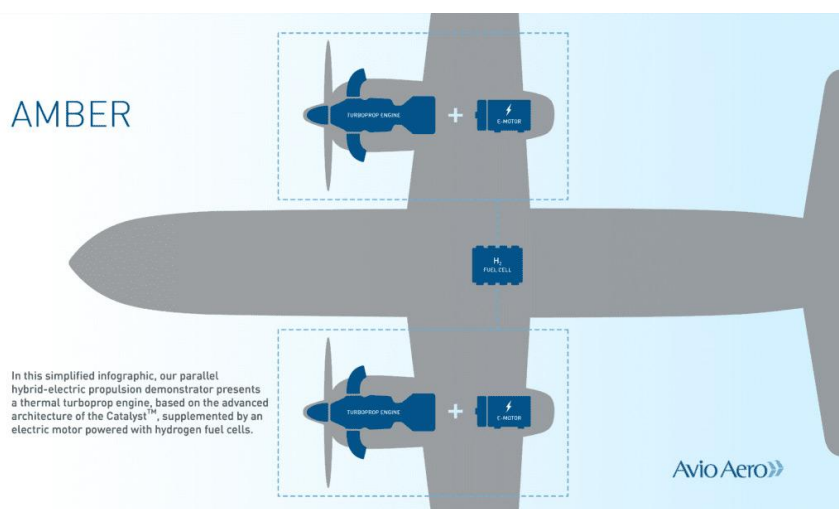


Figure 2.5: Amber propulsion system. Source: [11]

2.3.2. Turboelectric Architecture

NASA STARC-ABL A single-aisle commercial transport concept with a turboelectric propulsion system architecture was developed by NASA [51] with a projected entry into service date of 2035. This concept was designed for comparison with a similar technology conventional configuration. The turboelectric architecture comprised two underwing turbofans with generators that extracted power from the fan shaft and transmitted it to a rear fuselage, axisymmetric, boundary layer ingesting fan. The turboelectric distributed propulsion architecture decouples the power-producing components from the thrust-producing components, allowing the two to be widely separated. This enables each to operate at peak efficiency conditions, rather than at a compromise between the two, thereby increasing the

overall thermal efficiency. It is imperative to consider the detrimental effect of the efficiency loss due to the power conversion from mechanical to electrical, the transmission of electrical power, and the conversion from electrical power back to mechanical power.

The STARC-ABL concept was designed for a mission profile analogous to that of a contemporary Boeing 737-800 or Airbus A320. The configuration is that of a tube-and-wing, with two turbofans mounted under the wings.

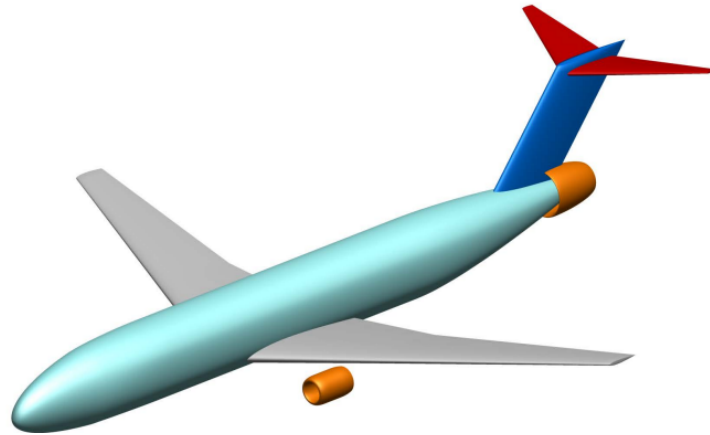


Figure 2.6: STARC ABL render in OpenVSP. Source:[51]

The results indicate that the turboelectric concept has an average block fuel reduction of 10%, depending on the mission. The increase in propulsion system efficiency from the rear fuselage BLI fan, which ingests only a portion of the boundary layer, and the downsizing of the underwing turbofans, which helps offset the weight of the additional turboelectric system components, are the key sources of this benefit.

2.4. All Electric Architecture

Sky Spark One notable example of a full-electric aircraft is the SkySpark [45]. It is a very light aircraft, derived from the Pioneer 300 and entirely retrofitted to operate as an electric aircraft. The project was undertaken by Digisky and Politecnico di Torino. The aircraft is distinguished by an empty mass of 450 kg and a wing span of 7.33 m. The aircraft was originally designed as a technical demonstrator for a high performance PEM fuel cell with an output of approximately 60 kW, more than 1kW/kg Power Density and a gaseous H₂ reservoir of 75L at 350 atm.

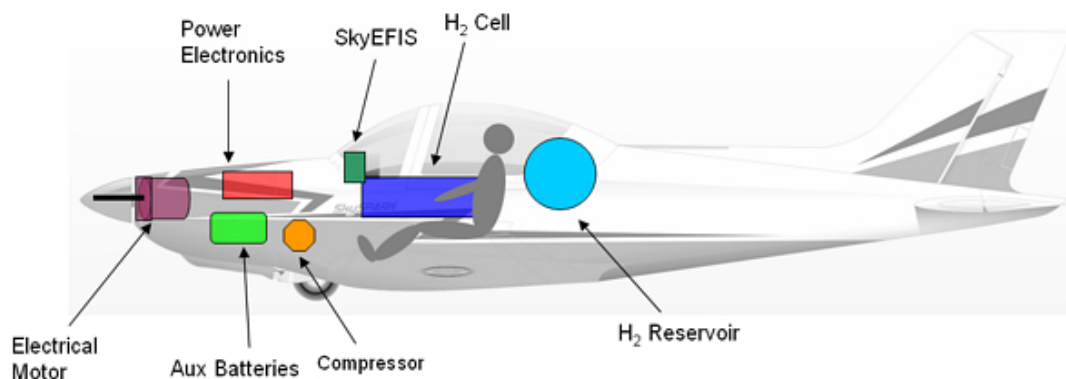


Figure 2.7: SkySpark configuration. Source: [45]

However, it was subsequently converted into a full battery aircraft. The propulsion system comprises a 65 kW brushless motor with a power Density $> 2\text{ kW/kg}$, a power electronic system comprising an 85 kVA-450 V inverter for supplying electrical power to the engine, a DC/DC converter for the avionic 12/24 V bus, and a 22 kWh Li-Po battery pack. The aircraft was able to achieve the highest speed world record for an full-electric aircraft.

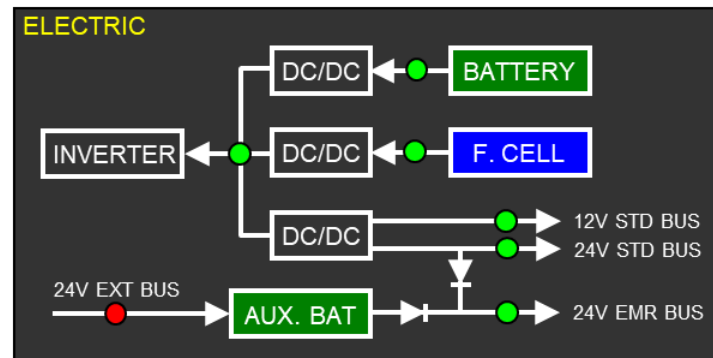


Figure 2.8: SkySpark electric bus. Source [45]

Universal Hydrogen In 2024, the company Universal Hydrogen operated the inaugural regional aircraft powered in part by hydrogen propulsion. The aircraft in question was a converted De Havilland Canada Dash-8, in which a fuel cell has been installed to replace one of the existing turboprop engines. The remaining aircraft was powered by kerosene. A modular and removable tank was affixed to the rear of the fuselage.

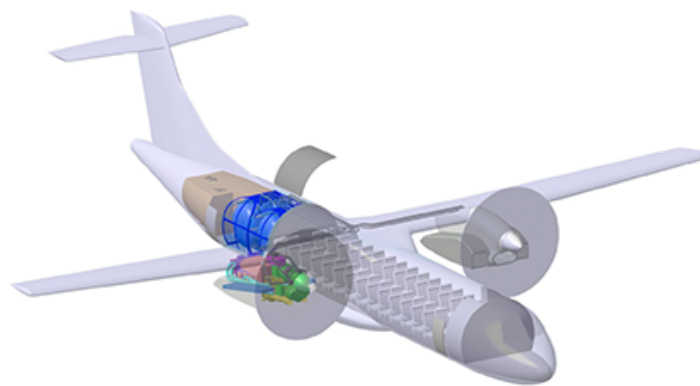


Figure 2.9: Universal Hydrogen propulsion system model. Source: [26]

3

Study Objective

As outlined in Chapter 1, new powertrain technologies are required to meet the ATAG emission targets by 2050. These technologies include the use of batteries, hydrogen, and sustainable aviation fuels (SAF).

Analysis of both the Clean Aviation Report [13] and existing studies on hybrid aircraft architectures (Section 2.3), reveals that new technologies are typically analysed singularly or considering a dual energy storage powertrain, such as battery-electric aircraft [51] or hydrogen-kerosene aircraft [11]. Current state-of-the-art hybrid propulsion modelling [50, 38], in terms of Powertrain Architectures (Chapter 2.1), System Descriptors (Section 2.2), and equations (Table 2.2), naturally focuses solely on single-hybrid powertrain aircraft, in particular battery-electric. Clearly, no studies account the simultaneous presence of a threefold energy storage powertrain.

A research gap has been identified in the modelling of a Double-Hybrid Powertrain that encompasses kerosene, hydrogen combustion, fuel cells, and batteries. This gap includes the subsequent evaluation and sensitivity analysis of how different combinations of these energy sources impact the overall aircraft performance and environmental impact.

This thesis addresses the following research questions:

Research Questions

- **Q1:** What effect does the introduction of hydrogen combustion and fuel cells have on single-hybrid powertrain architectures and their relative operating modes?
- **Q2:** How can the conceptual design synthesis method be adapted to account for the Double-Hybrid Powertrain?
- **Q3:** How do different combinations of kerosene, hydrogen (used in gas turbines or fuel cells), and batteries impact the key performance parameters of the aircraft?
- **Q4:** How do parameters such as battery specific energy, gas turbine and fuel cell efficiency, and hydrogen fuel system gravimetric index influence the sensitivity analysis results?

4

Fundamental of Hybrid Powertrain Components

This chapter outlines the fundamental components of a hybrid-electric architecture based on hydrogen, fuel cells, and gas turbines. It begins with an overview of turboprop engine performance, followed by a comparison of hydrogen and kerosene combustion. Challenges related to onboard hydrogen storage are then discussed. Finally, the working principles and sizing of fuel cells are presented.

4.1. Turboprop Engine

Turbofans and turboprops, powered by gas turbines, are the predominant means of air transportation today. Turboprop engines are a type of gas turbine engine that generate most of their thrust using a propeller driven by a free turbine through a reduction gearbox. Turboprop engines offer higher propulsive efficiency at low speeds, which translates to shorter runway requirements for take-off. Provided the speed does not compromise propeller efficiency, turboprop engines have the lowest specific fuel consumption compared to other gas turbines.

Turboprop efficiency (and gas turbine engine efficiency in general), also known as global gas turbine engine efficiency, is defined as:

$$\eta_{GT} = \frac{P_s}{\dot{m}_f \cdot LHV_f} \quad (4.1)$$

where P_s represents the extracted shaft power, \dot{m}_f the fuel flow rate, and LHV_f the lower heating value of the fuel.

For a turboprop engine, efficiency is conventionally expressed as Brake Specific Fuel Consumption (BSFC), defined as:

$$BSFC = \frac{\dot{m}_f}{P_s} \quad [g/kWh] \quad (4.2)$$

On-design, BSFC is a function of the total turbine inlet temperature T_3^0 and the compression ratio β . Its trend is illustrated in Fig. 4.1.

Off-design, the shaft horsepower, BSFC, and net thrust are corrected for altitude and true airspeed, as shown in Fig. 4.2.

Finally, BSFC for different throttle settings (equivalent to shaft speed percentage for a turboprop engine) is presented as a function of true airspeed in Fig. 4.3.

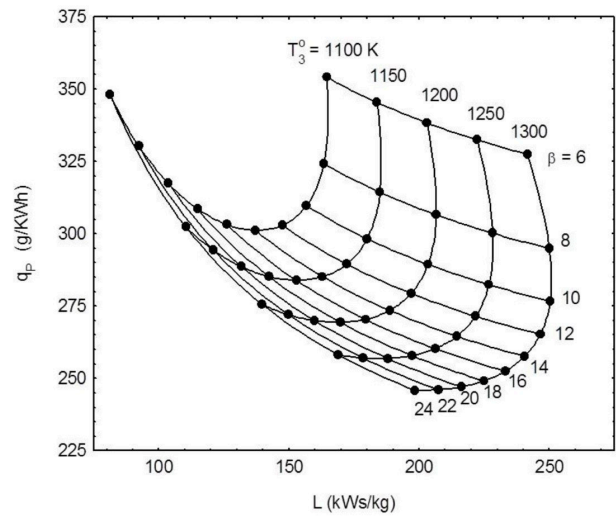


Figure 4.1: Gas turbine engine on-design performance at sea level conditions. Souce: [25]

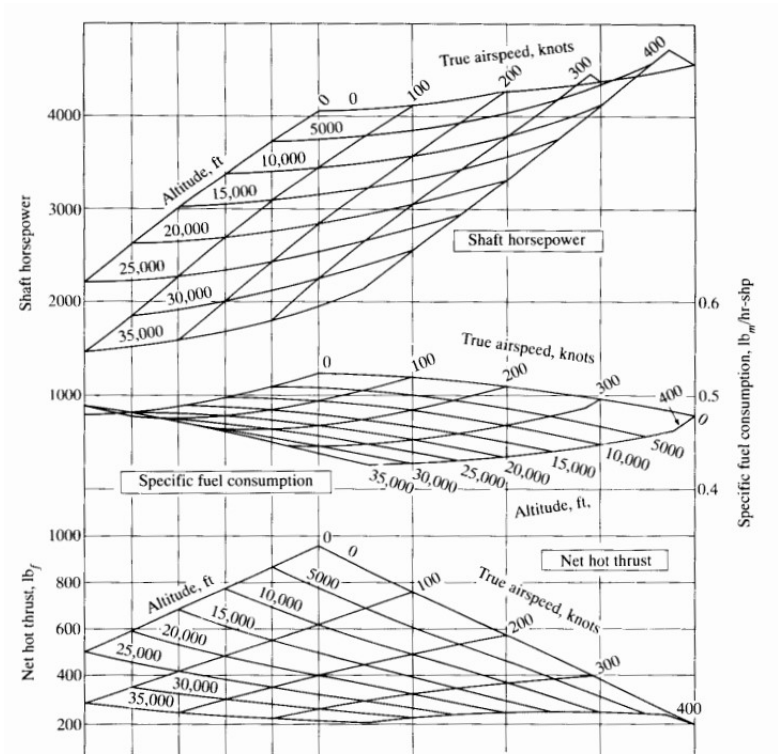


Figure 4.2: Turboprop off-design performance. Souce: [25]

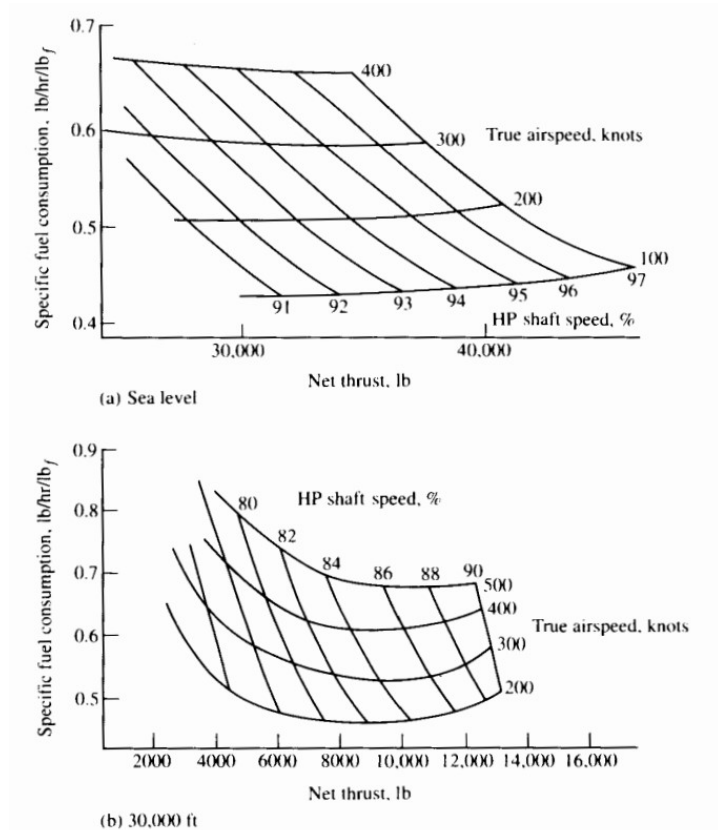


Figure 4.3: Gas turbine engine performance at various throttle settings. Source: [25]

4.2. Fundamental of Hydrogen Combustion

Given the disparate combustion properties of hydrogen in comparison to kerosene, the necessity arises for the design of new engines that are optimised specifically for hydrogen. Nevertheless, it is feasible to modify existing turbomachinery to enable the combustion of hydrogen by modifying the combustor and fuel supply system [6]. The fundamental concept of a hydrogen-powered gas turbine remains unchanged from that of a kerosene-powered engine. Consequently, engineers can draw upon their previous experience in the development of kerosene-fuelled engines. Gas turbines have a higher specific power than other propulsion methods, particularly for high-power applications. To illustrate, the fuel cell-powered propulsion system of the 737–800-sized CHEETA aircraft [9],[52] is approximately three times the weight of the estimated turbofan propulsion system installed on the 737–800 [18].

The fan, compressor, turbine, and nacelle in a hydrogen-powered gas turbine operate in a manner analogous to their counterparts in kerosene-fuelled engines, thereby necessitating only minimal design alterations, if any. The combustor is the sole component that necessitates substantial alterations. In order to comprehend the reasons behind the distinctive characteristics of hydrogen combustion, it is essential to undertake a preliminary examination of the fundamental thermodynamic concepts. The stoichiometric fuel-to-air ratio is defined as the ratio of fuel mass flow to air mass flow, representing the theoretical maximum rate of combustion where all the fuel is burned and all the oxygen in the air is consumed. The stoichiometric fuel-to-air ratio of hydrogen is 1:34, which is less than half that of kerosene (1:15) [6]. The actual fuel-to-air ratio can be divided by the stoichiometric fuel-to-air ratio to yield the equivalence ratio, which is a useful parameter for quantifying the amount of air involved in the combustion process. Equivalence ratios less than one correspond to lean combustion, in which more air is supplied than is necessary to fully burn the hydrogen. As illustrated in Figure 4.4, hydrogen's wider flammability limits enable it to be burned much leaner than kerosene.

The principal disadvantage of the greater flammability range is that the hydrogen-air mixture is so reactive that premixing before injection into the combustor is inherently risky. The process of premixing

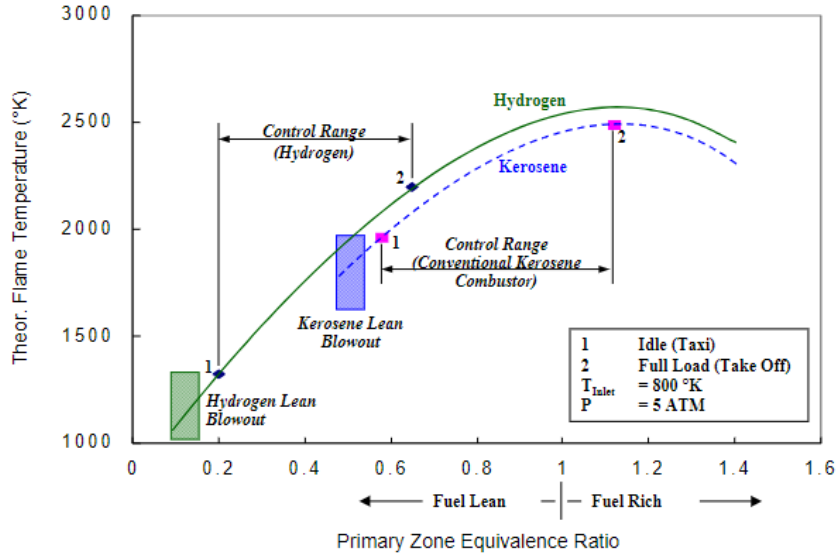


Figure 4.4: Temperature Characteristics of a Combustor. Source [5]

introduces the risk of flashback, whereby the flames travel upstream from the combustor into the mixing zone. Despite the absence of soot, CO_2 and other pollutants typically associated with hydrocarbon combustion, the process of hydrogen combustion still results in the production of nitrogen oxide (NO_x). The quantity of NO_x generated is contingent upon the residence time and combustion temperature. The combustion of hydrogen occurs at a higher flame speed than that of kerosene. This results in a faster combustion process and consequently, a reduction in residence time, which in turn leads to a decrease in NO_x emissions and a shorter combustor. The flame temperature of hydrogen is greater than that of kerosene when burned at an equivalence ratio of one. Nevertheless, the flame temperature can be reduced by burning hydrogen in a leaner mixture than kerosene. It can be reasonably assumed that a fully mixed hydrogen-air mixture will result in a reduction in NO_x production due to the lower flame temperature associated with lean combustion. However, in the absence of adequate mixing, localised areas of high temperature and combustion occur where the air and fuel are in stoichiometric equilibrium, resulting in the production of NO_x . It is essential to develop mechanisms that can enhance the mixing intensity without the necessity of premixing the fuel and air, in order to facilitate *low* – NO_x hydrogen combustion. Verstraete [47] reports that a **3% saving of thrust specific energy consumption** is possible with hydrogen combustion, thanks to the higher specific heat of hydrogen combustion gases compared to equivalent gases from hydrocarbon combustion.

The energy specific fuel consumption or ESFC is defined as

$$ESFC = TSFC \cdot LHV_{H_2} = \frac{\dot{m}_f \cdot LHV}{F_N} \quad (4.3)$$

where

- $TSFC$ is the thrust specific fuel consumption;
- \dot{m}_f represent the fuel flow rate;
- LHV_{H_2} the lower heating value of hydrogen;
- F_N defines the net thrust produced by the engine.

The ESFC is defined in order to facilitate a comparison between fuels with disparate lower heating values. It is a measure of the efficiency with which the energy present in the fuel is converted into thrust.

The ESFC advantage is illustrated in Figure 4.5. The figure illustrates the specific heat at constant pressure and the isentropic expansion coefficient, γ , for air, kerosene combustion gases and hydrogen combustion gases. The fuel-to-air ratios employed to construct the curves are derived from typical take-off conditions for a high bypass ratio GE90-like engine for both fuels. The conclusions presented in the figure are applicable in general and are not contingent on the specific engine type or operating conditions. The specific heat for hydrogen combustion gases is higher than that of kerosene, which results in a slightly lower temperature drop for a given turbine work (or enthalpy drop). As demonstrated by the subsequent equation, this phenomenon is partially counterbalanced by the slightly reduced gas flow rate resulting from the diminished fuel flow rate of hydrogen. Nevertheless, the impact of the compositional alteration is the most significant factor.

$$P_{\text{turb}} = (\dot{m}_a + \dot{m}_f) \cdot c_p \cdot (T_{t,\text{in}} - T_{t,\text{out}}) \quad (4.4)$$

where

- P_{turb} is turbine output power;
- $T_{t,\text{in}}, T_{t,\text{out}}$ the total temperature at the turbine inlet and outlet;
- \dot{m} stands for the mass flow rates of air (a) and fuel (f).

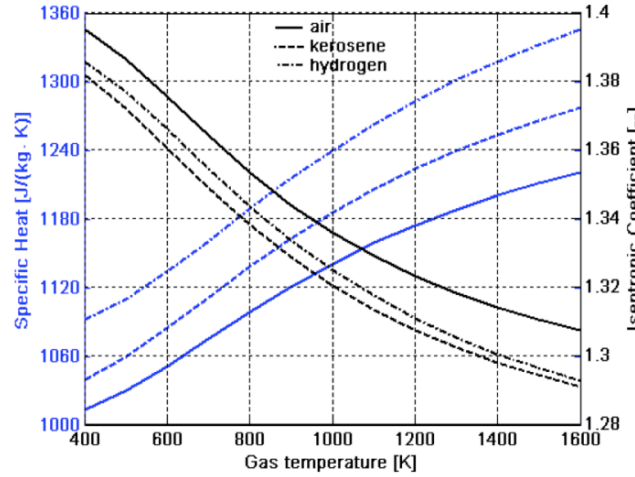


Figure 4.5: Changes in combustion gas properties when using hydrogen. Source: [47]

Given that the combustion of hydrogen produces a higher value of the γ , it is possible to achieve the requisite temperature reduction with a smaller pressure drop. This results in a greater quantity of energy being retained in the gases after the turbine, which in turn gives rise to an enhanced thrust.

$$\frac{T_{t,\text{out}}}{T_{t,\text{in}}} = \left(\frac{p_{t,\text{out}}}{p_{t,\text{in}}} \right)^{\frac{\gamma-1}{\gamma}} \quad (4.5)$$

In this context, the term p_t represents the total pressure. Consequently, the engine may be operated at a lower temperature for a given thrust output, or it may be constructed in a smaller size.

If the hydrogen is stored on board in liquid form, it provides a substantial heat sink. This enables engine designers to investigate innovative methods of enhancing performance. In their analysis, Boggia and Jackson [2] cite three potential modifications to the hydrogen-burning version of the A320 engine.

- Precooling the air entering the compressor is an effective method for facilitating compression. This approach has the potential to result in a 5.7% reduction in thrust specific fuel consumption (TSFC);

- Cooling the bleed air around the combustor and mixing it before the turbine should enable increases to the Turbine inlet temperature and a 2.1% reduction in TSFC;
- Preheating the hydrogen fuel from 25 to 250 K using the engine's hot exhaust, reducing fuel consumption by 1%–3%[15].

4.3. Hydrogen Tank

One of the first study [7] about liquid hydrogen tank was based on a 400-passenger airliner with 5500 miles of range. The airplane design consisted of two LH2 fuel tanks made from Al-2219 located forward and aft in the fuselage. These tanks operate at a maximum pressure of 21 psi and a minimum temperature of 25K. Some conclusions of this study with regard to the structural design of LH2 fuel tanks for aviation are:

- Tank pressure should be higher than atmospheric to prevent air ingestion that may cause an explosion hazard;
- Non-integral fuselage tanks require a larger available volume to store LH2;
- Due to maintenance difficulties, LH2 fuel tanks should be designed for a full service life;
- Fuel weight fraction (W_{Tank}/W_{LH2}) of liquid integral tank is ≈ 0.2
- Elliptical domes with ($a/b = 1.66$) offer the best combination of weight and tank length.

Between 1998 and 2002 the European Union commissioned Airbus and an extensive group of manufacturers and universities (e.g. Cranfield, TU Delft, Hamburg, TU Munich) to study possible airplane configurations that might allow a smooth transition from kerosene to hydrogen. The project, called Cryo-plane, gave the following conclusions with regard to the fuel tank design: For small regional airplanes a single LH2 tank can be located behind the pressure bulkhead, meanwhile, for middle and long-range airplanes a forward location of LH2 tank is required to maintain the C.G. within the allowable range, For small regional airplanes a single LH2 tank can be located behind the pressure bulkhead, meanwhile, for middle and long-range airplanes a forward location of LH2 tank is required to maintain the C.G. within the allowable range.

Shape and volume As Brewer[7]reported, there are two possible types of fuel tank: integral and non-integral. Non-integral tanks serve only as fuel containers and are mounted within and supported by a conventional fuselage skin/stringer/frame structure. Consequently, they only have to bear the loads associated with the fuel containment, i.e. pressurisation and fuel dynamic loads, plus thermal stresses (Brewer, 1991). Integral tanks, conversely, constitute an integral component of the basic airframe structure, necessitating their capacity to withstand the full spectrum of fuselage stresses stemming from critical aircraft loading conditions, in addition to the aforementioned loads. In the absence of the fuselage structure's protective barrier, an overlay must be applied to the insulation in the integral tank design. The necessity for an additional protective layer is driven by the fact that the external surface of the integral tank design is not protected by the fuselage structure, as is the case in the non-integral design. This extra shielding provides protection from both aerodynamic heating and air loads. In addition, integral tank is to be preferred over the non-integral tank with regard to the overall weight of the aircraft and the more straightforward accessibility of its components for the purposes of inspection. The integration of the tank into the fuselage necessitates the adaptation of the tank's geometry to align with the fuselage's dimensions to ensure optimal utilisation of the available space. Preliminary design shows that spherical or cylindrical tank shapes with a diameter equal to that of the fuselage as the sole viable option. The utilisation of spherical tanks ensures a minimal surface area in relation to its volume. This, in turn, leads to a reduction in passive heat flux and subsequent boiling of liquid hydrogen (LH2) within the tank. The spherical shape poses manufacturing challenges and has a higher frontal surface area, resulting in higher drag forces compared with a cylindrical tank. Conversely, cylindrical tank shapes are easier to manufacture but have a higher surface area to volume ratio, resulting in a higher passive heat load into the tank. However, they are easier to integrate into the tubular fuselage, offering a higher volumetric efficiency. The adoption of cylindrical tanks in this work is predicated on the aforementioned factors. It should be noted, however, that the aft tank, being situated in the tail cone, will not be purely cylindrical but conical, in order to comply with the shape of the aft fuselage.

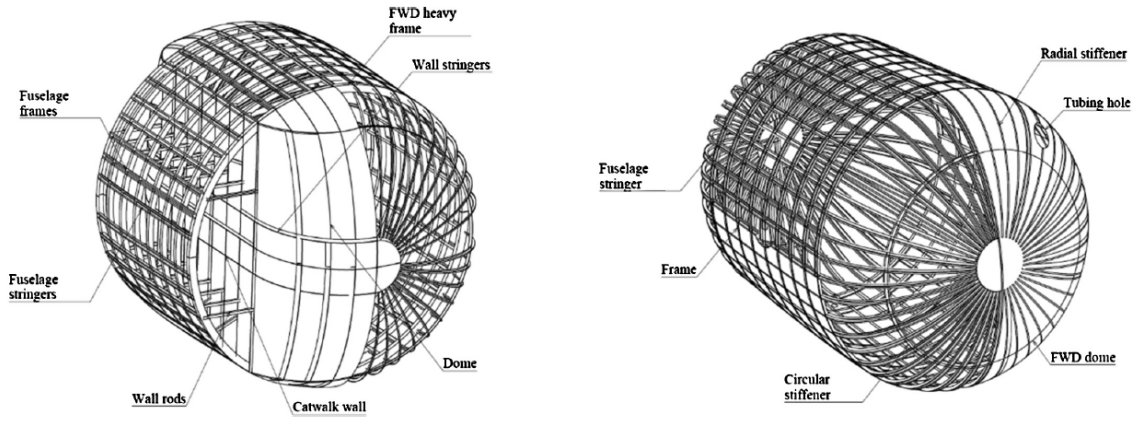


Fig. 4. Fuel tanks structural arrangement.

Figure 4.6: Fuel tank structural arrangement [22]

The determination of tank shape is an extensive process that entails more than merely calculating the hydrogen mass. Indeed, the pressure rise inside a tank filled with 100-percent saturated or supersaturated liquid is significantly higher than that of a tank filled with a two-phase mixture. The necessity for a significantly thicker insulation layer in the case of a tank filled with saturated or supersaturated liquid hydrogen (LH2) is a consequence of the greater pressure rise within the tank. This pressure rise, in turn, results in the requirement for a venting valve to be installed with the aim of avoiding overpressure and maintaining the structural integrity of the tank. Finally, allowance must be made for the volume of the tank.

Allowance for [%]	Brewer [7]	Cryoplane	Verstraete [48]
Tank contraction and expansion	0.9	-	0.9
Internal structure and equipment	0.6	0.5	0.6
Trapped and unusable fuel	0.3	1.0	0.6
Gas space for exit pipe	1.0	2.0	1.0
Total	1.8	3.5	3.1

Table 4.1: Allowance for different components

Tank Structural Layer Aluminum 2219-T87 is used for the tank skin due to the good relationship between strength and fracture toughness. This alloy has been widely used in cryogenic aerospace applications due to its easy weld-ability. Aluminum 7075-T6 is a strong and lightweight alloy used in structural members such as stringers, and frames that are subjected to higher stress levels than the skin. Additionally, this alloy is also employed in the catwalk wall skin due to the higher-pressure hoop stresses in this region. Stiffeners, vertical frames and diagonal ribs located in the catwalk are subjected to very high hoop stresses requiring the use of Ti-6Al-4V alloy [22]

To determine the tank wall thickness t_{wa} , the method from Barron [1] is adopted.

$$t_{wa} = \frac{p_{des} \cdot d_0}{2 \cdot \sigma_a \cdot e_w + 0.8 \cdot p_{des}} \quad (4.6)$$

where

- p_{des} is the pressure inside the tank equals to 0.172 MPa under the saturated liquid/gas condition;
- d_0 stands for the outside diameter of the shell;
- σ_a accounts the allowable tank wall stress;
- e_w expresses the weld efficiency which is taken for this case as 80%

Tank Insulation The LH2 is stored at low temperatures in the form of a saturated liquid/gas mixture. During the flight, the tank is subjected to heat input from the surrounding environment, resulting in fluctuations in internal pressure. To minimise heat transfer, fluctuations in pressure must be regulated. The internal insulation system serves to prevent direct contact between the LH2 and the tank structure, maintaining the temperature at a level close to that of the ambient environment and thus avoiding the conduction of heat along the length of the stringers, frames and external supporting rods.

As outlined in the article *Development and validation of purged thermal protection systems for liquid hydrogen fuel tanks of hypersonic vehicles* [24], an additional consideration is the capacity of the insulation system to accommodate dimensional alterations resulting from thermal cycling induced by the introduction of cryogenic hydrogen. The thermal coefficient discrepancies between the components of the tank system represent a pivotal aspect in the design of such a system. Insulation also serves to prevent condensation and subsequent solidification of atmospheric gases onto the tank. This can be addressed through the use of either a vacuum-jacketed system or a purged system (such as a helium purged system), where a non-condensable gas has replaced the air.

Mital asserts that the permeation of hydrogen represents a pivotal challenge in the design of the tank. Due to their diminutive size, hydrogen molecules are particularly susceptible to permeating the tank wall.

In the case of integral tank structures, a number of potential solutions have been considered. In his proposal, Onorato [36] put forth the idea of a single-wall construction with foam insulation. Nevertheless, this solution presents challenges in terms of integration with the airframe and the insulation capabilities of the tank. A double-wall construction with multi-layer insulation, initially proposed by Brewer [7] and subsequently by Verstraete [48], should prove an effective solution to these issues.

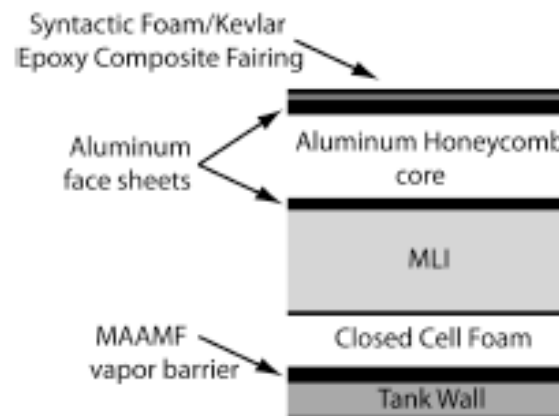


Figure 4.7: Tank structure for the multi layer insulation. Source [7]

An efficacious solution has been put forth by Montellano [37] wherein the inner tank assumes responsibility for the retention of hydrogen and the associated fuel containment loads, while the outer tank is connected to the adjacent airframe and bears the loads of the primary structure. With insulation positioned between the two tanks, the outer tank structure can be directly bolted to the primary airframe, thus circumventing issues associated with tank contraction and expansion, as well as heat conduction through the structure.

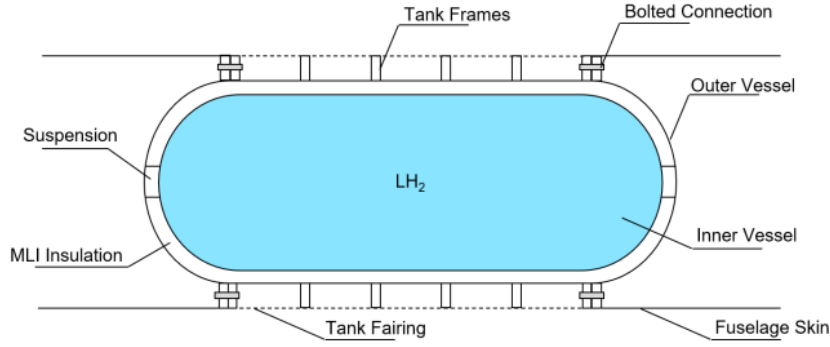


Figure 4.8: Tank integration onto aircraft structured proposed by Montellap. Source: [37]

The thickness of the insulation layer can be determined using the following equation [49]:

$$t_{insulation} = 2 \cdot \sqrt{\frac{k_{ins} t_{fl} (T_{int} - T_{LH_2})}{h_{LH_2} \cdot \rho_{ins}}} \quad (4.7)$$

where:

- k_{ins} is the thermal conductivity (Vacuum+MLI);
- t_{fl} defines the mission profile time;
- h_{LH_2} represents the enthalpy of vaporization of liquid hydrogen, equal to $447.60 \frac{kJ}{kg}$;
- T_{int} is the temperature at the external interface of the insulation;
- T_{LH_2} expresses the liquid hydrogen storage temperature;
- ρ_{ins} is the insulation density (Vacuum+MLI).

Tank Design for Regional Airliner Vestraete [48] consider the possibility for tank system for a regional aircraft with a simplified mission profile, with a total endurance of 5 hours. Three different options were considered.

- Single tank solution with an outer diameter of 2.42m;
- Twin tank, one at the front and one in the tail cone;
- Multiple tanks system at the top of the cabin and a single big tank in the tail cone.

The first solutions results in his study not feasible from a centre of gravity shifting during cruise point of view. Although this solution embodies the highest gravimetric efficiency i.e the lower weight. In fact the gravimetric index is defined as

$$\eta_{grav} = \frac{w_f}{w_f + w_{tank}} \quad (4.8)$$

where w_f is the fuel mass and w_{tank} is the mass of the tank structure.

The gravimetric efficiency of the single tank solution is illustrated in Figure 4.9, where the blue lines represent the polyurethane foam and the black ones represent rohacell. The full lines indicate the presence of metal tank walls, whereas the dashed lines denote a 25% weight reduction for composite materials, as cited in [44]. The figure demonstrates that the polyurethane foam provides a more lightweight solution for the tank design. The optimal venting pressure is approximately two bar, and the maximum gravimetric efficiency is observed between 62% and 70%.

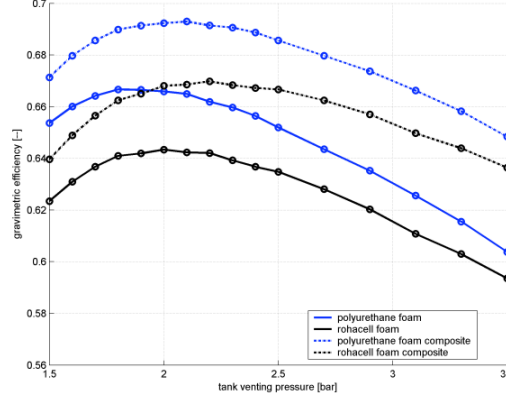


Figure 4.9: Gravimetric efficiency of a single tank option for a regional airliner [48]

4.4. Working Principles and Sizing of Fuel Cells

A fuel cell is an electrochemical device that directly converts the chemical energy of a fuel into electrical energy. This one-step process offers advantages over traditional combustion engines, including higher efficiency and compatibility with renewable sources like hydrogen for sustainable development [34]. While modern turbofans generate thrust primarily from the fan, ducted fans are a potential alternative, though they require larger, high-power-density electric motors. The most powerful aerospace-grade electric propulsion unit currently available is magniX's 650 kW magni650 [31], which powered the Universal Hydrogen Aircraft.

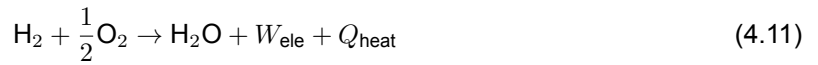
A fuel cell consists of an anode, a cathode, and an electrolyte. The electrodes are porous materials coated with a catalyst, often platinum in PEMFCs. Fig. 4.10 illustrates the PEMFC operation. Hydrogen is supplied to the anode, where it is oxidized:



The resulting hydrogen ions migrate through the electrolyte, while the electrons flow to the cathode through an external circuit. At the cathode, they react with oxygen to form water:



The overall reaction is:



Continuous heat and water removal is essential. The optimal PEMFC operating temperature is 25°C, with a theoretical efficiency of 83% [16]. Realistic efficiencies are 40-60%, with 50% being typical [35].

The fuel cell system includes the stack and its Balance of Plant (BoP) [32]. For this application, a PEMFC and a cryogenic hydrogen tank are used [48]. The sizing process, based on Massaro et al. [10], calculates the number of stacks and the hydrogen mass. The number of stacks is:

$$n_{\text{stack}}(h) = \left\lceil \frac{P_{\text{mission}}(h)}{\eta_{EM} P_{\text{stack,net}}(h)} \right\rceil \quad (4.12)$$

where $P_{\text{mission}}(h)$ is the mission power, η_{EM} is the electric motor efficiency, and $P_{\text{stack,net}}(h)$ is the net stack power.

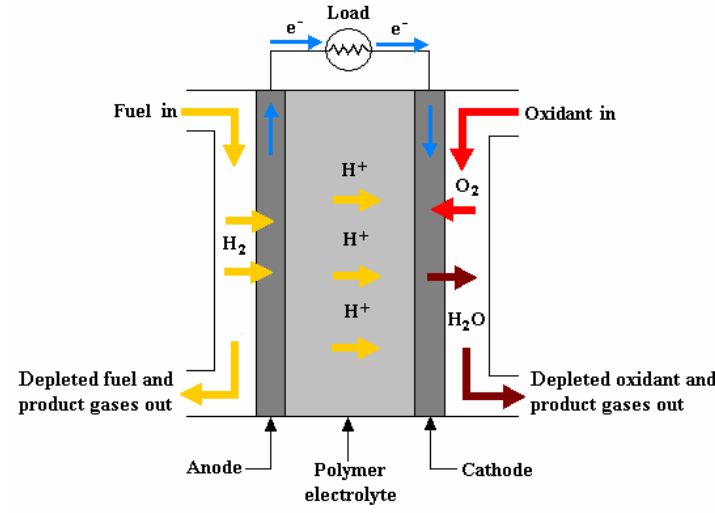


Figure 4.10: PEM fuel cell diagram. Source: [14]

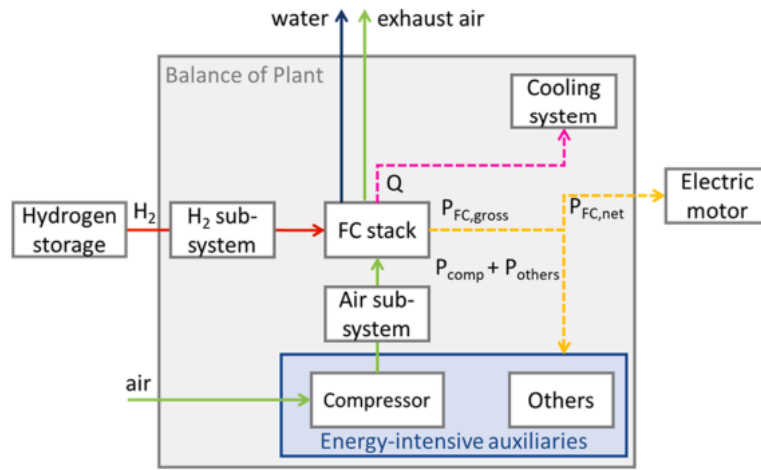


Figure 4.11: Fuel cell system architecture. Source: [32]

Stack Design and Performance Stack design determines cell area and number of cells. The stack power is:

$$P_{stack} = P_{fc} N_{cell} A_{cell} \quad (4.13)$$

where P_{fc} is the cell power density, N_{cell} is the number of cells, and A_{cell} is the cell area.

The net electrical power is:

$$P_{stack,net}(h) = P_{stack}(h) - P_{comp}(h) - P_{others} \quad (4.14)$$

where $P_{comp}(h)$ is the altitude-dependent compressor power and P_{others} is the power of other auxiliaries. The compressor power increases with altitude due to the decreasing air pressure.

System Weight and Hydrogen Mass The total weight of the fuel cell and propulsion system is:

$$W_{tot} = \frac{P_{stack,max} n_{stack}}{w_{FC}} + \frac{P_{comp,max} n_{stack}}{w_{compressor}} + A_{cooling} w_{cooling} + \frac{m_{H2}}{w_{H2,storage}} + \frac{P_{TO}}{\eta_{EM} w_{EM}} \quad (4.15)$$

Component	Parameter	Value	Unit
Fuel cell stack [39]	w_{FC}	3	kW/kg
Compressor [41]	w_{compr}	1.03	kW/kg
Cooling system [43]	$w_{cooling}$	1.08	kg/m ²
Hydrogen storage [12]	$w_{H_2, storage}$	0.22	kg _{H2} /kg _{storagesystem}
Electric motor [29]	w_{EM}	5.2	kW/kg

Table 4.2: Gravimetric indexes for the components of the electric propulsion system.

The required hydrogen mass is:

$$m_{H_2} = \frac{1}{10^3 LHV_{H_2}} \int_0^{t_{end}} \frac{P_{mission}(t)}{\eta_{EM} \eta_{net}(h)} dt \quad (4.16)$$

where t_{end} is the mission duration.

System Efficiency The fuel cell system efficiency is:

$$\eta_{net}(h) = \frac{P_{stack, net}(h)}{\dot{m}_{H_2, stack} LHV_{H_2} \times 10^3} \quad (4.17)$$

Figure 4.12 shows the system efficiency. The stack efficiency decreases with current. The system efficiency (without compressor) peaks due to auxiliary power. The overall efficiency (with compressor) is lower. Compressor power varies with altitude.

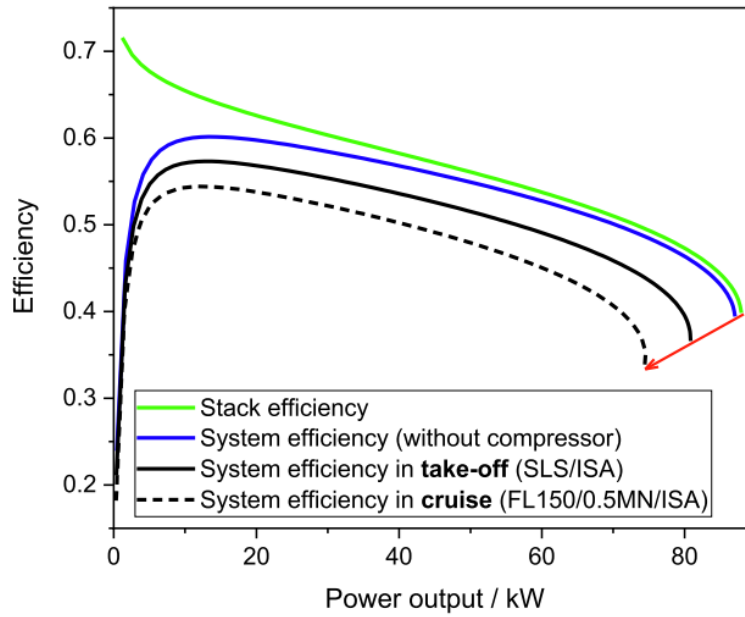


Figure 4.12: Fuel cell system efficiency curves as a function of power output. Source: [10]

5

Double-Hybrid Powertrain Modelling

In order to consider the potential coexistence of three distinct energy sources, namely kerosene, hydrogen and Batteries, it is necessary to develop a novel powertrain model to define the systems in the conceptual design phase. This model shall:

- include the key components of the powertrain, such as the gas turbine, fuel cell, electric motor and propellers/fans;
- be capable of evaluating the power flowing in and out of each component with minimal computational effort;
- Adapt to the different architecture illustrated in Chapter 2.1 and to the new ones that will emerge from the addition of hydrogen and fuel cells;
- Be sensitive to a number of double-hybrid system descriptors, to define the energy source splitting.

The obvious choice was to extend the system modelling for a single hybrid system and two district propulsion systems developed by De Vries [50], adding the hydrogen chain and the relative components and efficiencies. This would entail incorporating the hydrogen chain and the relevant components and efficiencies. Similarly to the De Vries model, the hypothesis is based on the assumption that the system is in a steady state, with a constant conversion/transmission efficiency assumed for each component. Furthermore, the impact of Battery state-of-charge on the maximum power output of the Batteries has not been considered. A fixed efficiency has been assumed for the hydrogen supply chain and fuel cell, irrespective of the flight conditions, and the same has been applied to the power management and distribution system (PMAD). The system is described by the following elements

- Energy sources: kerosene, hydrogen and Batteries;
- 1st propulsive line: gas turbine, fuel cell, electric motor, gearbox and the propeller(s)/fan(s);
- 2nd propulsive line: electric motor, gearbox and the propeller(s)/fan(s);
- Power management and distribution;
- Hydrogen supply chain and power divider.

Each component is associated with a constant efficiency. It is important to note that, at this juncture, the energy sources considered by the model are limited to the power flowing into and out of each component, rather than the energy required for a specific phase of the mission.

5.1. Architectures and Configurations

By combining different energy sources and powertrain elements in various ways, it is possible to define a series of different powertrain architectures and configurations. This list builds upon the work of Isikveren [28] and de Vries [50], who proposed additional architectures that rely on the integration of hydrogen combustion and fuel cells into the powertrain systems. A total of 28 distinct architectures

	Conventional	Turboelectric	Serial	Parallel	Partial Turboelectric	Serial/ parallel partial hybrid	Full-electric	Dual-electric
Number of possible configurations	3	3	4	5	3	1	6	3

Table 5.1: Number of possible configuration for each type of powertrain architecture

could be identified. Similarly, as has been done in previous literature, the various configurations can be grouped into eight distinct architectural categories. The configurations exhibit distinct differences in terms of combustion type (full-kerosene combustion, full-hydrogen combustion, mixed combustion), source of electric power (Battery, fuel cell, mixed) and the presence of both or either the first and second propulsive lines. It should be noted that a given power path can be either one-way or two-way. This implies that, for a given power path, power can flow in either direction. This is applicable to a Battery that can also be recharged, an engine that can operate as a windmill, and an electric motor that can operate as a generator. In the figures below, filled arrows represent the power path during nominal conditions, while dashed arrows represent other possible operating modes.

The serial parallel partial hybrid configuration represents the general case of all the others, and thus may be considered a limit case of the serial-parallel partial hybrid configuration. It would therefore be beneficial to identify three sources of energy hybrid system descriptors, which would allow for a clear representation of each of the 28 configurations, beginning with the serial parallel partial hybrid.

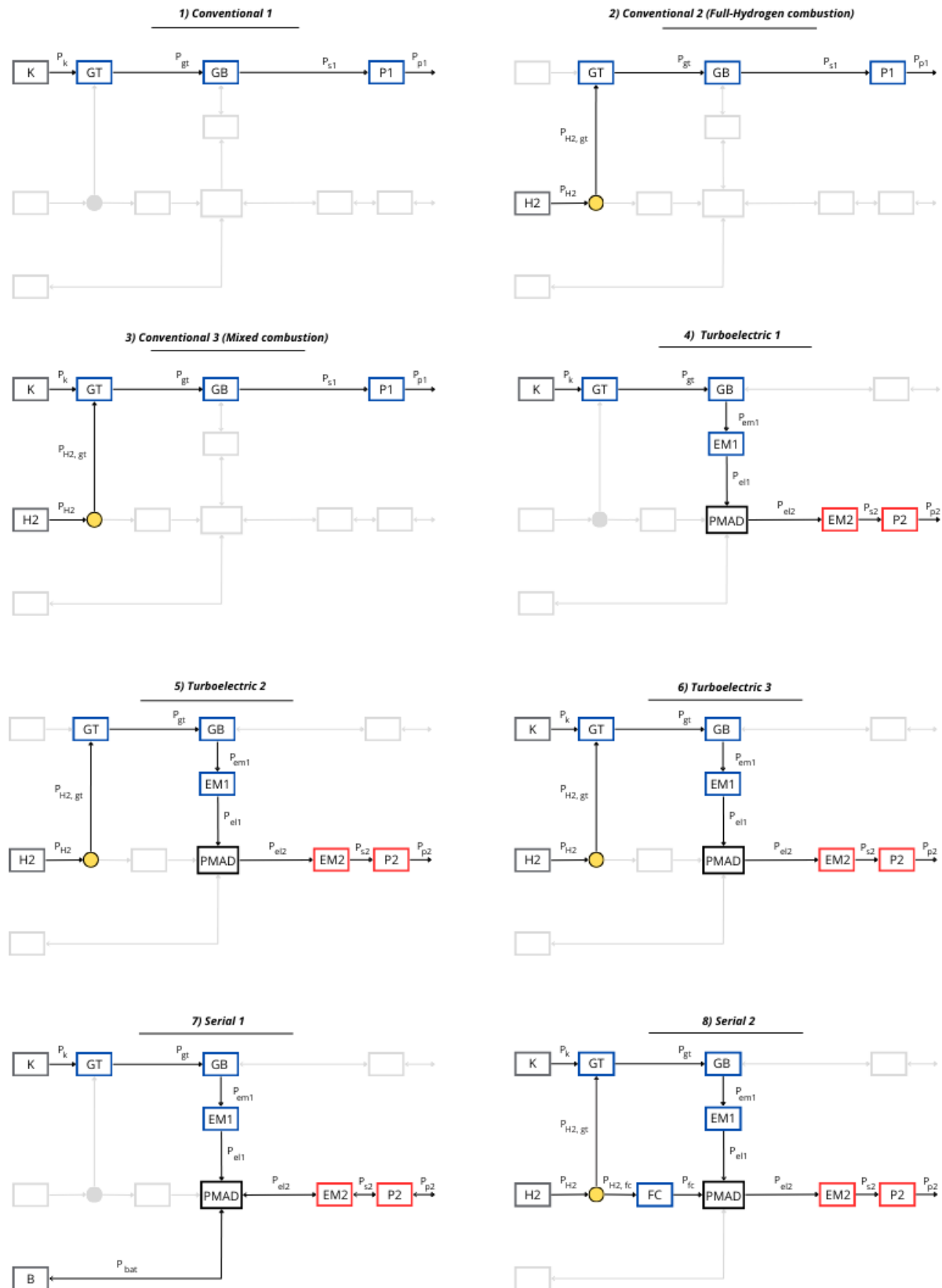


Figure 5.1: Configurations 1-8

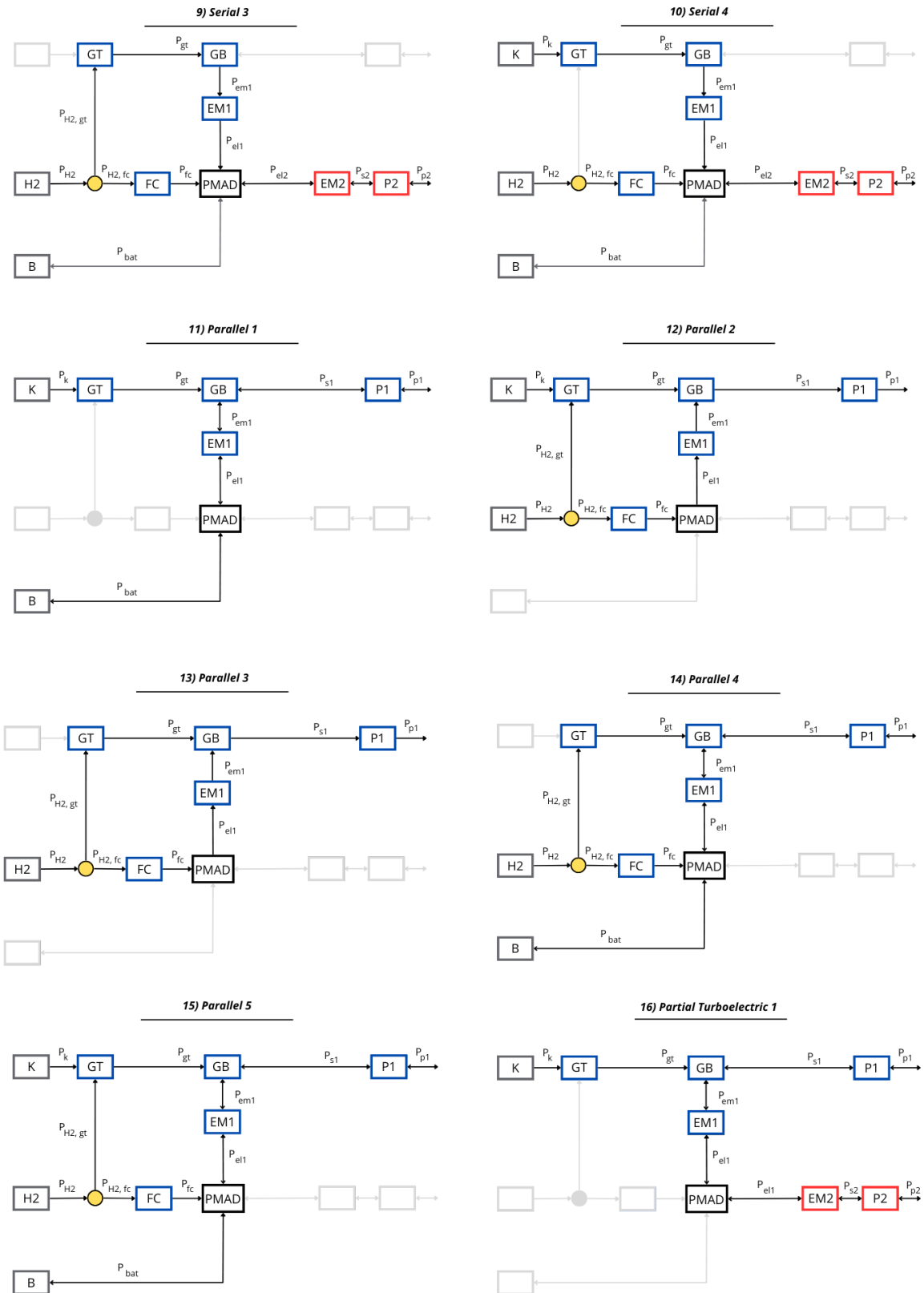


Figure 5.2: Configurations 9-16

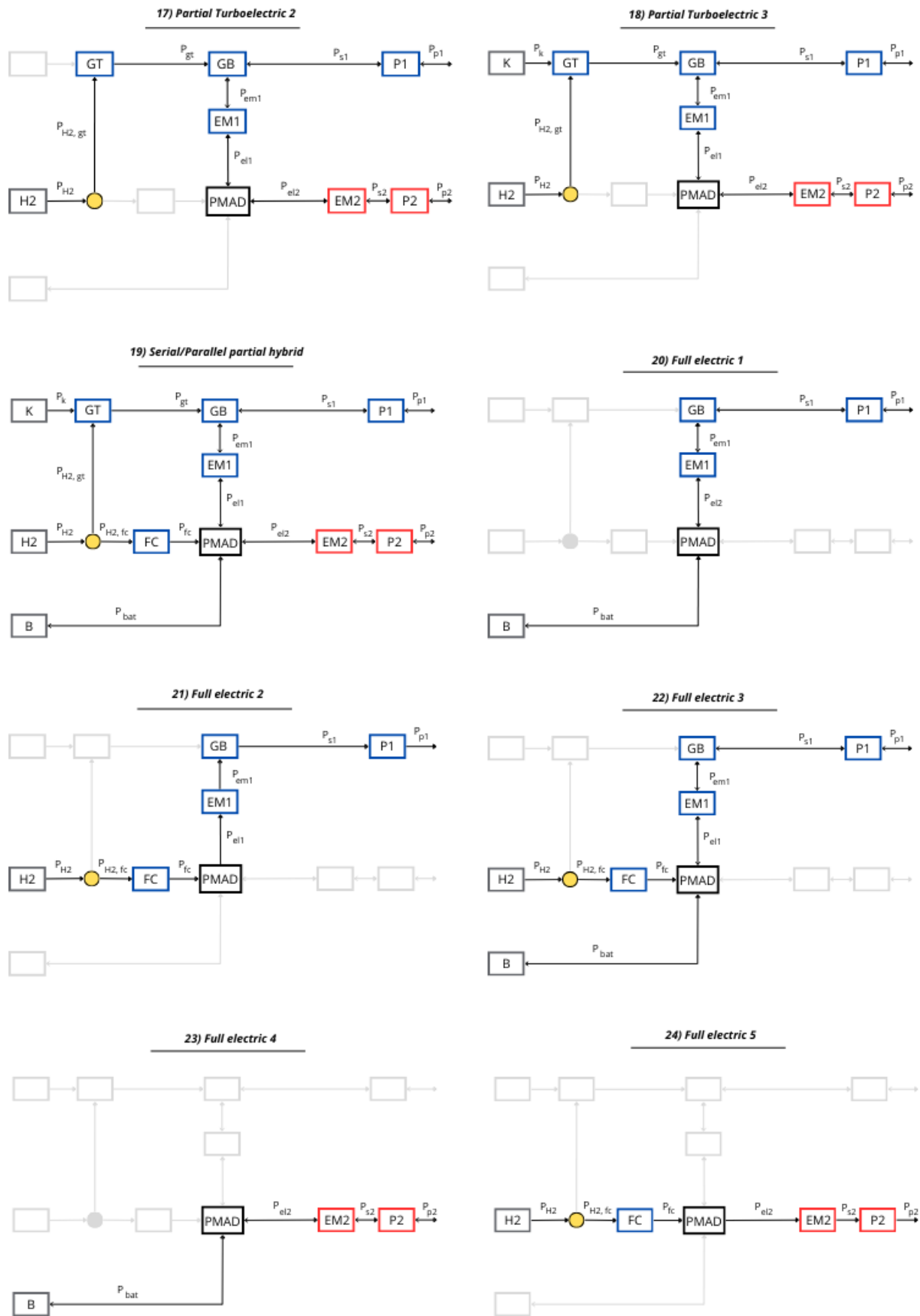


Figure 5.3: Configurations 17-24

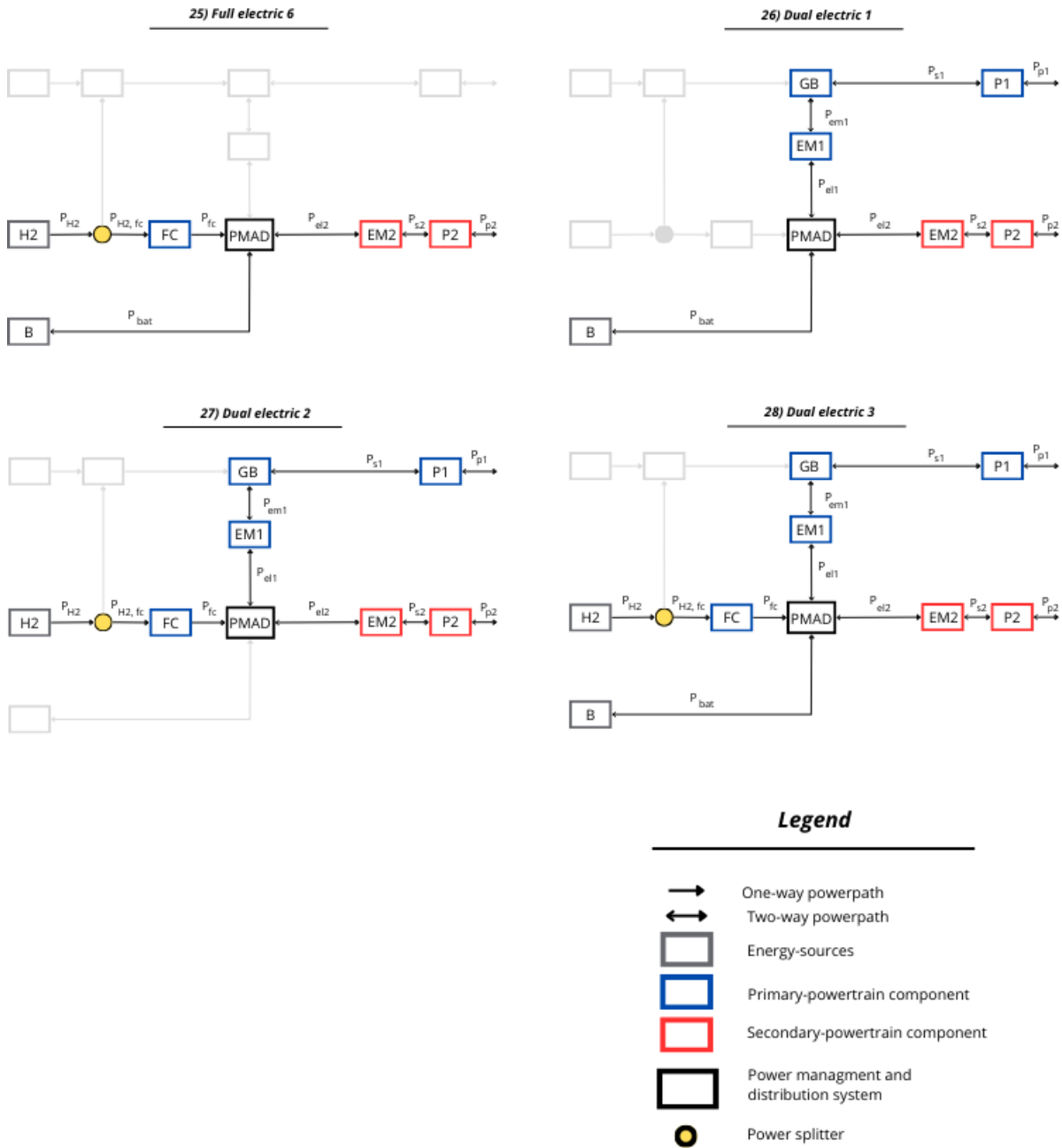


Figure 5.4: Configurations 25-28

5.2. Operating Modes

The majority of the 28 configurations demonstrate the capacity for operation in a manner that differs from the nominal condition, wherein both engines provide thrust, the Battery provides power, and the electric motors do not operate as generators. These operating modes are contingent upon the potential power flow that can be achieved through a double-path configuration for a given combination of power paths. Four distinct power paths can be operated in a double-path configuration, P_{EL1} , P_{EL2} , P_{s1} , P_{Bat} . However 16 distinct mathematical combinations exist, only 10 are physically viable. The green arrows illustrate a specific power flow exhibiting an inverse behaviour with respect to operating mode 1. In this instance, the power flow is regarded as negative. The green arrows illustrate a specific power flow exhibiting inverse behaviour with respect to operating mode 1. In this instance, the power flow is regarded as negative. It should be noted that at this point, all the operating modes do not take account of the actual feasibility in terms of technological boundaries and weight per each component, nor do

Configuration	OM1	OM2	OM3	OM4	OM10	OM6	OM7	OM8	OM9	OM5
Conventional	•									
Full-Hydrogen Combustion	•									
Mixed Combustion	•									
Conventional Turboelectric				•						
Hydrogen Turboelectric				•						
Mixed Turboelectric				•						
Serial 1				•		•	•			•
Serial 2				•						
Serial 3				•		•	•			•
Serial 4				•		•	•			•
Parallel 1	•					•		•		•
Parallel 2	•									
Parallel 3	•									
Parallel 4	•				•			•		•
Parallel 5	•				•			•		•
Partial Turboelectric 1		•		•			•			
Partial Turboelectric 2		•		•			•			
Partial Turboelectric 3		•		•			•			
SPPH	•	•	•	•	•	•	•	•	•	•
Full electric 1	•							•		
Full electric 2	•									
Full electric 3	•							•		
Full electric 4	•									•
Full electric 5	•									
Full electric 6	•		•			•	•			•
Dual electric 1	•	•	•				•	•	•	
Dual electric 2	•	•					•			
Dual electric 3	•	•	•		•		•	•	•	

Table 5.2: Operational Modes Associated with Aircraft Configurations

they account for the actual feasibility of a certain operating mode during a certain flight condition. In the operating modes 1 to 3 and 10, the surplus energy from the PMAD is redirected to the gearbox, which is situated throughout an electric motor, thereby generating shaft power. Conversely, in the aforementioned operating modes (4 to 9), the surplus shaft power from the gearbox is redirected to the PMAD through the utilisation of the electric motor as a generator. The operating modes determine whether the engines are used to provide thrust or to harvest power.

Table 5.2 illustrates the possible operating modes for each configuration. The ability of the SPPH configuration to be operated in all possible modes serves to confirm it can be considered as the general case for all other configurations.

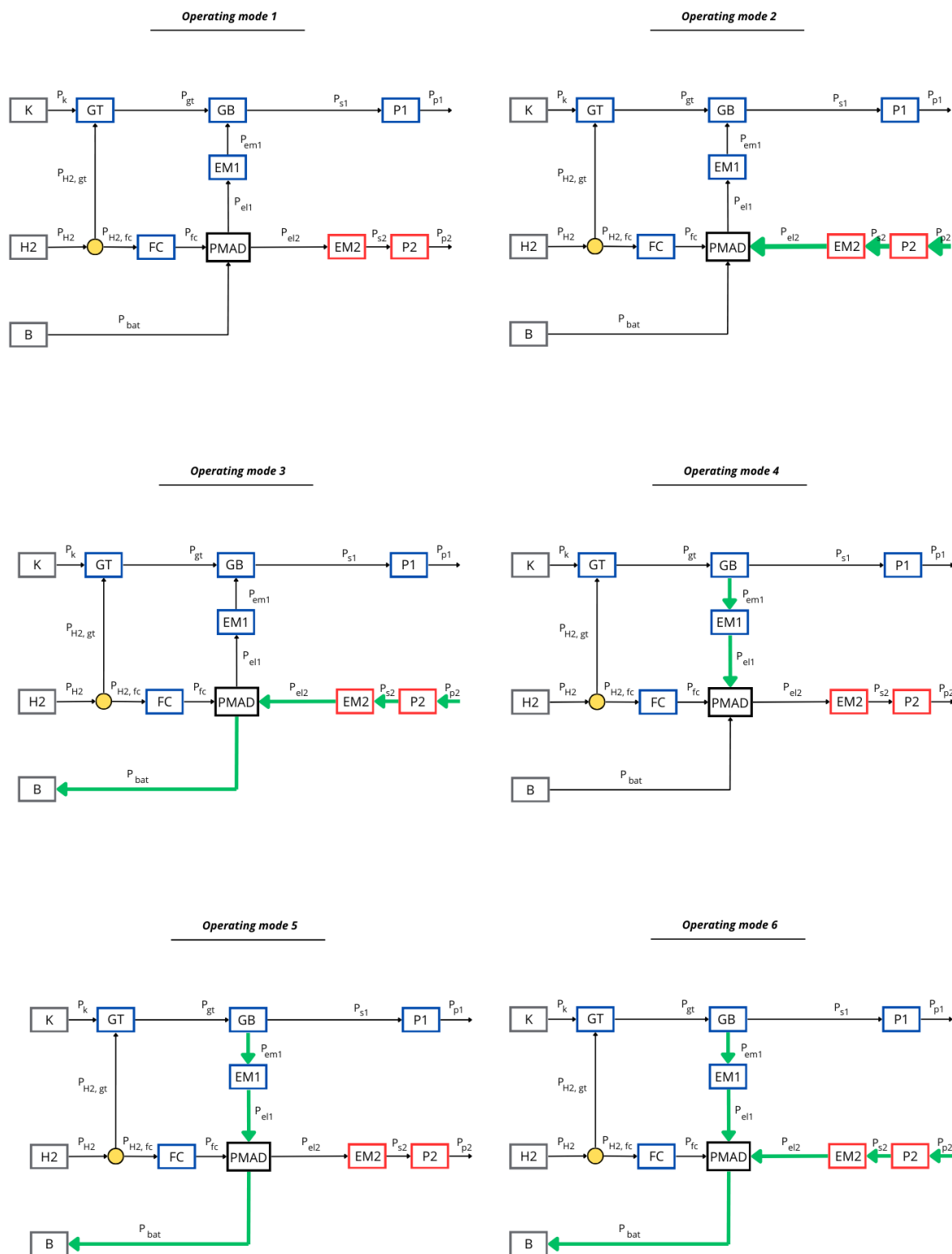


Figure 5.5: Operating modes 1-6

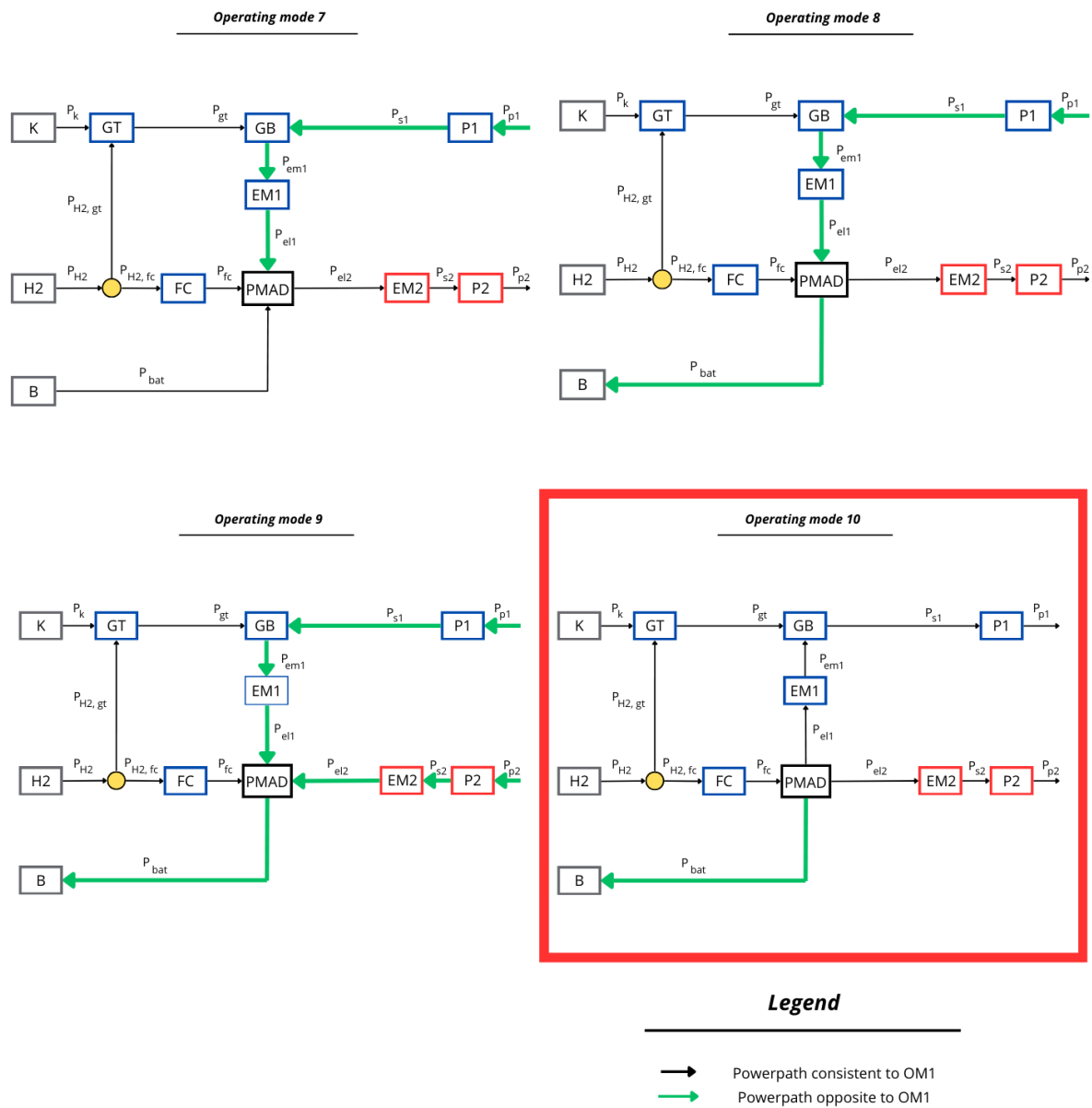


Figure 5.6: Operating modes 7-10. The red rectangle represent an addition possible operating mode respect to the current literature

5.3. Threefold Energy Storage Powertrain Descriptors

5.3.1. Power Control Parameters

The numerous potential configurations, based on different splitting of the source of energy and splitting of hydrogen between fuel cell and gas turbines, imply that a set of power control parameters are necessary to characterise the diverse powerflows of the system quantitatively.

The initial two parameters represent the power supplied by the Batteries and hydrogen, respectively, in relation to the total amount of power utilized. This represents an extension of the power ratio concerning Battery and kerosene, as defined by Isikveren [28], to encompass the combination of kerosene, hydrogen, and Batteries as a source of power.

$$\Phi_{Bat} = \frac{P_{Bat}}{P_{Bat} + P_{H2} + P_k}. \quad (5.1)$$

$$\Phi_{H2} = \frac{P_{H2}}{P_{Bat} + P_{H2} + P_k}. \quad (5.2)$$

The sum of these two parameters is constrained to a maximum value of 1, as they represent the energy source ratio. The limit value of 1 signifies that no kerosene is being utilised and that the engines are not harvesting power.

$$\Phi_{Bat} + \Phi_{H2} \leq 1 \quad (5.3)$$

The hydrogen supply ratio ξ is a measure of the quantity of hydrogen supplied to the fuel cell relative to the total quantity of hydrogen.

$$H2_{split} = \frac{P_{H2,FC}}{P_{H2,FC} + P_{H2,GT}} \quad (5.4)$$

Two distinct options are available for defining the electrical power partition. An alternative approach would be to define a specific partition coefficient or to utilise the shaft power ratio, as proposed by De Vries [50]. This final possibility was employed.

$$\varphi = \frac{P_{s2}}{P_{s1} + P_{s2}}. \quad (5.5)$$

The table below presents the range of power control parameters during nominal conditions (OM1, OM4).

5.3.2. Energy Control Parameters

The classic definition of fuel fraction fails to provide a direct correlation with the total quantity and species of energy stored onboard. Specifically, its application is limited to the determination of the total amount of cumulative propellant, excluding the specific proportions of hydrogen and kerosene, and the energy stored in the battery. Similarly, the energy fraction can only account for the total energy associated with the battery, hydrogen, and kerosene, without differentiating their individual contributions.

Consequently, the energy fraction should be complemented by two additional parameters to quantitatively describe the energy amount for each of the three energy sources: the Battery Energy Degree of Hybridization and the Fuel Energy Degree of Hybridization.

Defining the total fuel energy as $E_{fuel} = E_{H2} + E_k$, the Battery Degree of Hybridization (DOH_{Bat}) is defined as:

$$EDO H_{Bat} = \frac{E_{Bat}}{E_{Bat} + E_{fuel}} \quad (5.6)$$

To characterize the individual quantities of kerosene and hydrogen, the Fuel Energy Degree of Hybridization ($EDO H_{Fuel}$) is introduced:

$$EDOH_{Fuel} = \frac{E_{H2}}{E_{H2} + E_k} \quad (5.7)$$

5.4. Power Control Parameters along the Operating Modes

A crucial point of this powertrain modelling relies on the sign of the fourteen power flows themselves. For this purpose, the assumption of considering a power flow with a positive sign when coherent with the fluxes expressed in OM1, and vice versa, is carried out. Looking at the power control parameters, it's clear that the possibility of P_{Bat} , P_{s1} , and P_{s2} being either positive or negative has a crucial influence on these parameters' value range.

Considering the nominal scenario where P_{Bat} , P_{s1} , and P_{s2} assume a positive sign, which corresponds to OM1 and OM4, their range can be evaluated straightforwardly.

Table 5.3: Power Control Parameters Range during Nominal Conditions (OM1, OM4)

	Φ_{Bat}	Φ_{H2}	$H2_{split}$	φ
Nominal Conditions (OM1, OM4)	[0, 1]	[0, 1]	[0, 1]	[0, 1]

However, when one of the aforementioned changes sign, its behaviour becomes far from obvious, being naturally characterized by a singularity. This section examines the power control parameters Φ_{Bat} , Φ_{H2} and φ as functions in the diverse operating modes in order to explore their behaviour, range and singularities.

$H2_{split}$ is not mentioned since this power flow cannot reverse its sign, making it always fall between 0 and 1 independently of the operating mode.

5.4.1. Battery Being Recharged

To analyse the trend of the functions $\Phi_{Bat} = f(P_{Bat})$ and $\Phi_{H2} = f(P_{Bat})$, first it is evaluated the impact of the upper and lower limits of the power directed to the battery, in which the upper and lower limits correspond respectively to infinite and no power.

$$\lim_{P_{Bat} \rightarrow 0} \Phi_{Bat} = \lim_{P_{Bat} \rightarrow 0} \frac{P_{Bat}}{P_{Bat} + P_{H2} + P_k} = 0 \quad (5.8)$$

$$\lim_{P_{Bat} \rightarrow 0} \Phi_{H2} = \lim_{P_{Bat} \rightarrow 0} \frac{P_{H2}}{P_{Bat} + P_{H2} + P_k} = c > 0, \quad c \in \mathbb{R} \quad (5.9)$$

$$\lim_{P_{Bat} \rightarrow -\infty} \Phi_{Bat} = \lim_{P_{Bat} \rightarrow -\infty} \frac{P_{Bat}}{P_{Bat} + P_{H2} + P_k} = \nexists \quad (5.10)$$

$$\lim_{P_{Bat} \rightarrow -\infty} \Phi_{H2} = \lim_{P_{Bat} \rightarrow -\infty} \frac{P_{H2}}{P_{Bat} + P_{H2} + P_k} = \nexists \quad (5.11)$$

It results that when $P_{Bat} \rightarrow -\infty$ the limit does not exist. In fact, two distinct cases must be noted, depending on the operating modes.

When none of the engines harvest power (OM5, OM10) and battery is being recharged, the input power directed to the battery P_{Bat} must be of the same order of magnitude as the power required for charging. Obviously, both hydrogen and kerosene power can only be characterised by a positive sign and part of their power is diverted to the battery. Saying that, for this scenario $P_{H2} + P_k = -a \cdot P_{Bat} + b$, where the coefficient a is dependent upon the efficiency of the propulsive system in delivering power to the battery and parameter b represents the amount of power directed to the engines, consequently the resulting functions are:

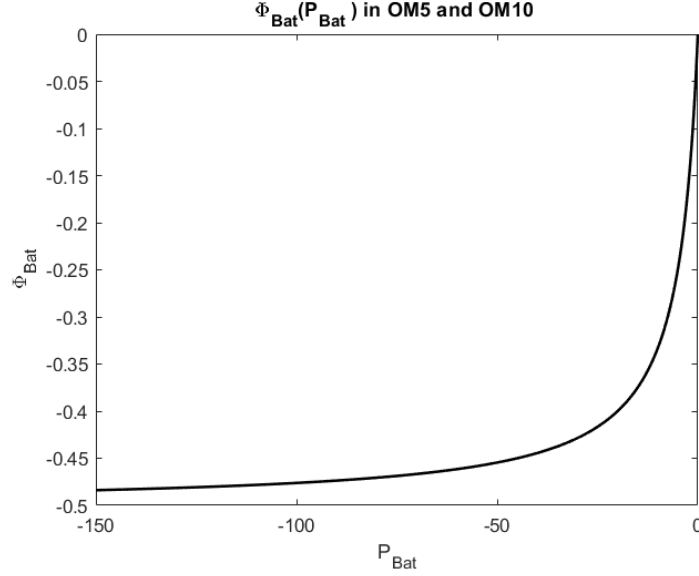


Figure 5.7: Qualitative graph of $\Phi_{Bat} = f(P_{Bat})$ in OM5 and OM10. a is assumed greater than 1 and b is positive.

$$\lim_{P_{Bat} \rightarrow -\infty} \Phi_{Bat} = \lim_{P_{Bat} \rightarrow -\infty} \frac{P_{Bat}}{P_{Bat} - a \cdot P_{Bat} + b} = c < 0, \quad c \in \mathbb{R} \quad [P_{Bat} < 0 \text{ in OM5, OM10}] \quad (5.12)$$

$$\lim_{P_{Bat} \rightarrow -\infty} \Phi_{H2}(P_{Bat}) = \lim_{P_{Bat} \rightarrow -\infty} \frac{P_{H2}}{P_{Bat} - a \cdot P_{Bat} + b} = 0^+, \quad [P_{Bat} < 0, \text{ OM5, OM10}] \quad (5.13)$$

In a real system, where the efficiencies cannot be equal to 1, $P_{Bat} \neq P_{H2} + P_k \cdot P$

In contrast, when one or both of the engines are harvesting power (OM3, OM6, OM8, OM9), the system is subject to a singularity. Indeed, for this case, the assumption that the sum of the power produced by hydrogen and kerosene must be of the same order of magnitude as the power directed to recharge the battery is no longer valid. In fact, theoretically, either propulsive line operating as a windmill could provide the powertrain with an amount of power with a diverse order of magnitude with respect to the power production of hydrogen and kerosene. This situation could happen, for instance, during the descent phase. As a consequence, the resulting function is:

$$\lim_{P_{Bat} \rightarrow -k} \Phi_{Bat}(P_{Bat}) = \lim_{P_{Bat} \rightarrow -k} \frac{P_{Bat}}{P_{Bat} + k} = \pm\infty, \quad [P_{Bat} < 0, \text{ OM3, OM6, OM7, OM8, OM9}] \quad (5.14)$$

$$\lim_{P_{Bat} \rightarrow -k} \Phi_{H2}(P_{Bat}) = \lim_{P_{Bat} \rightarrow -k} \frac{P_{H2}}{P_{Bat} + k}, \quad [P_{Bat} < 0, \text{ OM3, OM6, OM7, OM8, OM9}] \quad (5.15)$$

where k is the sum of $P_{H2} + P_k$. In this case,

$$\lim_{P_{Bat} \rightarrow -\infty} \Phi_{Bat}(P_{Bat}) = \lim_{P_{Bat} \rightarrow -\infty} \frac{P_{Bat}}{P_{Bat} + k} = 1^+, \quad [P_{Bat} < 0, \text{ OM3, OM6, OM8, OM9}] \quad (5.16)$$

$$\lim_{P_{Bat} \rightarrow -\infty} \Phi_{H2}(P_{Bat}) = \lim_{P_{Bat} \rightarrow -\infty} \frac{P_{H2}}{P_{Bat} + k} = 0^-, \quad [P_{Bat} < 0, \text{ OM3, OM6, OM8, OM9}] \quad (5.17)$$

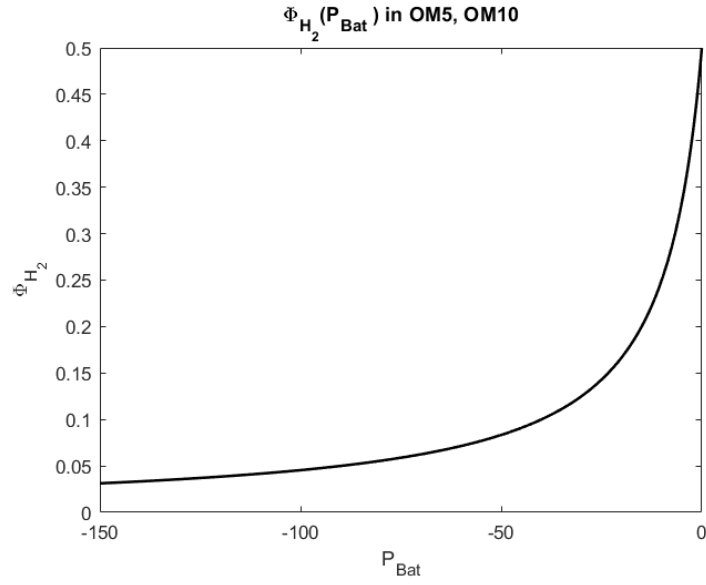


Figure 5.8: Qualitative graph of $\Phi_{H_2} = f(P_{Bat})$ in OM5 and OM10.

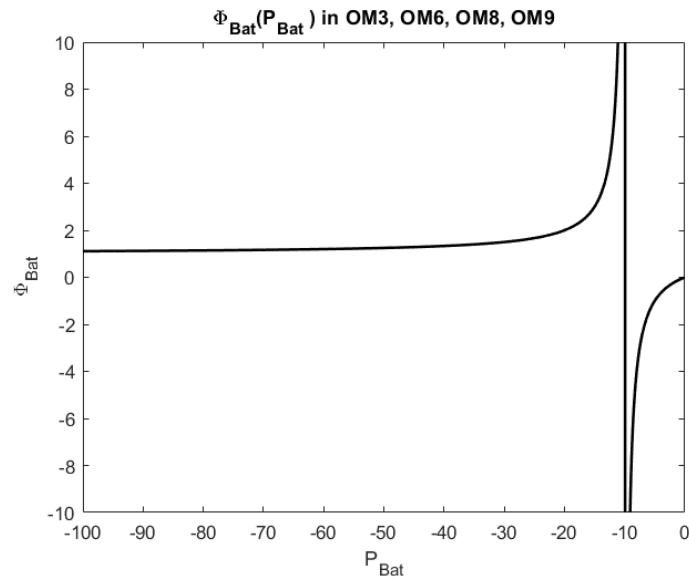


Figure 5.9: Qualitative graph of $\Phi_{Bat} = f(P_{Bat})$ in OM3, OM6, OM8, OM9. k is assumed positive.

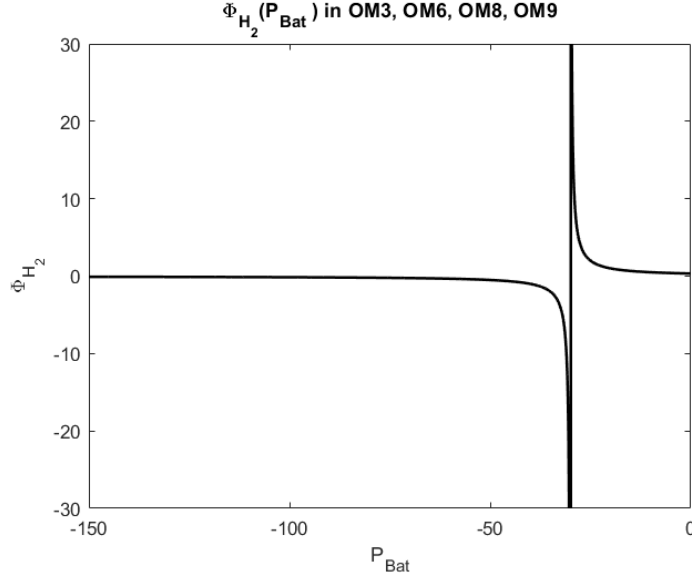


Figure 5.10: Qualitative graph of $\Phi_{H2} = f(P_{Bat})$ in OM3, OM6, OM8, OM9. k is assumed positive.

Since

$$P_{Bat} + P_{H2} + P_k = f(\eta, OM) \cdot P_p \quad (5.18)$$

where η is a matrix containing the powertrain components efficiencies, it can be demonstrated that a series of combinations of P_{tot} and η ultimately result in a singularity.

5.4.2. Engine Windmilling

The utilization of a single shaft power parameter is not able to correctly define P_{s1} and P_{s2} unless employed in conjunction with the total propulsive power P_p , and thus the total shaft power.

Defining the function:

$$\varphi(P_{s2}) = \frac{P_{s2}}{P_{s1} + P_{s2}} \quad (5.19)$$

a singularity clearly occurs when $\lim_{P_{s1} \rightarrow -P_{s2}} \varphi(P_{s2})$. Two different cases can be identified, depending on the sign of P_{s1} , and therefore the operating mode.

When $P_{s1} > 0$ that corresponds to OM1 to OM6 and OM10,

$$\lim_{P_{s2} \rightarrow -\infty} \varphi(P_{s2}) = \lim_{P_{s2} \rightarrow -\infty} \frac{P_{s2}}{P_{s1} + P_{s2}} = 1^+, \quad [\text{OM1 to OM6, OM10}] \quad (5.20)$$

$$\lim_{P_{s2} \rightarrow +\infty} \varphi(P_{s2}) = \lim_{P_{s2} \rightarrow +\infty} \frac{P_{s2}}{P_{s1} + P_{s2}} = 1^-, \quad [\text{OM1 to OM6, OM10}] \quad (5.21)$$

In contrast, if it assumed $P_{s1} < 0$, representing OM7 to OM9, the resulting fuctions are

$$\lim_{P_{s2} \rightarrow -\infty} \varphi(P_{s2}) = \lim_{P_{s2} \rightarrow -\infty} \frac{P_{s2}}{P_{s1} + P_{s2}} = 1^-, \quad [\text{OM7 to OM9}] \quad (5.22)$$

$$\lim_{P_{s2} \rightarrow +\infty} \varphi(P_{s2}) = \lim_{P_{s2} \rightarrow +\infty} \frac{P_{s2}}{P_{s1} + P_{s2}} = 1^+, \quad [\text{OM7 to OM9}] \quad (5.23)$$

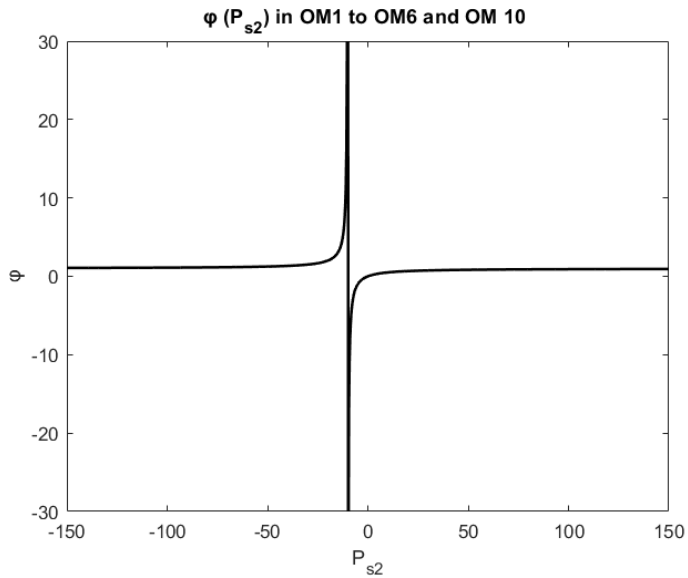


Figure 5.11: Qualitative graph of $\varphi = f(P_{s2})$ in OM1 to OM6 and OM10. P_{s1} is assumed positive.

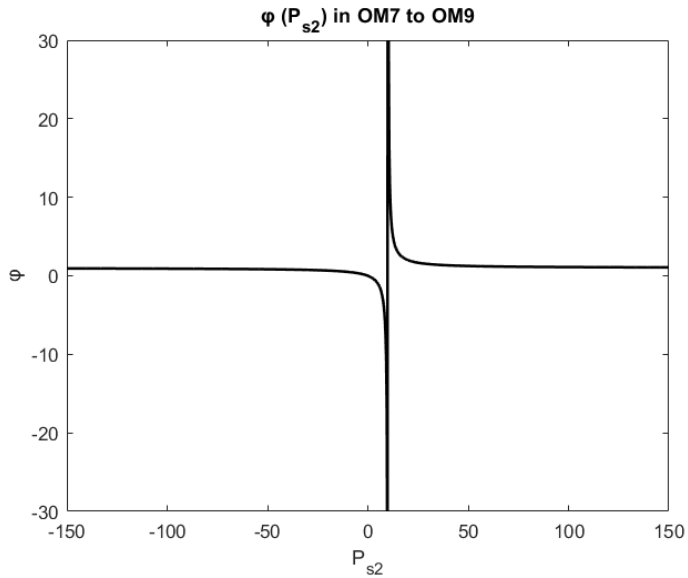


Figure 5.12: Qualitative graph of $\varphi(P_{s2})$ in OM7 to OM9. P_{s1} is assumed negative.

Summary table The following table presents a summary of the range of double-hybrid system descriptors in the context of the various operational modes.

	OM1	OM2	OM3	OM4
Φ_{Bat}	$[0, 1]$	$[0, 1]$	$(+1, +\infty), P_{tot} < 0$ $(-\infty, 0), P_{tot} > 0$	$[0, 1]$
Φ_{H2}	$[0, 1]$	$[0, 1]$	$(0, -\infty), P_{tot} < 0$ $(\infty, k), P_{tot} > 0$	$[0, 1]$
φ	$[0, 1]$	$(+1, +\infty), P_{s1} + P_{s2} < 0$ $(-\infty, 1), P_{s1} + P_{s2} > 0$	$(+1, +\infty), P_{s1} + P_{s2} < 0$ $(-\infty, 1), P_{s1} + P_{s2} > 0$	$[0, 1]$

Table 5.4: Control Parameters for Operating Modes 1-4

	OM5	OM6	OM7
Φ_{Bat}	$[-k, 0]$	$(+1, +\infty), P_{tot} < 0$ $(-\infty, 0), P_{tot} > 0$	$(+1, +\infty), P_{tot} < 0$ $(-\infty, 0), P_{tot} > 0$
Φ_{H2}	$(0, k]$	$(0, -\infty), P_{tot} < 0$ $(+\infty, k), P_{tot} > 0$	$(0, -\infty), P_{tot} < 0$ $(\infty, k), P_{tot} > 0$
φ	$[0, 1]$	$(+1, +\infty), P_{s1} + P_{s2} < 0$ $(-\infty, 1), P_{s1} + P_{s2} > 0$	$(+1, -\infty), P_{s1} + P_{s2} < 0$ $(+\infty, 1), P_{s1} + P_{s2} > 0$

Table 5.5: Power Control Parameters for Operating Modes 5-7

	OM8	OM9	OM10
Φ_{Bat}	$(+1, +\infty), P_{tot} < 0$ $(-\infty, 0), P_{tot} > 0$	$(1, +\infty)$	$[-k, 0]$
Φ_{H2}	$(0, -\infty), P_{tot} < 0$ $(\infty, k), P_{tot} > 0$	$(0, -\infty)$	$(0, k]$
φ	$(+1, -\infty), P_{s1} + P_{s2} < 0$ $(+\infty, 1), P_{s1} + P_{s2} > 0$	$[0, 1]$	$[0, 1]$

Table 5.6: Power Control Parameters for Operating Modes 8-10

Where k is a positive number.

5.5. Powertrain Equations

The Powertrain Equation can be considered as the real and proper core of the mathematical model for powertrain model. A total of 14 variables are involved in the SPPH configuration, each of which represents a power flow. Accordingly, in order to solve this system, it is necessary to derive 14 equations.

The initial nine equations illustrate the power flow into and out of each component, including the equations pertaining to the PMAD and GB nodes. With η individual component efficiency is represented, i.e. η_{GB} accounts the efficiency of the gearbox. Notably is Eq. 5, that corresponds to the conservation of the liquid hydrogen power from storage to the gas turbine or the fuel cell. The coefficient η_{SD} considers hydrogen power losses in this power flow due to evaporation and venting pressure.

Eq. 10 to 13 contain the double-hybrid system parameters described in the preceding section.

Equation 14 contains the constant term of the system, which is necessary for solving the linear system. The system is initially solved with respect to the total propulsive power.

Consequently, the system is completely defined. The equations can be written in matrix form

$$A\mathbf{x} = \mathbf{b}$$

where matrix A represents the powertrain architecture and its relative operative mode, x is the array containing the power paths and b a vector except for total propulsive power P_p

Equation Number	Power Path or Component
1	$P_{GT} = \eta_{GT,H2} \cdot P_{H2} + \eta_{GT,k} \cdot P_k$
2	$P_{p1} = \eta_{p1} \cdot P_{s1}$
3	$P_{p2} = \eta_{p2} \cdot P_{s2}$
4	$P_{em1} = \eta_{EM1} \cdot P_{EL1}$
5	$P_{H2} = \eta_{H2,SD} \cdot (P_{H2,GT} + P_{H2,FC})$
6	$P_{EL1} + P_{EL2} = \eta_{PMAD} \cdot (P_{FC} + P_{Bat})$
7	$P_{FC} = \eta_{FC} \cdot P_{H2,FC}$
8	$P_{s1} = \eta_{GB} \cdot (P_{GT} + P_{em1})$
9	$P_{s2} = \eta_{EM2} \cdot P_{EL2}$
10	$P_{s2} = P_{s1} \cdot \frac{\varphi}{1-\varphi}$
11	$P_{Bat} = \Phi_{Bat} \cdot (P_{Bat} + P_{H2} + P_k)$
12	$P_{H2} = \Phi_{H2} \cdot (P_{Bat} + P_{H2} + P_k)$
13	$P_{H2,FC} = P_{H2,GT} \cdot \frac{H2_{split}}{1-H2_{split}}$
14	$P_{p1} + P_{p2} = P_p$

Table 5.7: Powertrain Equations for Extended Powertrain System

$$\begin{bmatrix}
 1 & 0 & 0 & 0 & 0 & -\eta_{GT,H2} & 0 & 0 & -\eta_{GT,k} & 0 & 0 & 0 & 0 & 0 \\
 0 & 1 & 0 & 0 & 0 & 0 & 0 & 0 & 0 & 0 & 0 & 0 & -\eta_{p1} & 0 \\
 0 & 0 & 1 & 0 & 0 & 0 & 0 & 0 & 0 & 0 & 0 & 0 & 0 & -\eta_{p2} \\
 0 & 0 & 0 & 1 & 0 & 0 & 0 & 0 & 0 & -\eta_{EM1} & 0 & 0 & 0 & 0 \\
 0 & 0 & 0 & 0 & -\eta_{H2,SD} & 1 & 1 & 0 & 0 & 0 & 0 & 0 & 0 & 0 \\
 0 & 0 & 0 & 0 & 0 & 0 & 0 & -\eta_{PMAD} & 0 & 1 & 1 & -\eta_{PMAD} & 0 & 0 \\
 0 & 0 & 0 & 0 & 0 & 0 & -\eta_{FC} & 0 & 0 & 0 & 0 & 1 & 0 & 0 \\
 -\eta_{GB} & 0 & 0 & -\eta_{GB} & 0 & 0 & 0 & 0 & 0 & 0 & 0 & 0 & 1 & 0 \\
 0 & 0 & 0 & 0 & 0 & 0 & 0 & 0 & 0 & 0 & 0 & -\eta_{EM2} & 0 & 0 \\
 0 & 0 & 0 & 0 & 0 & 0 & 0 & 0 & 0 & 0 & 0 & 0 & 1 & -\varphi \\
 0 & 0 & 0 & 0 & -\Phi_{Bat} & 0 & 0 & 1 - \Phi_{Bat} & -\Phi_{Bat} & 0 & 0 & 0 & 0 & 0 \\
 0 & 0 & 0 & 0 & 1 - \Phi_{H2} & 0 & 0 & -\Phi_{H2} & -\Phi_{H2} & 0 & 0 & 0 & 0 & 0 \\
 0 & 0 & 0 & 0 & 0 & -H2_{split} & 1 - H2_{split} & 0 & 0 & 0 & 0 & 0 & 0 & 0 \\
 0 & 1 & 1 & 0 & 0 & 0 & 0 & 0 & 0 & 0 & 0 & 0 & 0 & 0
 \end{bmatrix}
 \begin{bmatrix}
 P_{GT} \\
 P_{p1} \\
 P_{p2} \\
 P_{em1} \\
 P_{H2} \\
 P_{H2,GT} \\
 P_{H2,FC} \\
 P_{Bat} \\
 P_k \\
 P_{EL1} \\
 P_{EL2} \\
 P_{FC} \\
 P_{s1} \\
 P_{s2}
 \end{bmatrix}
 =
 \begin{bmatrix}
 0 \\
 0 \\
 0 \\
 0 \\
 0 \\
 0 \\
 0 \\
 0 \\
 0 \\
 0 \\
 0 \\
 0 \\
 0 \\
 0
 \end{bmatrix}$$

Given that the initial nine equations of the matrix represent power flowing into and out of each component, including nodes and taking into account relative efficiency, it is necessary to adapt this set to each operating mode. If not, in cases where the power flow is in opposition to the nominal condition (OM1) would result in an erroneous assessment of the efficiency of each component, leading to an overestimation of the power flowing out in comparison to the power flowing in. Consequently, the node equations must also be modified. In light of the general criteria that a power flowing into a node is positive and flowing out is negative, in certain operating modes, the consideration of power flows opposite to the nominal condition as negative would lead to negative power flowing into the nodes, which would not respect the conservation of energy. To prevent this, the sign in the node equations is reversed when a power flow is negative.

Example 5.5.1

$$OM2 : \eta_{PMAD} \cdot \underbrace{(P_{FC})}_{>0} + \underbrace{(P_{EL2})}_{<0} + \underbrace{(P_{Bat})}_{>0} + \underbrace{(P_{EL1})}_{<0} = 0$$

In the operating mode, engine P2 operates as a windmill, thus its relative sign is negative. In order to maintain the conservation of energy, the following equation must be considered:

$$OM2 : \eta_{PMAD} \cdot \underbrace{(P_{FC})}_{>0} - \underbrace{(P_{EL2})}_{>0} + \underbrace{(P_{Bat})}_{>0} + \underbrace{(P_{EL1})}_{<0} = 0$$

The matrix A can be split in two sub-matrices,

$A_{9 \times 14}^{(TOP)}$ and $A_{5 \times 14}^{(BOT)}$ where the first represents the operating modes and the second the powertrain input scenario (PTIS), thus enabling the calculation of power splitting and the total amount of power.

The $A^{(TOP)}$ matrices for the ten different operating modes are presented below.

1. Battery, gas turbine and fuel cell provide power, both propulsive lines supply thrust, and excess power from the PMAD is diverted to the electric motor connected to the gearbox;

$$A_1^{(TOP)} = \begin{bmatrix} 1 & 0 & 0 & 0 & 0 & -\eta_{GT,H2} & 0 & 0 & -\eta_{GT,k} & 0 & 0 & 0 & 0 & 0 \\ 0 & 1 & 0 & 0 & 0 & 0 & 0 & 0 & 0 & 0 & 0 & 0 & -\eta_{p1} & 0 \\ 0 & 0 & 1 & 0 & 0 & 0 & 0 & 0 & 0 & 0 & 0 & 0 & 0 & -\eta_{p2} \\ 0 & 0 & 0 & 1 & 0 & 0 & 0 & 0 & 0 & -\eta_{EM1} & 0 & 0 & 0 & 0 \\ 0 & 0 & 0 & 0 & -\eta_{H2,SD} & 1 & 1 & 0 & 0 & 0 & 0 & 0 & 0 & 0 \\ 0 & 0 & 0 & 0 & 0 & 0 & 0 & -\eta_{PMAD} & 0 & 1 & 1 & -\eta_{PMAD} & 0 & 0 \\ 0 & 0 & 0 & 0 & 0 & 0 & -\eta_{FC} & 0 & 0 & 0 & 0 & 1 & 0 & 0 \\ -\eta_{GB} & 0 & 0 & -\eta_{GB} & 0 & 0 & 0 & 0 & 0 & 0 & 0 & 0 & 1 & 0 \\ 0 & 0 & 0 & 0 & 0 & 0 & 0 & 0 & 0 & 0 & -\eta_{EM2} & 0 & 0 & 1 \end{bmatrix}$$

2. Battery, gas turbine and fuel cell provide power, first propulsive line supplies thrust while second propulsive line harvests power. Excess power from the PMAD is diverted to the electric motor connected to the gearbox;

$$A_2^{(TOP)} = \begin{bmatrix} 1 & 0 & 0 & 0 & 0 & -\eta_{GT,H2} & 0 & 0 & -\eta_{GT,k} & 0 & 0 & 0 & 0 & 0 \\ 0 & 1 & 0 & 0 & 0 & 0 & 0 & 0 & 0 & 0 & 0 & 0 & -\eta_{p1} & 0 \\ 0 & 0 & -\eta_{p2} & 0 & 0 & 0 & 0 & 0 & 0 & 0 & 0 & 0 & 0 & 1 \\ 0 & 0 & 0 & 1 & 0 & 0 & 0 & 0 & 0 & -\eta_{EM1} & 0 & 0 & 0 & 0 \\ 0 & 0 & 0 & 0 & -\eta_{H2,SD} & 1 & 1 & 0 & 0 & 0 & 0 & 0 & 0 & 0 \\ 0 & 0 & 0 & 0 & 0 & 0 & 0 & -\eta_{PMAD} & 0 & 1 & \eta_{PMAD} & -\eta_{PMAD} & 0 & 0 \\ 0 & 0 & 0 & 0 & 0 & 0 & -\eta_{FC} & 0 & 0 & 0 & 0 & 1 & 0 & 0 \\ -\eta_{GB} & 0 & 0 & -\eta_{GB} & 0 & 0 & 0 & 0 & 0 & 0 & 0 & 0 & 1 & 0 \\ 0 & 0 & 0 & 0 & 0 & 0 & 0 & 0 & 0 & 0 & 1 & 0 & 0 & -\eta_{EM2} \end{bmatrix}$$

3. Gas turbine and fuel cell provide power, first propulsive line supplies thrust while second propulsive line harvests power. Excess power from the PMAD is diverted to the electric motor connected to the gearbox and to recharge the Battery;

$$A_3^{(TOP)} = \begin{bmatrix} 1 & 0 & 0 & 0 & 0 & -\eta_{GT,H2} & 0 & 0 & -\eta_{GT,k} & 0 & 0 & 0 & 0 & 0 \\ 0 & 1 & 0 & 0 & 0 & 0 & 0 & 0 & 0 & 0 & 0 & 0 & -\eta_{p1} & 0 \\ 0 & 0 & -\eta_{p2} & 0 & 0 & 0 & 0 & 0 & 0 & 0 & 0 & 0 & 0 & 1 \\ 0 & 0 & 0 & 1 & 0 & 0 & 0 & 0 & 0 & -\eta_{EM1} & 0 & 0 & 0 & 0 \\ 0 & 0 & 0 & 0 & -\eta_{H2,SD} & 1 & 1 & 0 & 0 & 0 & 0 & 0 & 0 & 0 \\ 0 & 0 & 0 & 0 & 0 & 0 & 0 & -1 & 0 & 1 & \eta_{PMAD} & -\eta_{PMAD} & 0 & 0 \\ 0 & 0 & 0 & 0 & 0 & 0 & -\eta_{FC} & 0 & 0 & 0 & 0 & 1 & 0 & 0 \\ -\eta_{GB} & 0 & 0 & -\eta_{GB} & 0 & 0 & 0 & 0 & 0 & 0 & 0 & 0 & 1 & 0 \\ 0 & 0 & 0 & 0 & 0 & 0 & 0 & 0 & 0 & 0 & 1 & 0 & 0 & -\eta_{EM2} \end{bmatrix}$$

4. Battery, gas turbine and fuel cell provide power, both propulsive lines supply thrust, and excess

power from the gearbox is diverted to the PMAD through the electric motor, acting as a generator;

$$A_4^{(TOP)} = \begin{bmatrix} 1 & 0 & 0 & 0 & -\eta_{GT,H2} & 0 & 0 & -\eta_{GT,k} & 0 & 0 & 0 & 0 & 0 & 0 \\ 0 & 1 & 0 & 0 & 0 & 0 & 0 & 0 & 0 & 0 & 0 & 0 & -\eta_{p1} & 0 \\ 0 & 0 & 1 & 0 & 0 & 0 & 0 & 0 & 0 & 0 & 0 & 0 & 0 & -\eta_{p2} \\ 0 & 0 & 0 & -\eta_{EM1} & 0 & 0 & 0 & 0 & 0 & 1 & 0 & 0 & 0 & 0 \\ 0 & 0 & 0 & 0 & -\eta_{H2,SD} & 1 & 1 & 0 & 0 & 0 & 0 & 0 & 0 & 0 \\ 0 & 0 & 0 & 0 & 0 & 0 & 0 & -\eta_{PMAD} & 0 & \eta_{PMAD} & 1 & -\eta_{PMAD} & 0 & 0 \\ 0 & 0 & 0 & 0 & 0 & 0 & -\eta_{FC} & 0 & 0 & 0 & 0 & 1 & 0 & 0 \\ -\eta_{GB} & 0 & 0 & -1 & 0 & 0 & 0 & 0 & 0 & 0 & 0 & 0 & 1 & 0 \\ 0 & 0 & 0 & 0 & 0 & 0 & 0 & 0 & 0 & 0 & -\eta_{EM2} & 0 & 0 & 1 \end{bmatrix}$$

5. Gas turbine and fuel cell provide power, both propulsive lines supply thrust, and excess power from the gearbox is diverted to the PMAD through the electric motor, acting as a generator as well as the excess power from the PMAD is diverted to the Battery to recharge it;

$$A_5^{(TOP)} = \begin{bmatrix} 1 & 0 & 0 & 0 & -\eta_{GT,H2} & 0 & 0 & -\eta_{GT,k} & 0 & 0 & 0 & 0 & 0 & 0 \\ 0 & 1 & 0 & 0 & 0 & 0 & 0 & 0 & 0 & 0 & 0 & 0 & -\eta_{p1} & 0 \\ 0 & 0 & 1 & 0 & 0 & 0 & 0 & 0 & 0 & 0 & 0 & 0 & 0 & -\eta_{p2} \\ 0 & 0 & 0 & -\eta_{EM1} & 0 & 0 & 0 & 0 & 0 & 1 & 0 & 0 & 0 & 0 \\ 0 & 0 & 0 & 0 & -\eta_{H2,SD} & 1 & 1 & 0 & 0 & 0 & 0 & 0 & 0 & 0 \\ 0 & 0 & 0 & 0 & 0 & 0 & 0 & -1 & 0 & \eta_{PMAD} & 1 & -\eta_{PMAD} & 0 & 0 \\ 0 & 0 & 0 & 0 & 0 & 0 & -\eta_{FC} & 0 & 0 & 0 & 0 & 1 & 0 & 0 \\ -\eta_{GB} & 0 & 0 & -1 & 0 & 0 & 0 & 0 & 0 & 0 & 0 & 0 & 1 & 0 \\ 0 & 0 & 0 & 0 & 0 & 0 & 0 & 0 & 0 & 0 & -\eta_{EM2} & 0 & 0 & 1 \end{bmatrix}$$

6. Gas turbine and fuel cell provide power, first propulsive line supplies thrust while second propulsive line harvest power. Excess power from the gearbox is diverted to the PMAD through the electric motor, acting as a generator. Battery is being recharged;

$$A_6^{(TOP)} = \begin{bmatrix} 1 & 0 & 0 & 0 & 0 & -\eta_{GT,H2} & 0 & 0 & -\eta_{GT,k} & 0 & 0 & 0 & 0 & 0 \\ 0 & 1 & 0 & 0 & 0 & 0 & 0 & 0 & 0 & 0 & 0 & 0 & -\eta_{p1} & 0 \\ 0 & 0 & -\eta_{p2} & 0 & 0 & 0 & 0 & 0 & 0 & 0 & 0 & 0 & 0 & 1 \\ 0 & 0 & 0 & -\eta_{EM1} & 0 & 0 & 0 & 0 & 0 & 1 & 0 & 0 & 0 & 0 \\ 0 & 0 & 0 & 0 & -\eta_{H2,SD} & 1 & 1 & 0 & 0 & 0 & 0 & 0 & 0 & 0 \\ 0 & 0 & 0 & 0 & 0 & 0 & 0 & -1 & 0 & \eta_{PMAD} & \eta_{PMAD} & -\eta_{PMAD} & 0 & 0 \\ 0 & 0 & 0 & 0 & 0 & 0 & -\eta_{FC} & 0 & 0 & 0 & 0 & 1 & 0 & 0 \\ -\eta_{GB} & 0 & 0 & -1 & 0 & 0 & 0 & 0 & 0 & 0 & 0 & 0 & 1 & 0 \\ 0 & 0 & 0 & 0 & 0 & 0 & 0 & 0 & 0 & 0 & 1 & 0 & 0 & -\eta_{EM2} \end{bmatrix}$$

7. Battery, gas turbine and fuel cell provide power, first propulsive line harvests power while second propulsive line supplies thrust. Power from the gearbox is diverted to the PMAD through the electric motor, acting as a generator;

$$A_7^{(TOP)} = \begin{bmatrix} 1 & 0 & 0 & 0 & 0 & -\eta_{GT,H2} & 0 & 0 & -\eta_{GT,k} & 0 & 0 & 0 & 0 & 0 \\ 0 & -\eta_{p1} & 0 & 0 & 0 & 0 & 0 & 0 & 0 & 0 & 0 & 0 & 1 & 0 \\ 0 & 0 & 1 & 0 & 0 & 0 & 0 & 0 & 0 & 0 & 0 & 0 & 0 & -\eta_{p2} \\ 0 & 0 & 0 & -\eta_{EM1} & 0 & 0 & 0 & 0 & 0 & 1 & 0 & 0 & 0 & 0 \\ 0 & 0 & 0 & 0 & -\eta_{H2,SD} & 1 & 1 & 0 & 0 & 0 & 0 & 0 & 0 & 0 \\ 0 & 0 & 0 & 0 & 0 & 0 & 0 & -\eta_{PMAD} & 0 & \eta_{PMAD} & 1 & -\eta_{PMAD} & 0 & 0 \\ 0 & 0 & 0 & 0 & 0 & 0 & -\eta_{FC} & 0 & 0 & 0 & 0 & 1 & 0 & 0 \\ -\eta_{GB} & 0 & 0 & -1 & 0 & 0 & 0 & 0 & 0 & 0 & 0 & 0 & \eta_{GB} & 0 \\ 0 & 0 & 0 & 0 & 0 & 0 & 0 & 0 & 0 & 0 & -\eta_{EM2} & 0 & 0 & 1 \end{bmatrix}$$

8. Gas turbine and fuel cell provide power, first propulsive line harvests power while second propulsive line supplies thrust. Power from the gearbox is diverted to the PMAD through the electric

motor, acting as a generator. Battery is being recharged;

$$A_8^{(TOP)} = \begin{bmatrix} 1 & 0 & 0 & 0 & 0 & -\eta_{GT,H2} & 0 & 0 & -\eta_{GT,k} & 0 & 0 & 0 & 0 & 0 & 0 \\ 0 & -\eta_{p1} & 0 & 0 & 0 & 0 & 0 & 0 & 0 & 0 & 0 & 0 & 0 & 1 & 0 \\ 0 & 0 & 1 & 0 & 0 & 0 & 0 & 0 & 0 & 0 & 0 & 0 & 0 & 0 & -\eta_{p2} \\ 0 & 0 & 0 & -\eta_{EM1} & 0 & 0 & 0 & 0 & 0 & 1 & 0 & 0 & 0 & 0 & 0 \\ 0 & 0 & 0 & 0 & -\eta_{H2,SD} & 1 & 1 & 0 & 0 & 0 & 0 & 0 & 0 & 0 & 0 \\ 0 & 0 & 0 & 0 & 0 & 0 & 0 & -1 & 0 & \eta_{PMAD} & 1 & -\eta_{PMAD} & 0 & 0 & 0 \\ 0 & 0 & 0 & 0 & 0 & 0 & -\eta_{FC} & 0 & 0 & 0 & 0 & 1 & 0 & 0 & 0 \\ -\eta_{GB} & 0 & 0 & -1 & 0 & 0 & 0 & 0 & 0 & 0 & 0 & 0 & \eta_{GB} & 0 & 0 \\ 0 & 0 & 0 & 0 & 0 & 0 & 0 & 0 & 0 & 0 & -\eta_{EM2} & 0 & 0 & 0 & 1 \end{bmatrix}$$

9. Gas turbine and fuel cell provide power, both primary and second propulsive line harvest power. Power from the gearbox is diverted to the PMAD through the electric motor, acting as a generator. Battery is being recharged;

$$A_9^{(TOP)} = \begin{bmatrix} 1 & 0 & 0 & 0 & 0 & -\eta_{GT,H2} & 0 & 0 & -\eta_{GT,k} & 0 & 0 & 0 & 0 & 0 & 0 \\ 0 & -\eta_{p1} & 0 & 0 & 0 & 0 & 0 & 0 & 0 & 0 & 0 & 0 & 0 & 1 & 0 \\ 0 & 0 & -\eta_{p2} & 0 & 0 & 0 & 0 & 0 & 0 & 0 & 0 & 0 & 0 & 0 & 1 \\ 0 & 0 & 0 & -\eta_{EM1} & 0 & 0 & 0 & 0 & 0 & 1 & 0 & 0 & 0 & 0 & 0 \\ 0 & 0 & 0 & 0 & -\eta_{H2,SD} & 1 & 1 & 0 & 0 & 0 & 0 & 0 & 0 & 0 & 0 \\ 0 & 0 & 0 & 0 & 0 & 0 & 0 & -1 & 0 & \eta_{PMAD} & \eta_{PMAD} & -\eta_{PMAD} & 0 & 0 & 0 \\ 0 & 0 & 0 & 0 & 0 & 0 & -\eta_{FC} & 0 & 0 & 0 & 0 & 1 & 0 & 0 & 0 \\ -\eta_{GB} & 0 & 0 & -1 & 0 & 0 & 0 & 0 & 0 & 0 & 0 & 0 & \eta_{GB} & 0 & 0 \\ 0 & 0 & 0 & 0 & 0 & 0 & 0 & 0 & 0 & 0 & 1 & 0 & 0 & -\eta_{EM2} & 0 \end{bmatrix}$$

10. Gas turbine and fuel cell provide power, both propulsive lines supply thrust, and excess power from the gearbox is diverted to the PMAD through the electric motor, acting as a generator. Battery is being recharged.

This operating mode was possible to be introduced thanks to the Double-Hybrid Powertrain and results to be an addition with respect to the previous literature. In Fig.5.6 it is underlined by a red rectangle.

$$A_{10}^{(TOP)} = \begin{bmatrix} 1 & 0 & 0 & 0 & 0 & -\eta_{GT,H2} & 0 & 0 & -\eta_{GT,k} & 0 & 0 & 0 & 0 & 0 & 0 \\ 0 & 1 & 0 & 0 & 0 & 0 & 0 & 0 & 0 & 0 & 0 & 0 & -\eta_{p1} & 0 & 0 \\ 0 & 0 & 1 & 0 & 0 & 0 & 0 & 0 & 0 & 0 & 0 & 0 & 0 & -\eta_{p2} & 0 \\ 0 & 0 & 0 & 1 & 0 & 0 & 0 & 0 & 0 & -\eta_{EM1} & 0 & 0 & 0 & 0 & 0 \\ 0 & 0 & 0 & 0 & -\eta_{H2,SD} & 1 & 1 & 0 & 0 & 0 & 0 & 0 & 0 & 0 & 0 \\ 0 & 0 & 0 & 0 & 0 & 0 & 0 & -1 & 0 & 1 & 1 & -\eta_{PMAD} & 0 & 0 & 0 \\ 0 & 0 & 0 & 0 & 0 & 0 & -\eta_{FC} & 0 & 0 & 0 & 0 & 1 & 0 & 0 & 0 \\ -\eta_{GB} & 0 & 0 & -\eta_{GB} & 0 & 0 & 0 & 0 & 0 & 0 & 0 & 0 & 1 & 0 & 0 \\ 0 & 0 & 0 & 0 & 0 & 0 & 0 & 0 & 0 & 0 & -\eta_{EM2} & 0 & 0 & 0 & 1 \end{bmatrix}$$

5.6. Powertrain Input Scenario

In order to solve the system, five propulsive inputs are required. However, different formulations can be adopted to describe the propulsive input, depending on the Powertrain Input Scenario (PTIS). The first propulsive input scenario refers to the basic formulation of the powertrain power control parameters.

$$PTIS_1 : [\varphi, \Phi_{Bat}, \Phi_{H2}, H2_{split}, P_p]. \quad (5.24)$$

A simple analysis indicates that it is possible to substitute the shaft power ratio, represented by the variable φ , provided that the propulsive powers of both the primary and secondary propulsive lines, represented by the variables P_{p1} and P_{p2} , respectively, are known. In this case, the resulting array of necessary inputs is given by:

$$PTIS_2 = [\Phi_{Bat}, \Phi_{H2}, H2_{split}, P_{p1}, P_{p2}] \quad (5.25)$$

and the overall matrix system becomes

$$\begin{bmatrix} 1 & 0 & 0 & 0 & 0 & -\eta_{GT,H2} & 0 & 0 & -\eta_{GT,k} & 0 & 0 & 0 & 0 & 0 & 0 \\ 0 & 1 & 0 & 0 & 0 & 0 & 0 & 0 & 0 & 0 & 0 & 0 & -\eta_{p1} & 0 & 0 \\ 0 & 0 & 1 & 0 & 0 & 0 & 0 & 0 & 0 & 0 & 0 & 0 & 0 & -\eta_{p2} & 0 \\ 0 & 0 & 0 & 1 & 0 & 0 & 0 & 0 & 0 & 0 & -\eta_{EM1} & 0 & 0 & 0 & 0 \\ 0 & 0 & 0 & 0 & -\eta_{H2,SD} & 1 & 1 & 0 & 0 & 0 & 0 & 0 & 0 & 0 & 0 \\ 0 & 0 & 0 & 0 & 0 & 0 & 0 & -\eta_{PMAD} & 0 & 1 & 1 & -\eta_{PMAD} & 0 & 0 & 0 \\ 0 & 0 & 0 & 0 & 0 & 0 & -\eta_{FC} & 0 & 0 & 0 & 0 & 1 & 0 & 0 & 0 \\ -\eta_{GB} & 0 & 0 & -\eta_{GB} & 0 & 0 & 0 & 0 & 0 & 0 & 0 & 0 & 1 & 0 & 0 \\ 0 & 0 & 0 & 0 & 0 & 0 & 0 & 0 & 0 & 0 & -\eta_{EM2} & 0 & 0 & 1 & 0 \\ 0 & 0 & 0 & 0 & -\Phi_{Bat} & 0 & 0 & 1 - \Phi_{Bat} & -\Phi_{Bat} & 0 & 0 & 0 & 0 & 0 & 0 \\ 0 & 0 & 0 & 0 & 1 - \Phi_{H2} & 0 & 0 & -\Phi_{H2} & -\Phi_{H2} & 0 & 0 & 0 & 0 & 0 & 0 \\ 0 & 0 & 0 & 0 & 0 & -H2_{split} & 1 - H2_{split} & 0 & 0 & 0 & 0 & 0 & 0 & 0 & 0 \\ 0 & 1 & 0 & 0 & 0 & 0 & 0 & 0 & 0 & 0 & 0 & 0 & 0 & 0 & 0 \\ 0 & 0 & 1 & 0 & 0 & 0 & 0 & 0 & 0 & 0 & 0 & 0 & 0 & 0 & 0 \end{bmatrix} \begin{bmatrix} P_{GT} \\ P_{p1} \\ P_{p2} \\ P_{em1} \\ P_{H2} \\ P_{H2,GT} \\ P_{H2,FC} \\ P_{Bat} \\ P_k \\ P_{EL1} \\ P_{EL2} \\ P_{FC} \\ P_{s1} \\ P_{s2} \end{bmatrix} = \begin{bmatrix} 0 \\ 0 \\ 0 \\ 0 \\ 0 \\ 0 \\ 0 \\ 0 \\ 0 \\ 0 \\ 0 \\ 0 \\ P_{p1} \\ P_{p2} \end{bmatrix}$$

An additional approach would be to consider the throttle setting and the total shaft-installed power (if available). Indeed, an appropriate description of the aircraft's overall throttle setting, irrespective of the source of the power, would be:

$$\xi = \frac{P_{s1} + P_{s2}}{P_{s1,inst,corr} + P_{s2,inst,corr}} \quad (5.26)$$

where P_{s1} and P_{s2} are the actual shaft power, and $P_{s1,inst,corr}$ and $P_{s2,inst,corr}$ are the corrected installed shaft power by means of altitude and velocity. This correction is applied to the power produced by the gas turbine. The approximate relationship between sea-level static shaft power and shaft power at flight condition is as follows:

$$P_{s1,inst}^{(Corr)} + P_{inst}^{(corr)} = (P_{s1,inst}^{SL} + P_{s2,inst}^{SL}) \cdot \left(\frac{P_{GT} \cdot f(h, M)}{P_{GT} + P_{FC} + P_{Bat}} + \frac{P_{FC} + P_{Bat}}{P_{GT} + P_{FC} + P_{Bat}} \right) \quad (5.27)$$

The input array results to be

$$PTIS_3 = [\varphi, \Phi_{Bat}, \Phi_{H2}, H2_{split}, \xi] \quad (5.28)$$

and the relative matrix equation systems:

$$\begin{bmatrix} 1 & 0 & 0 & 0 & 0 & -\eta_{GT,H2} & 0 & 0 & -\eta_{GT,k} & 0 & 0 & 0 & 0 & 0 & 0 \\ 0 & 1 & 0 & 0 & 0 & 0 & 0 & 0 & 0 & 0 & 0 & 0 & -\eta_{p1} & 0 & 0 \\ 0 & 0 & 1 & 0 & 0 & 0 & 0 & 0 & 0 & 0 & 0 & 0 & 0 & -\eta_{p2} & 0 \\ 0 & 0 & 0 & 1 & 0 & 0 & 0 & 0 & 0 & 0 & -\eta_{EM1} & 0 & 0 & 0 & 0 \\ 0 & 0 & 0 & 0 & -\eta_{H2,SD} & 1 & 1 & 0 & 0 & 0 & 0 & 0 & 0 & 0 & 0 \\ 0 & 0 & 0 & 0 & 0 & 0 & 0 & -\eta_{PMAD} & 0 & 1 & 1 & -\eta_{PMAD} & 0 & 0 & 0 \\ 0 & 0 & 0 & 0 & 0 & 0 & -\eta_{FC} & 0 & 0 & 0 & 0 & 1 & 0 & 0 & 0 \\ -\eta_{GB} & 0 & 0 & -\eta_{GB} & 0 & 0 & 0 & 0 & 0 & 0 & 0 & 0 & 1 & 0 & 0 \\ 0 & 0 & 0 & 0 & 0 & 0 & 0 & 0 & 0 & 0 & -\eta_{EM2} & 0 & 0 & 1 & 0 \\ 0 & 0 & 0 & 0 & 0 & 0 & 0 & 0 & 0 & 0 & 0 & -\varphi & 1 - \varphi & 0 & 0 \\ 0 & 0 & 0 & 0 & -\Phi_{Bat} & 0 & 0 & 1 - \Phi_{Bat} & -\Phi_{Bat} & 0 & 0 & 0 & 0 & 0 & 0 \\ 0 & 0 & 0 & 0 & 1 - \Phi_{H2} & 0 & 0 & -\Phi_{H2} & -\Phi_{H2} & 0 & 0 & 0 & 0 & 0 & 0 \\ 0 & 0 & 0 & 0 & 0 & -H2_{split} & 1 - H2_{split} & 0 & 0 & 0 & 0 & 0 & 0 & 0 & 0 \\ 0 & 0 & 0 & 0 & 0 & 0 & 0 & 0 & 0 & 0 & 0 & 0 & 1 & 1 & 1 \end{bmatrix} \begin{bmatrix} P_{GT} \\ P_{p1} \\ P_{p2} \\ P_{em1} \\ P_{H2} \\ P_{H2,GT} \\ P_{H2,FC} \\ P_{Bat} \\ P_k \\ P_{EL1} \\ P_{EL2} \\ P_{FC} \\ P_{s1} \\ P_{s2} \end{bmatrix} = \begin{bmatrix} 0 \\ 0 \\ 0 \\ 0 \\ 0 \\ 0 \\ 0 \\ 0 \\ 0 \\ 0 \\ 0 \\ 0 \\ \xi \cdot (P_{s1,inst} + P_{s2,inst}) \end{bmatrix}$$

Lastly, it is necessary to define the individual component throttle setting and their relative installed power. It should be noted that three different throttle settings for power source components can be defined, respectively, for the gas turbine, fuel cell, and Battery.

$$\xi_{GT} = \frac{P_{GT}}{P_{GT,inst}^{(corr)}}; \xi_{FC} = \frac{P_{FC}}{P_{FC,inst}^{(corr)}}; \xi_{Bat} = \frac{P_{Bat}}{P_{Bat,inst}^{(corr)}} \quad (5.29)$$

The maximum power of the aforementioned components is equal to the sea-level installed power, except for the gas turbine, where the maximum power is related to the installed sea-level static power by means of altitude and altitude, as previously demonstrated.

The input array associated with Powertrain Input Scenario 4 is:

$$PTIS_4 = [\xi_{GT}, \xi_{FC}, \xi_{Bat}, H2_{split}, \varphi] \quad (5.30)$$

and the relative equation system:

$$\begin{bmatrix} 1 & 0 & 0 & 0 & 0 & -\eta_{GT,H2} & 0 & 0 & -\eta_{GT,k} & 0 & 0 & 0 & 0 & 0 & 0 \\ 0 & 1 & 0 & 0 & 0 & 0 & 0 & 0 & 0 & 0 & 0 & 0 & -\eta_{p1} & 0 & 0 \\ 0 & 0 & 1 & 0 & 0 & 0 & 0 & 0 & 0 & 0 & 0 & 0 & 0 & -\eta_{p2} & 0 \\ 0 & 0 & 0 & 1 & 0 & 0 & 0 & 0 & 0 & -\eta_{EM1} & 0 & 0 & 0 & 0 & 0 \\ 0 & 0 & 0 & 0 & -\eta_{H2,SD} & 1 & 1 & 0 & 0 & 0 & 0 & 0 & 0 & 0 & 0 \\ 0 & 0 & 0 & 0 & 0 & 0 & 0 & -\eta_{PMAD} & 0 & 1 & 1 & -\eta_{PMAD} & 0 & 0 & 0 \\ 0 & 0 & 0 & 0 & 0 & 0 & -\eta_{FC} & 0 & 0 & 0 & 0 & 1 & 0 & 0 & 0 \\ -\eta_{GB} & 0 & 0 & -\eta_{GB} & 0 & 0 & 0 & 0 & 0 & 0 & 0 & 0 & 1 & 0 & 0 \\ 0 & 0 & 0 & 0 & 0 & 0 & 0 & 0 & 0 & 0 & -\eta_{EM2} & 0 & 0 & 1 & 0 \\ 0 & 0 & 0 & 0 & 0 & 0 & 0 & 0 & 0 & 0 & 0 & 0 & -\varphi & 1 - \varphi & 0 \\ 1 & 0 & 0 & 0 & 0 & 0 & 0 & 0 & 0 & 0 & 0 & 0 & 0 & 0 & 0 \\ 0 & 0 & 0 & 0 & 0 & 0 & 0 & 0 & 0 & 0 & 0 & 1 & 0 & 0 & 0 \\ 0 & 0 & 0 & 0 & 0 & 0 & 0 & 1 & 0 & 0 & 0 & 0 & 0 & 0 & 0 \\ 0 & 0 & 0 & 0 & 0 & -H2_{split} & 1 - H2_{split} & 0 & 0 & 0 & 0 & 0 & 0 & 0 & 0 \end{bmatrix} \begin{bmatrix} P_{GT} \\ P_{p1} \\ P_{p2} \\ P_{em1} \\ P_{H2} \\ P_{H2,GT} \\ P_{H2,FC} \\ P_{Bat} \\ P_k \\ P_{EL1} \\ P_{EL2} \\ P_{FC} \\ P_{s1} \\ P_{s2} \end{bmatrix} = \begin{bmatrix} 0 \\ 0 \\ 0 \\ 0 \\ 0 \\ 0 \\ 0 \\ 0 \\ 0 \\ 0 \\ \xi_{GT} \cdot P_{GT,max} \\ \xi_{FC} \cdot P_{FC,max} \\ \xi_{Bat} \cdot P_{Bat,max} \\ 0 \end{bmatrix}$$

Considering that:

$$\xi_{GT}, \xi_{FC} \in [0, 1] \quad (5.31)$$

and noting that it is reasonable to assume that the Battery cannot be charged with a power greater than that required for its highest discharge power. Consequently,

$$\xi_{Bat} \in [-1, 1] \quad (5.32)$$

The resulting propulsive input interval to describe each operating mode in $PTIS_4$ results to be highly simplified with respect to $PTIS_1$ (as it is described in Tables 5.4, 5.5, 5.6).

	OM1	OM2	OM3	OM4
ξ_{GT}	[0, 1]	[0, 1]	[0, 1]	[0, 1]
ξ_{FC}	[0, 1]	[0, 1]	[0, 1]	[0, 1]
ξ_{Bat}	[-1, 1]	[-1, 1]	[-1, 1]	[-1, 1]
φ	[0, 1]	$(+1, +\infty), P_{s1} + P_{s2} < 0$ $(-\infty, 1), P_{s1} + P_{s2} > 0$	$(+1, +\infty), P_{s1} + P_{s2} < 0$ $(-\infty, 1), P_{s1} + P_{s2} > 0$	[0, 1]

Table 5.8: Power Control Parameters for Operating Modes 1-4

	OM5	OM6	OM7
ξ_{GT}	[0, 1]	[0, 1]	[0, 1]
ξ_{FC}	[0, 1]	[0, 1]	[0, 1]
ξ_{Bat}	[-1, 1]	[-1, 1]	[-1, 1]
φ	[0, 1]	$(+1, +\infty), P_{s1} + P_{s2} < 0$ $(-\infty, 1), P_{s1} + P_{s2} > 0$	$(+1, -\infty), P_{s1} + P_{s2} < 0$ $(+\infty, 1), P_{s1} + P_{s2} > 0$

Table 5.9: Power Control Parameters for Operating Modes 5-7

While theoretically possible to combine the various propulsive input scenario arrays, it is strongly discouraged. Not all power control parameter permutations are feasible due to the risk of the matrix

	OM8	OM9	OM10
ξ_{GT}	$[0, 1]$	$[0, 1]$	$[0, 1]$
ξ_{FC}	$[0, 1]$	$[0, 1]$	$[0, 1]$
ξ_{Bat}	$[-1, 1]$	$[-1, 1]$	$[-1, 1]$
φ	$(+1, -\infty), P_{s1} + P_{s2} < 0$ $(+\infty, 1), P_{s1} + P_{s2} > 0$	$[0, 1]$	$[0, 1]$

Table 5.10: Power Control Parameters for Operating Modes 8-10

algebraic system becoming overdetermined or underdetermined. Furthermore, the propulsive input scenarios (PTIS), specifically $PTIS_1$, $PTIS_3$, and $PTIS_4$, are designed for distinct uses.

During the design phase, controlling the power ratios Φ_{Bat} and Φ_{H2} is often desirable for understanding the contributions of different energy sources, making $PTIS_1$ suitable.

$PTIS_3$ and $PTIS_4$ are applicable only after the propulsive system and its installed power are defined. $PTIS_3$ provides insight into the overall system throttle setting (as potentially requested by the pilot) and the total shaft power relative to the maximum sea-level shaft power. $PTIS_4$ is intended for use by a FADEC (Full Authority Digital Engine Control) system to manage individual component throttle settings, identifying the optimal combination for a given flight phase within a mission analysis optimizer.

6

Conceptual design synthesis for a double hybrid aircraft

The conceptual design method for a double hybrid aircraft is an expansion of traditional design methods (Roskam, Torenbeek, Raymer) that account for the additional complexity of the powertrain and multiple energy storage. The design synthesis starts from input data about

- Aircraft design parameters (wing aspect and taper ratio, ...);
- Payload mass;
- Engines type and number;
- CS/FAR category (23 or 25, depending on MTOW);
- Mission parameters and performance requirements
- Brake-specific fuel consumption;
- Power-input ratios;

The design tool shall provide as output

- Maximum power requested from each component of the powertrain along the entire mission;
- Take-off mass;
- Wing surface and span;
- Fuel mass;
- Battery mass;

In comparison to the conventional method, the sizing of hybrid systems implies that the thrust and power required from the vehicle is not solely linked to conventional engines. Instead, the power is distributed among various components, including fuel cells, electric motors, batteries, and other elements. The distribution of power is determined by the power input of the double-hybrid powertrain model. The conceptual design (Class 1) design module is represented in the flowchart below. This method is derived from De Vries dissertation [50] and extended to accommodate the coexistence of three energy sources and the powertrain components associated with hydrogen usage.

6.1. Matching Chart and Constraint Diagrams

In order to identify a feasible design space and define a design point that describes the optimal vehicle configuration in terms of maximum power, maximum take-off mass and wing surface area, a series of matching requirements have been formulated. These requirements are expressed as $T_p/W_{ref} = f(W_{ref}/S)$, where T_p represents the thrust required for a specific flight condition, W_{ref} the reference aircraft weight, which is equal to the take-off mass, and S describes the wing surface.

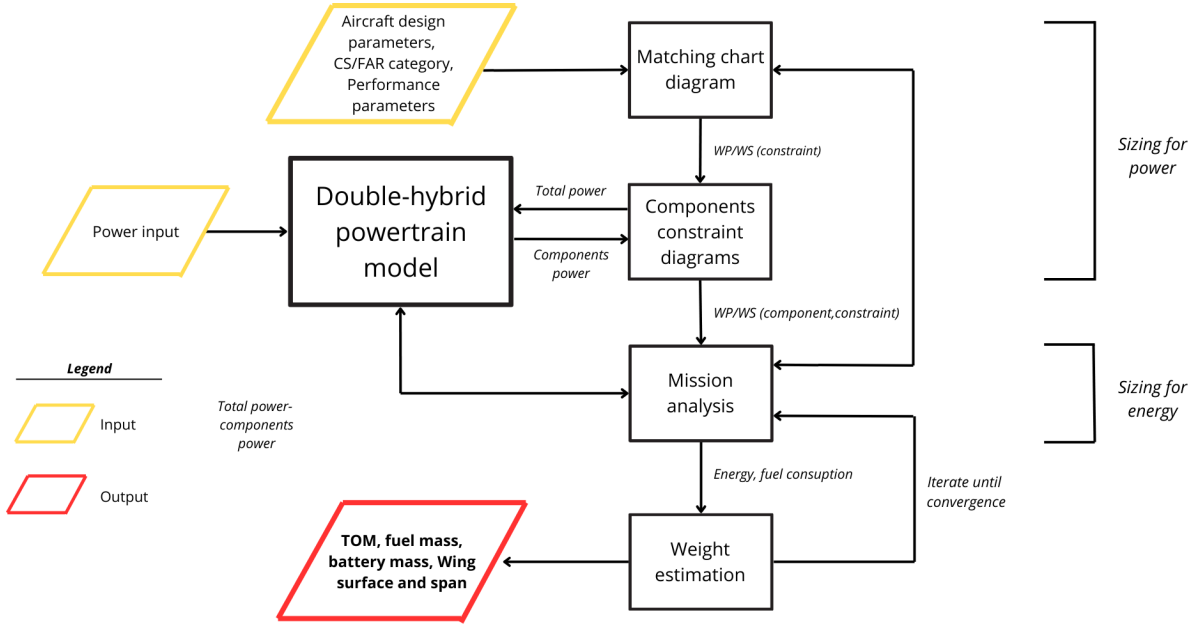


Figure 6.1: Flowchart of the conceptual design (Class 1) module. The outputs and inputs of the method are highlighted.

Those requirements represent the force equilibrium during each mission phase (*constraint cruise speed, constraint climb condition, constraint stall/landing condition*) in addition to Certification Specification requirements (*OEI balked landing constraint, OEI second-segment-climb constraint, AEO Balked landing constraint, ...*). As an example, it is reported the cruise requirement

$$\frac{T_{cruise}}{W_{ref}} = \frac{q \cdot C_D}{W_{ref}/S} + \frac{W_{ref}/S}{q \cdot \pi \lambda e} \quad (6.1)$$

where:

- $q = \frac{1}{2} \rho V_{cruise}^2$ represents the dynamic pressure;
- C_D is the drag coefficient;
- λ the wing aspect ratio;
- e express the Oswald factor.

However, in a hybrid configuration, power-loading diagrams are preferred to thrust-loading diagrams because each component of the powertrain is dimensioned in terms of power. The matching requirement expressed as a thrust loading diagram, as outlined in Equation 6.1, can be evaluated in terms of power loading as

$$\frac{W_{ref}}{P_p} = \frac{1}{V \cdot \frac{T}{W_{ref}}} \quad (6.2)$$

The propulsive system shall generate sufficient power to satisfy all the stipulated requirements. Consequently, the lowest value of W/P is to be selected from among all the requirement curves. Analogously, the wing must provide sufficient lift in all flight conditions; consequently, the lowest wing loading and highest wing surface are selected. The design space, therefore, can be identified as the area that meets all these requirements.

The Double Hybrid Powertrain model and its relative propulsive input (Φ_{Bat} , H_2 and H_2 split) are utilised to identify the components' constraints diagrams and thus the power loading for each component. First, **WP/WS design point is evaluated for a conventional aircraft**. Subsequently, for **each powertrain component, at design WS , WP is evaluated for the different constraints and the minimum is**

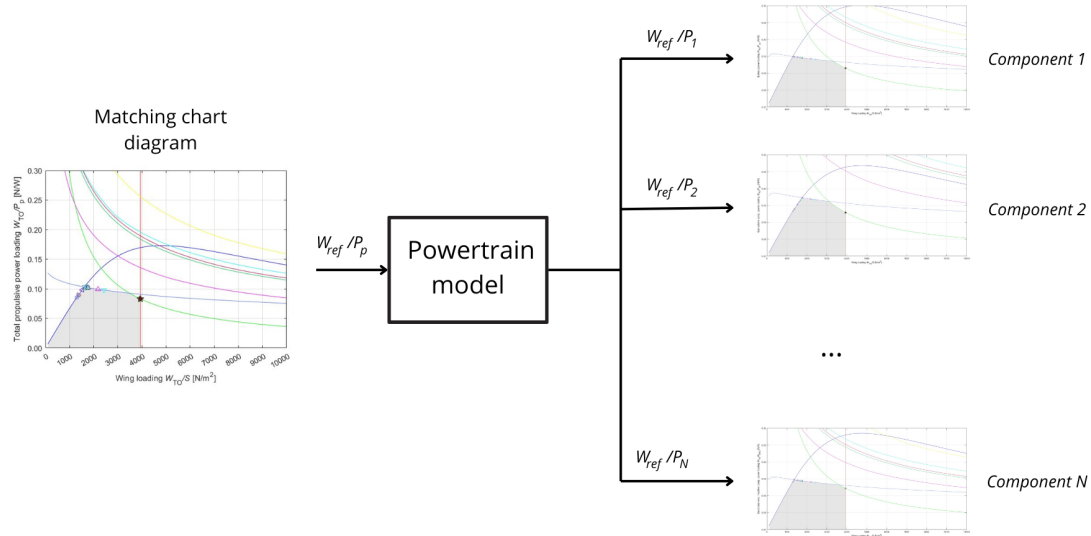


Figure 6.2: Methodology to derive the components' constraint diagram from the aircraft matching chart

chosen as the sizing constraint. Thus, each component of the powertrain can be sized in terms of the requisite power. This approach also enabled the designer to enhance the complexity of the powertrain by incorporating new components or connections between existing ones, while simultaneously assessing the power requirements of each component of the powertrain with minimal effort.

6.2. Mission Analysis

Payload-Range Diagram The payload range diagram for a dual-hybrid aircraft is an area of particular interest. In a conventional aircraft, region A represents fuel added as required to reach a specific range, with the payload capacity not exceeding the certified or physical maximum for the aircraft. Region B represents the condition where the tank is not full, and a trade-off can be made with respect to the payload mass, since the maximum take-off weight is already being reached. In Region C, the fuel tank is full, and the only way to fly further is to reduce the total weight of the aircraft, thereby reducing the payload. In contrast to conventional aircraft, Region B has different significance for a double-hybrid aircraft. It is evident that a trade-off between fuel and payload is not possible for batteries. Furthermore, the low density of hydrogen and the associated challenges in its storage necessitate that the aircraft be designed to always initiate the mission with the hydrogen tank fully loaded. Overall, the existence of the B region is contingent on the total kerosene tank capacity and its utilisation during the mission.

Mission Analysis The mission analysis has been approached through the implementation of a numerical methodology. The mission has been divided into different flight segments. For short flight segments, such as taxiing, takeoff, and landing, a fixed energy fraction, denoted by $E_{Segment}/E_{TOT}$, is adopted. These energies serve as a substitute for the fuel fraction statically estimated in traditional preliminary aircraft design methods, and they also take into account battery energy usage during these segments. For the remaining flight segments, such as climb or cruise, a specific mission analysis per segment is carried out.

The loop commences with an initial estimate of the take-off mass, the fuel type fraction, the fuel fraction, and the degree of hybridisation. It then proceeds through a series of iterations until the error falls below a pre-defined threshold limit. The error is a function of the variables involved in the convergence loop. Figure 6.4 presents a flowchart illustrating this loop.

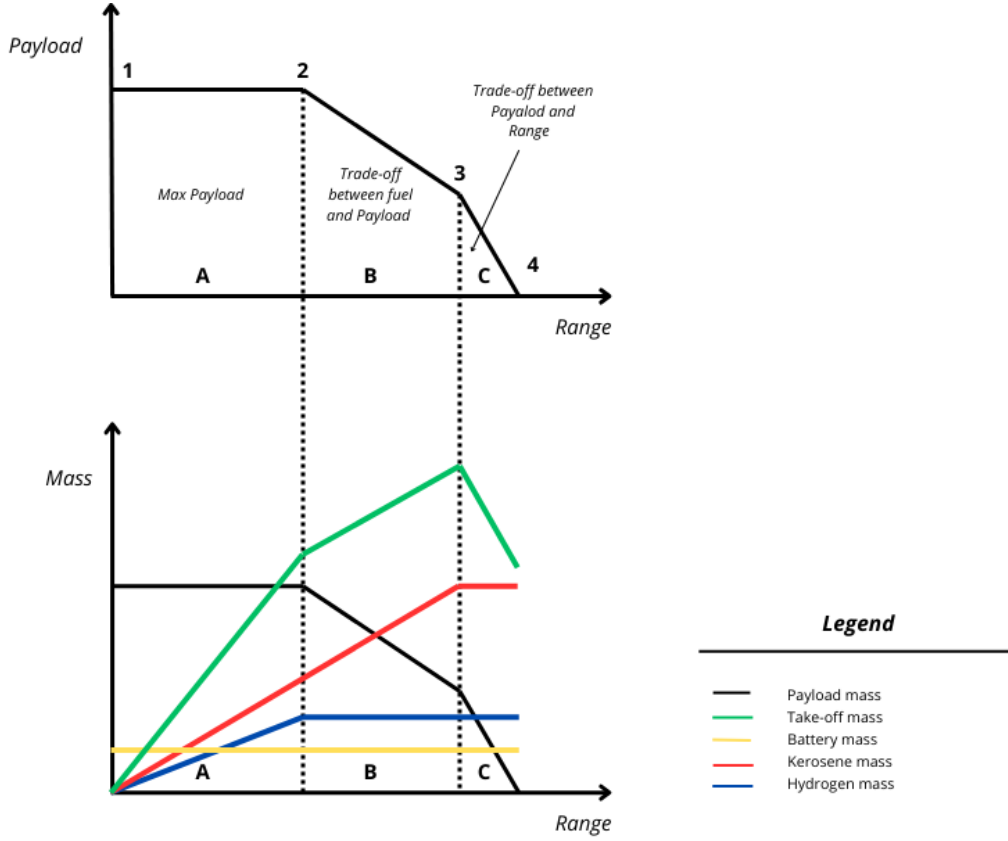


Figure 6.3: Payload-range diagram for double-hybrid aircraft

$$Err = f([TOM_1 - TOM_0] + [FTF_1 - FTF_0] + [FF_1 - FF_0] + [DOH_1 - DOH_0]) \quad (6.3)$$

In the context of flight segment mission analysis, a quasi-steady approach is employed. This approach involves the division of the flight segment into time-steps, designated as ΔT , wherein the weight, thrust, propulsive input, and aerodynamic coefficient are considered constant values. Figure 6.5 illustrates the analysis conducted for each time-step over the course of the entire mission segment analysis. In each time-step, the fuel consumption, either kerosene or hydrogen, and the battery energy consumption are evaluated as

$$e_s = P_s \cdot \Delta T \quad (6.4)$$

where s represents the energy source (hydrogen, kerosene or battery). The total energy consumption is nothing but the sum of energy calculated in each time step.

6.3. Weight Estimation

In the case of a conventional aircraft, the conceptual design mass breakdown consists of the sum of the operative empty mass, which is derived from the static data of similar aircraft, the payload mass and the fuel mass.

Torenbeek [46] suggested a formulation to determine the operative empty mass for a conventional aircraft:

$$OEM = c_1 \cdot PL + c_2 \cdot TOM + c_3 \quad (6.5)$$

where

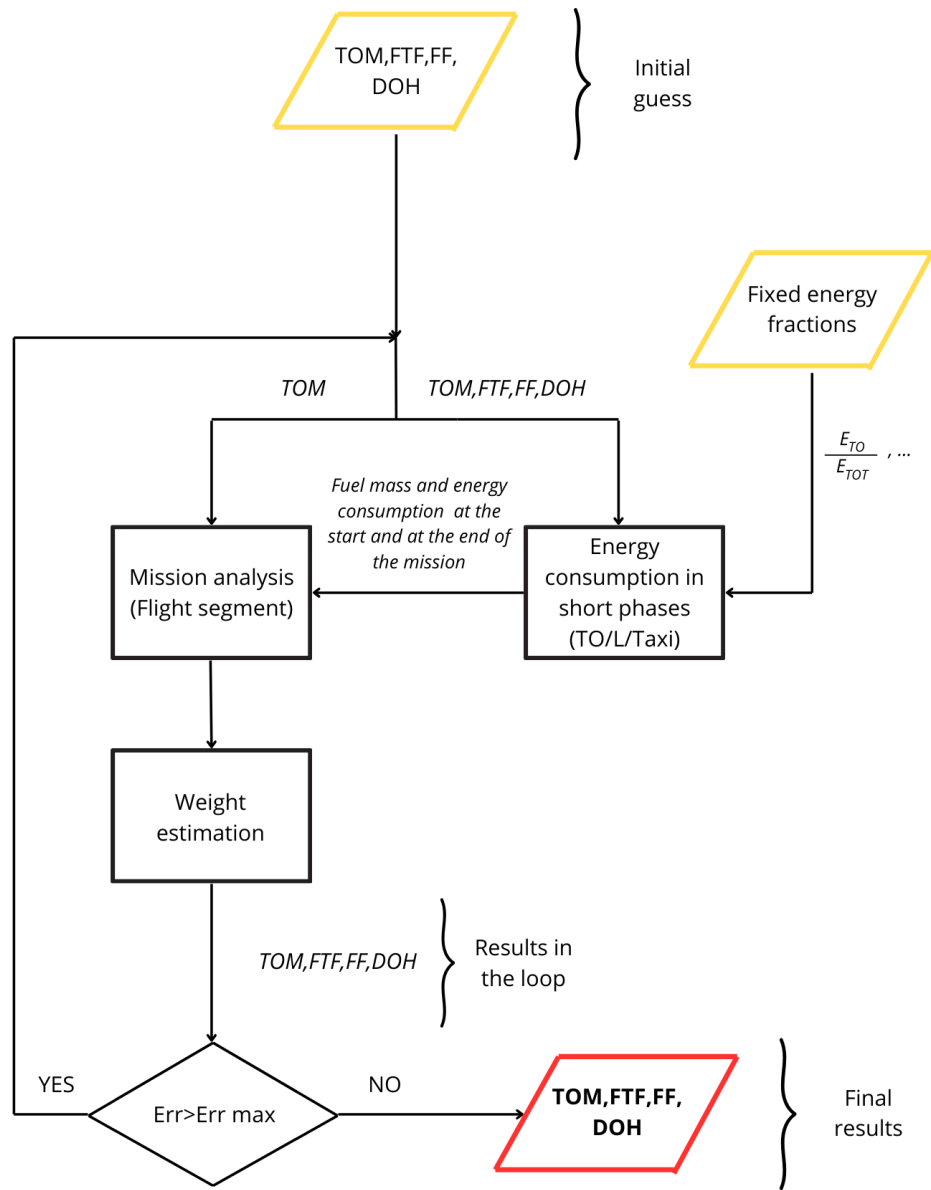


Figure 6.4: Mission Analysis and Weight estimation flow chart

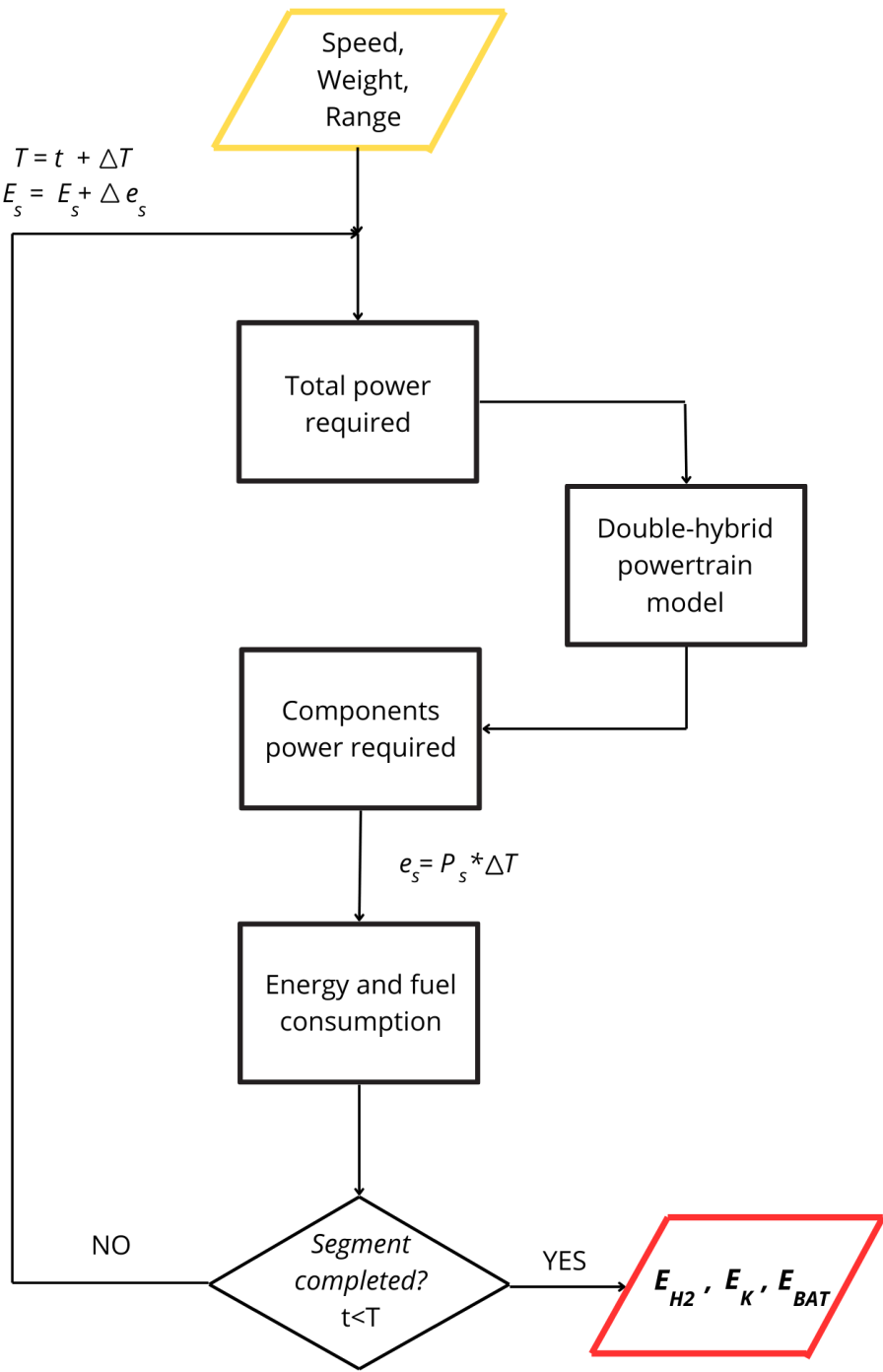


Figure 6.5: Segment mission analysis

- c_1 accounts for the overall body group weight. Items directly related to the payload mass PL and the cabin dimensions are determined. These items include the fuselage and vertical tail structures, air conditioning, pressurisation, electrical and electronic systems, passenger accommodation, cabin furnishing and equipment;
- c_2 denotes weight components that are predominantly associated with the take-off mass, TOM . This includes elements such as the wing and horizontal tail structure, the power plant, and the landing gear weight;
- Last, c_3 represents crew weight. For a given category of aircraft, this term can be assumed small in respect to TOM and independent of both the payload and the take-off mass.

In consideration of the Class-1 purpose of the weight estimation, a straightforward method to automatically derive the relative aircraft class, without defining the seat configuration, is to define a payload interval related to each class. For CS-23 aircraft, the payload limit is set by regulation to 19 passengers ($\approx 2tons$), while the payload limit for single aircraft payload is based on the maximum payload achievable the current biggest narrow-body aircraft. The parameters for Small Commuter are derived from the author.

Aircraft Class	Payload (PL)	c_1	c_2	c_3
Small Commuter (CS23)	PL < 2t	1.15	0.19	250
Single Aisle	3t < PL < 25.5t	1.25	0.20	500
Double Aisle	PL \geq 25.5t	1.50	0.20	600

Table 6.1: Coefficient for estimating OEM. Source:[46]

In the context of double hybrid aircraft, the absence of statistical data exerts a substantial influence on the conceptual design weight estimation process. While the mass of fuel and battery is calculated in the mission analysis, the OEM remains unknown.

The unity equation expressed by Torenbeek expresses the relation between that is, for double-hybrid aircraft, the sum of the mass of hydrogen, kerosene and battery.

The unity equation, which establishes a relationship between TOM , OEM , PL and energy mass EM . In the context of double-hybrid aircraft, EM corresponds to the total mass of hydrogen, kerosene and the battery.

$$TOM = OEM + PLM + EM \quad (6.6)$$

Combining Eqs 6.5 and 6.6, as derived by Wolleswinkel [53], it is possible to express the OEM for a conventional aircraft as function of PL, defined by top level requirement, and the ratio EM/TOM .

$$OEM = \left(c_1 + \frac{c_2(1 + c_1)}{1 - \frac{EM}{TOM} - c_2} \right) PL + \frac{c_2 \cdot c_3}{1 - \frac{EM}{MTOM} - c_2} + c_3 \quad (6.7)$$

This dependency of the OEM over the EM/TOM is fundamental. Indeed, even if a realistic EM/TOM for 50-100 kerosene-fuelled aircraft is $\approx 25\%$, the adoption of hydrogen and batteries as sources of energy would lead this ratio to be much lower and higher, respectively. Utilising a formulation that does not take account of this effect would result in the underestimation or overestimation of the empty mass in the case of hydrogen and battery aircraft, respectively. Figure 6.6 illustrates the influence of the EM/TOM fraction on the total mass and breakdown of a 75-passenger single-aisle aircraft.

Following the definition of the OEM as a function of EM/TOM for a conventional aircraft, a suitable approach would be to utilise the OEM, then subtract the mass of the conventional aircraft powertrain (turbofan, turboprop), and subsequently add the double-hybrid powertrain components and the resultant fuselage weight due to its stretch to accommodate the hydrogen tank. The resulting equation to calculate the take-off mass is

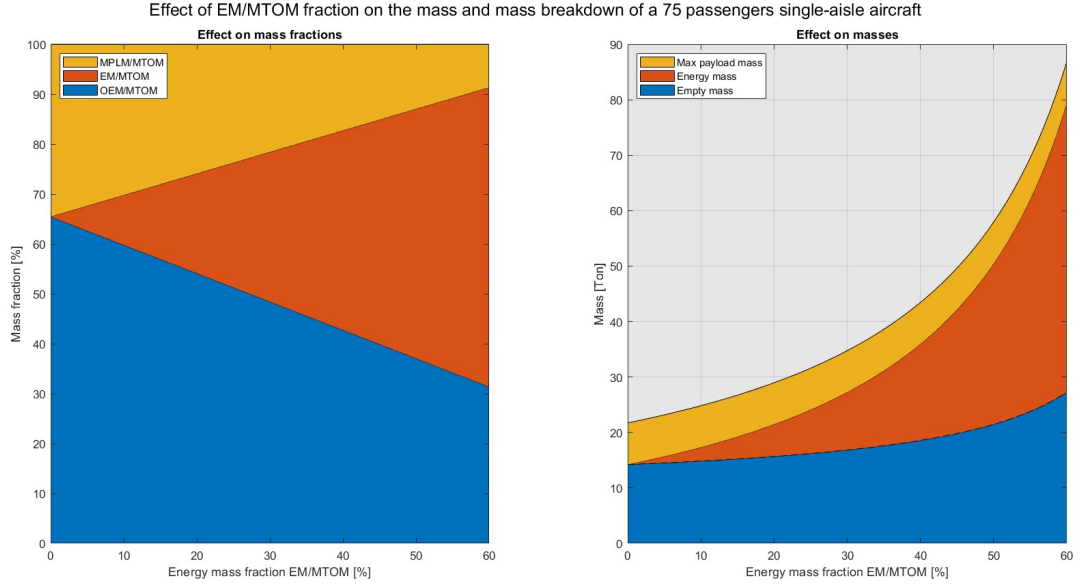


Figure 6.6: Effect of EM/TOM fraction on the mass and mass breakdown of a 75 passenger single-aisle aircraft.

$$TOM = OEM' + ELM + FC + GT + H2tank + Fus + EM + PL \quad (6.8)$$

where

- OEM' represents the operative empty mass derived from conventional aircraft (Eq.6.7) and with power plant subtracted;

$$OEM' = OEM - GT_{conv} \quad (6.9)$$

GT_{conv} represent the virtual weight of the gas turbine engine in the context of a conventional aircraft. This is calculated as a function of the approximate installed power of the gas turbine as

$$GT_{conv} = N \cdot f\left(\frac{P_{s1,inst} + P_{s2,inst}}{N} \cdot \frac{1}{\eta_{gb}}\right) \quad (6.10)$$

where $P_{s1,inst}$ and $P_{s2,inst}$ are the shaft installed power associated to the two propulsive line, N the number of engines and η_{gb} the gear box efficiency.

- ELM is the mass of electric motors, evaluated using its specific power $SP[Kg/W]$:

$$ELM = SP_{EM} \cdot P_{EM}; \quad (6.11)$$

- FC the fuel cell

$$FC = SP_{FC} \cdot P_{FC}; \quad (6.12)$$

- GT the actual mass of the gas turbine for the Double-Hybrid powertrain system. Similarly to GT_{conv} , its evaluation is derived from the actual installed power of the gas turbine:

$$GT = N \cdot f\left(\frac{P_{GT,inst}}{N}\right); \quad (6.13)$$

- $H2_{tank}$ consist in the mass associated to the hydrogen fuel tank and its fuel system. It is evaluated using the gravimetric index

$$M_{H2:fuel:system} = M_{H2} \cdot \frac{1 - GI}{GI} \quad (6.14)$$

as defined in [27].

Payload [ton]	Fuselage Diameter [m]	Fuselage Weight per Meter [kg/m]
$PL \leq 9.5$	2.8	350
$9.5 < PL \leq 25$	4.0	450
$PL > 25$	6.0	600

Table 6.2: Fuselage Diameter and Weight per Meter based on Payload

- F_{us} considers the stretching of the fuselage in order to accommodate the volume of the hydrogen tank. The tank is hypothesised to be a perfect cylinder. Its volume is increased by a factor of 1.1 to account for the venting volume and the gap between the tank wall and the fuselage skin.

$$F_{us} = F_{us_{KG/M}} \cdot L_{fus} \quad (6.15)$$

The hypothesis is that the fuselage weight per metre is dependent solely on the fuselage diameter, and furthermore, that the fuselage diameter is a function of PL.

- EM represents the energy mass (kerosene + hydrogen + battery);
- PL the payload mass.

Depending on the specific case, the battery can be sized either in terms of power (kg/W) or energy kg/J requirement. The maximum is taken as sizing mass, following the most demanding constraint. In addition, the value of the minimum state of charge of the battery is maintained through the incorporation of a 20% additional battery mass.

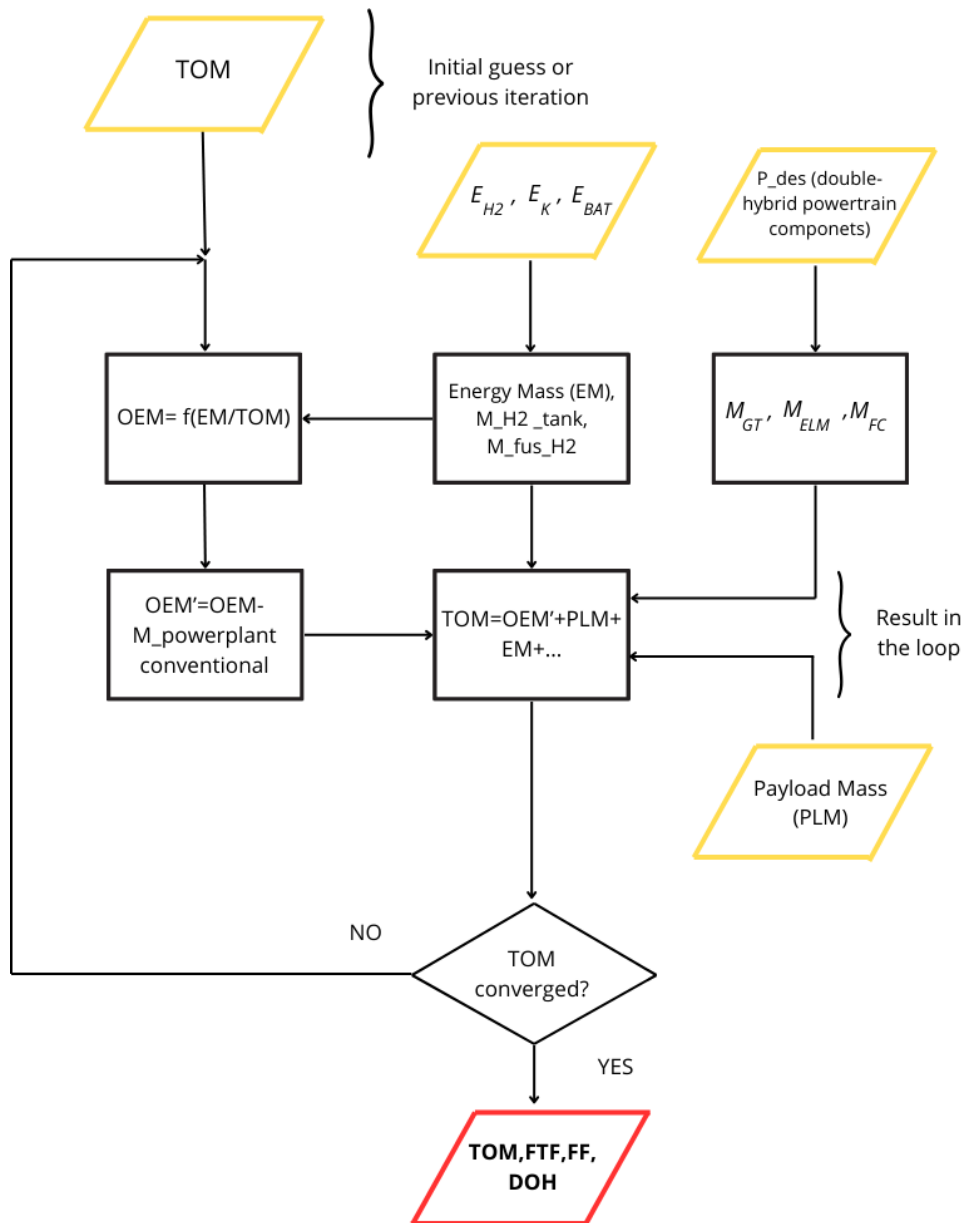


Figure 6.7: Weight estimation loop flowchart

Verification of the Double-Hybrid Conceptual Design Model

The absence of reference data regarding double-hybrid aircraft necessitated the validation to be conducted on the limit points of the design space, which encompass a conventional aircraft (fully kerosene-fuelled), a hydrogen combustion aircraft, and a more-electric aircraft where the battery supplied 20% of the energy required during cruise.

Kerosene aircraft: DO-228NG The first case proposed is a 19 passenger aircraft certified under CS-23 Regulation. To compare the double-hybrid with existing design synthesis conceptual design tool, respectively developed by Orefice [38] and De Vries , is chosen an aircraft already taken into account by the two authors, namely the Dornier DO-228NG. The high level requirements are shown in the following table

The initial case under consideration is that of a 19-passenger aircraft certified under CS-23 Regulation. In order to facilitate a comparison between the double-hybrid and the existing design synthesis conceptual design tool, respectively developed by Orefice [38] and De Vries [20], an aircraft that has already been taken into account by the two authors is selected: namely the Dornier DO-228NG. The high-level requirements are shown in the following table.

	Value	Unit
Number of passengers	19	-
Aspect ratio	9	-
Design range	396	km
Landing field length	720	m
Take-off field length	793	m
Cruise speed	115	m/s
Cruise altitude	3000	m
Alternate range	270	km
Fuel reserve	5	%
Holding	30	min

Table 7.1: TLAR of DO-228NG

The outcomes demonstrate a strong correlation between the Double-Hybrid model and the actual aircraft mass. The maximum take-off mass error is notably lower than the errors associated with the other two design methods previously referenced. The fuel-mass results are marginally higher than the reference, however, it is noteworthy that the burned fuel is significantly influenced by the maximum lift-to-drag ratio and the brake specific fuel consumption, whose values are not reported for the other two methods. Consequently, the results are considered to be reasonably accurate.

	HEAD[38]		Method A[20]		Double-Hybrid Model		DO-228NG
	Error (%)		Error (%)		Error (%)		
MTOM [kg]	6171	-3.6%	6641	3.8%	6220	-2.8%	6400
Fuel Mass [kg]	547	1.3%	615	13.9%	570	5.6%	540
OEM [kg]	3663	-6.2%	3866	-1.0%	3690	-5.5%	3904
BSFC (g/kWh)					394		
L/D max					14		

Table 7.2: Comparison among the three design methods

Hydrogen Aircraft: LH2 Turboprop The absence of reference data concerning existing flying prototypes of liquid hydrogen aircraft is a significant limitation. Consequently, comparisons can only be made with other design models. For the purposes of this case study, the Class-2 results developed by Mukhopadhaya [33] are taken as the reference point. The high-level requirements for the aircraft are presented below and are consistent with the high-level requirements for the ATR72, which is used as a conventional reference aircraft.

	Value	Unit
Range	1420	km
Passenger	70	-
Mach Number	0.45	-
Aspect Ratio	15	-
Take-off Distance	1400	m
Gravimetrix Index (GI)	0.35	-
Altitude	6100	m

Table 7.3: TLAR for hydrogen combustion aircraft

	Double-Hybrid Model	Mukhopadhaya [33]	Diff. (%)
OEM [ton]	16.95	17.80	-5.01
Fuel Mass [ton]	1.07	1.19	-11.21
MTOM [ton]	24.54	25.50	-3.91
BSFC [g/kWh]			386
L/D max			18.5

Table 7.4: Comparison among the two design methods for hydrogen combustion aircraft

As was observed in the preceding case study, the most significant disparity between the two design methodologies pertained to the burned fuel, which was found to be considerably influenced by the BSFC and L/D max. The developed Class-1 method was found to be accurate, with a -3.91% difference compared to the reference MTOM. This finding aligns with the results reported in the study by Mukhopadhaya [33].

More electric aircraft The reference aircraft in this case is a Class-2 aircraft developed as part of the CHYLA project [3]. This aircraft is characterised by a single-aisle configuration and a turboprop engine, with a payload capacity of 7.5ton , a battery power ratio of $\Phi_{Bat} = 0.16$ and a total range of 926km (including loiter and diversion ranges).

	Value	Unit
Payload	7500	kg
Range	463	km
Mach Number	0.4	-
Aspect Ratio	12	-
Altitude	7000	m
Alternate Range	185	km
Loiter Time	45	min
Alternate Mach	0.4	-
Alternate Altitude	3500	m
Take-off Distance	1300	m
Landing Distance	1200	m

Table 7.5: TLAR of battery-electric aircraft

	Double-Hybrid Model	CHYLA [3]	Diff. (%)
MTOW [t]	34.95	36.30	-3.72
L/D max	19.76		
BSFC [g/kWh]	294		

Table 7.6: Comparison among the two design methods for battery-electric aircraft

Emission Estimation Metodology

A crucial point in the design synthesis of a next generation aircraft consists in a preliminary estimation of the relative environmental impact. In particular, for a Double-Hybrid aircraft, it is necessary to implement a model capable to calculate the chemical emissions throughout the cruise segment for three distinct sources of energy and their utilisation. Specifically, the model should encompass:

- Kerosene combustion;
- Hydrogen combustion;
- Hydrogen for fuel cell reaction;
- Battery.

The ensuing sections will address the direct emission estimation of kerosene and hydrogen. It is important to note that the indirect emissions from batteries are not included in these estimations.

8.1. Kerosene Combustion

The combustion of kerosene in air produces various chemical molecules, categorized into two groups: those proportional and those non-proportional to fuel consumption. The proportional group, directly related to fuel consumption during different flight phases, includes carbon dioxide (CO_2), water vapor (H_2O), and sulfur oxides (SO_x).

Non-proportional emissions include nitric oxides (NO_x), carbon monoxide (CO), and hydrocarbons (HC). Nitric oxides (NO_x) are formed when atmospheric nitrogen (N_2) enters the high-temperature combustion chamber, increasing with temperature and pressure due to thermal reaction processes in the primary combustion zone. Carbon monoxide (CO) and hydrocarbons (HC) result from incomplete combustion. Unlike NO_x , these emissions are inversely proportional to combustion efficiency. Since combustion efficiency correlates with thrust (at sea-level static conditions) and thrust correlates with fuel flow, the emission indices (EI) for CO and HC decrease with increasing fuel flow.

The emission index (EI) is the mass of emissions produced per unit mass of fuel burned, measured in grams of emissions per kilogram of fuel. Table 8.1 shows the EI for proportional chemical emissions, constant throughout the mission profile due to stoichiometric combustion.

Emission	EI (g/kg)
CO_2	3160
H_2O	1240
SO_x	0.06

Table 8.1: Emission Indices for Proportional Chemical Emissions

The EI at sea level conditions for the landing, climb-out, approach, and take-off (LTO) cycle—each with a specific engine thrust setting and mode duration—for uninstalled turbofan and turbojet engines are available in the ICAO Emissions Data Bank [8].

	Take-Off	Climb-Out	Approach	Idle
Thrust Setting	100%	85%	30%	7%
Mode Duration (min)	0.7	2.2	4	22

Table 8.2: ICAO Standard for LTO Cycle Operating Mode Thrust Setting and Duration

8.1.1. Boeing Fuel Flow Method 2

This chapter presents the Boeing Fuel Flow Method 2 [17], a semi-empirical approach that correlates the EI measured at sea level in the LTO cycle with the EI in any condition as a function of engine fuel flow, ambient conditions, and Mach number.

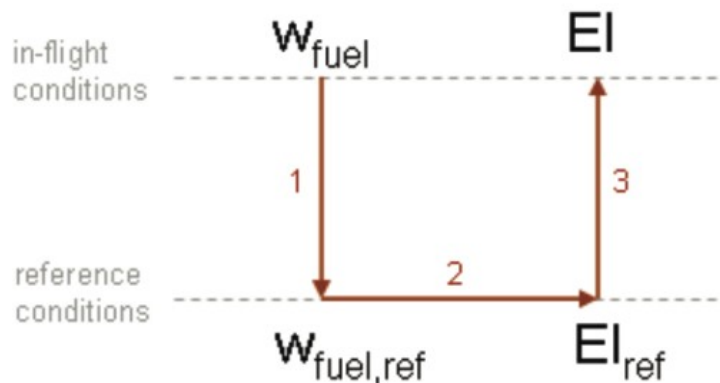


Figure 8.1: Graphical representation of the Boeing Fuel Flow Method 2 steps to correlate in flight EI to reference conditions EI

It consists of three steps:

1. The fuel flow obtained from mission analysis, W_f , is adjusted to a fuel flow factor, W_{ff} , at reference conditions:

$$W_{ff} = \frac{W_f \theta^{3.8} e^{(0.2M^2)}}{\delta} \quad (8.1)$$

where:

$$\theta = T/T_{SL}$$

$$\delta = P/P_{SL}$$

T and P are the ambient temperature and pressure, respectively, and T_{SL} and P_{SL} are the sea level temperature and pressure.

2. Boeing proposes a correction factor, r , to be applied to the fuel flow data from the ICAO Database. This adjustment accounts for engine installation effects, including bleed air usage.

	Take-Off	Climb-Out	Approach	Idle
Correction Factor (r)	1.010	1.013	1.020	1.100

Table 8.3: Correction Factor Applied to Thrust Setting (BFFM2)

A relationship exists between the fuel flow factor, W_{ff} , and the emission indices measured at reference conditions for non-proportional chemical species:

$$EI_{ref} = f(W_{ff}) \quad (8.2)$$

3. Finally, the reference EIs are adjusted to flight conditions:

$$EICO = EICO_{ref} \frac{\theta^{3.3}}{\delta^{1.02}} \quad (8.3)$$

$$EIHC = EIHC_{ref} \frac{\theta^{3.3}}{\delta^{1.02}} \quad (8.4)$$

$$EINO_x = EINO_{x,ref} \sqrt{\frac{\delta^{1.02}}{\theta^{3.3}}} e^H \quad (8.5)$$

where:

$$\begin{aligned} \beta = & 7.90298(1 - \tau) + 3.00571 + 5.02808 \log_{10}(\tau) \\ & + (1.3816 \times 10^{-7}) \left(1 - 10^{11.344(1 - \frac{1}{\tau})}\right) \\ & + 8.1328 \times 10^{-3} \left(10^{3.49149(1 - \tau)} - 1\right); \end{aligned}$$

$$P_v = 0.014504 \cdot 10^\beta$$

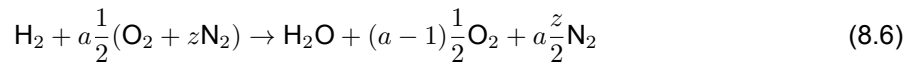
$$\omega = \frac{(0.62197058 \cdot \phi \cdot P_v)}{(P_{amb} - \phi \cdot P_v)}$$

$$H = -19(\omega - 0.00634)$$

$0.6 < P_v < 0.75$, is the relative vapour pressure, depending on the altitude.

8.1.2. Hydrogen Emissions

Hydrogen combustion emissions differ from kerosene combustion emissions, particularly due to hydrogen's **higher flame temperatures and lower heating values** (Chapter 4.2). As reported in Ref. [42], carbon species are not involved; therefore, CO₂, CO, HC, and soot are eliminated. The absence of aromatics also eliminates SO_x formation.



Furthermore, burning one kilogram of hydrogen produces more H₂O and NO_x than burning one kilogram of kerosene.

In fuel cells, emission calculation is simpler. The only product in stoichiometric reactions is water (Equation 4.11).

The emission indices for water (the unique proportional emission species) from fuel cell reactions and hydrogen combustion are:

	Hydrogen Combustion	Fuel Cell
EI H ₂ O (g/kg)	9000	18000

Table 8.4: Emission Indices for Water

For hydrogen combustion NO_x emissions, Funke [21] suggests a relative EI approximately +30% higher than kerosene. For this preliminary estimation, the EI NO_x derived using BFFM2 for kerosene is multiplied by 1.3:

$$EI \text{ NO}_x(\text{H}_2) = 1.3 \cdot EI \text{ NO}_x(\text{kerosene, BFFM2}) \quad (8.7)$$

8.2. Emissions for Turboprop Engine

The ICAO Emissions Databank does not report data regarding turboprop and turboshaft engines. Consequently, an extrapolation for this particular type of engine is necessary. The results reported herein are taken from Filippone et al. [19] and refer to the PW150A engine installed on the Bombardier Q400. It should be noted that some key points differ from those in the ICAO emission evaluation.

- The data under consideration refers to a set of full flights from gate to gate. It should be noted that this includes both low and high power demands for the engine.
- Those data are effected by atmospheric effects and engine intake distortion (installation and propeller's induced flow);
- Saying that N_1 is the percent gas generator speed, at $N_1 = 95\%$ there is a sharp increase in fuel flow, which is accompanied by an increase in shaft torque. For example, the gas generator turbine never reaches the 100% speed required by the ICAO standard settings.
- Lastly, the fuel flow drops to zero at engine speeds of the order of 25 – 30%. Therefore, idle conditions can be interpreted as $N_1\% = 25$, in contrast to the prescribed ICAO value.

In addition to the previous assumptions, it's assumed that the EI NO_x as a function of throttle setting remains constant independently if the gas turbine engine is upscaled or down scaled in respect to the PW150A.

Fuel flow for PW150A is expressed by the function

$$W_f = e^{(4.459 \cdot 10^{-2} \cdot N_1 - 4.098)} [kg/s] \quad (8.8)$$

and the relative scaled fuel flow by means of installed gas turbine power

$$W_{f_{scaled}} = W_f \cdot \frac{P_{GT,inst}}{P_{GT,PW150A}} \quad (8.9)$$

	Take-Off	Climb-Out	Approach	Idle
N_1 [%]	100	85	30	20

Table 8.5: Throttle setting definition in LTO Cycle for Turboprop Engine

The resulting predicted emissions are reported in the table below.

	NO_x	CO	HC
Takeoff	16.089	0.588	0.093
Climbout	12.636	0.669	0.109
Approach	7.003	6.001	0.328
Idle	3.305	32.703	4.162

Table 8.6: Predicted emission indices for the PW150A. All data are [g/kg].

and the relative interpolated function for EI NO_x

$$EI \text{ NO}_x = 3.165 \cdot \log(W_{f_{scaled}}) + 14.4373 \quad (8.10)$$

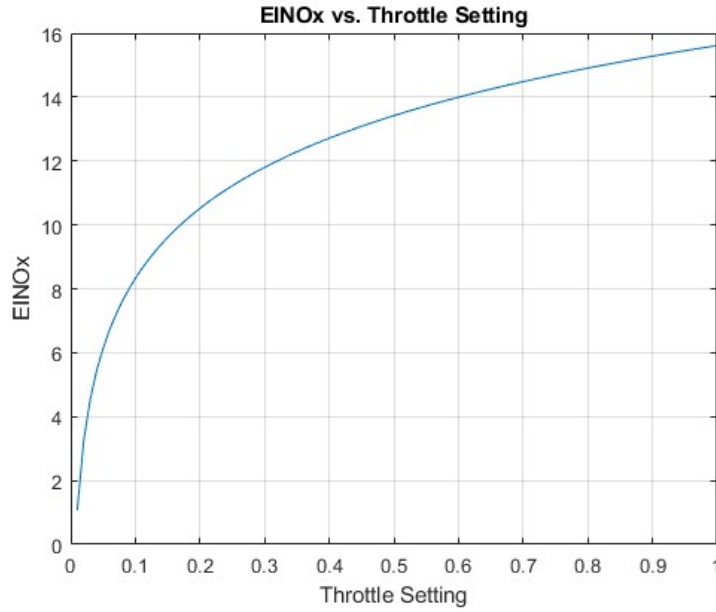


Figure 8.2: $EINO_x$ depending on throttle setting for PW150A engine

8.3. Cumulative Emissions Estimation

As hydrogen and kerosene are characterised by different emissions, it is interesting to evaluate the preliminary predicted cumulative emissions. Kerosene is characterised by the emission of carbon dioxide and water, while hydrogen is characterised by a zero CO_2 emission but a higher emission of water. These species have different environmental impacts. The cumulative emissions are evaluated in terms of effective radiative forcing ($ERF[mW/m^2]$). ERF accounts for the alteration in the net, downward minus upward, radiative flux due to a modification in an external driver of climate change.

The subsequent simplified formulation does not take into account either flying altitude or atmospheric humidity variation across different locations. Due to this, the values reported in the following table and extracted by, have to be considered only as estimation of the order of magnitude environmental impact of the diverse species.

The subsequent simplified formulation does not take into account either flying altitude or atmospheric humidity variation across different locations. Consequently, the values presented in the ensuing table and derived by Filippone [19] should be regarded as estimation of the environmental impact magnitude of the various species.

	Specific ERF	Units
CO_2	1.4×10^{-5}	$mW/m^2/ton$
NO_x	5.5×10^{-6}	$mW/m^2/ton$
H_2O	5.20×10^{-3}	$mW/m^2/ton$
Contrail cirrus	1.82×10^{-9}	$mW/m^2/km$

Table 8.7: Effective Radiative Forcing (ERF) for most relevant aviation emissions chemical species

Finally, it is possible to calculate the cumulative ERF and thus the total environmental impact.

$$ERF = \sum_i \text{Specific ERF}_i \cdot M_i + \text{Specific ERF}_{\text{contrails}} \cdot R \quad (8.11)$$

where index i represents the different chemical species (CO_2 , NO_x , H_2O), M_i their respective mass, and R the aircraft range.

Double-Hybrid Sensitivity Analysis for a Regional Aircraft Application

Following the definition of the model of the Double-Hybrid Powertrain, its parameters and limits, and the integration of the powertrain into the conceptual design process, the aircraft design synthesis can be performed. Initially, the power ratio design space should be considered. The design space is characterised by the possibility of burning either or both kerosene and hydrogen, and using the least either or both for combustion and fuel cell. Conventional kerosene aircraft is characterised in the power ratio design space by a single point, corresponding to the gas turbine entirely fed by kerosene. The single-hybrid configuration can be seen as one vector with 1 degree of freedom (its length), corresponding to 1 DOH. Conversely, the configuration of a double-hybrid powertrain is represented by a three-dimensional vector, with spacing across power ratio variables (Φ_{Bat} , Φ_{H2} , $H2_{split}$).

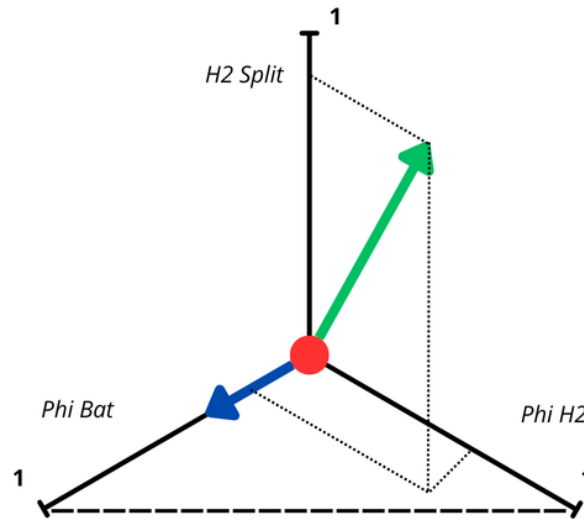


Figure 9.1: Graphical representation of power ratio design space for a Double-Hybrid Powertrain

A key question to be addressed within the scope of this thesis is that of the effect of power ratio vector spacing across the design space on some relevant performance indicators. The specific performance indicators that are of particular importance in this regard are as follows: TOM, OEM, wing span, energy consumption and environmental impact. The ensuing analysis is centred on a case study of a regional aircraft, featuring a parallel powertrain architecture ¹ and a conventional twin-engine configura-

¹Power control parameters spanning across their space enables to analyse each of the five parallel architecture (Fig. 5.2) configuration since each configuration is characterised by a different combination of parameters Φ_{Bat} , Φ_{H2} and $H2_{split}$

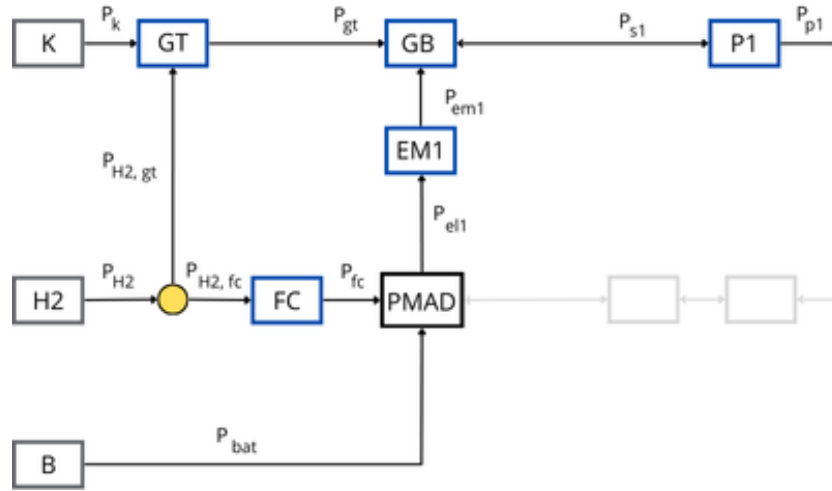


Figure 9.2: Parallel powertrain configuration employed in this study

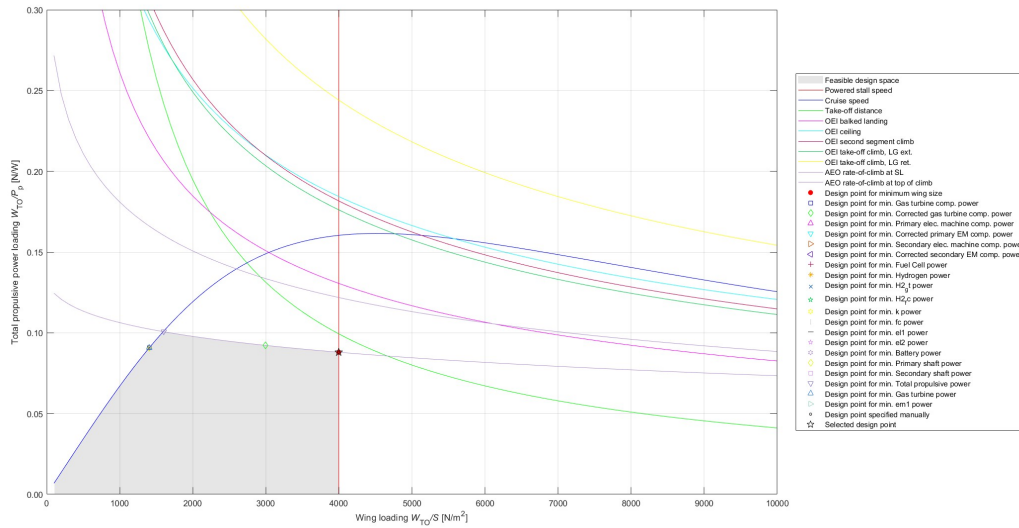


Figure 9.3: Total propulsive power constraint diagram

ration. Power control parameters $\Phi_{Bat}, \Phi_{H2}, H2_{Split}$ were varied **a priori** from 0 to 1 in increments of 0.1.

Subsequent sections present the high-level requirements that guided the sizing of the aircraft, complemented by the CS25 specification. As the requirements remain constant, each aircraft derived from this analysis is characterised by the same PW and WS ratios. In terms of mission analysis, the focus is on the most energy-demanding and environmentally impactful segment: the cruise segment.

9.1. TLAR and Powertrain Input Parameters

The high-level requirements employed for the present study, as presented in Table 9.1, are derived from the high-level requirement for a classic conventional aircraft, the ATR72. It is important to note that no requirements are related to the loiter and diversion segment. The constraint diagram for the overall propulsive system is presented below. It can be observed that the design point varies with respect to the design points for individual components minimum power.

With regard to powertrain components efficiencies (see Tab. 9.2), the technology available in 2025 was

considered. It is notably that hydrogen combustion was considered more efficient rather than kerosene combustion, following . is important to note that hydrogen combustion was considered to be 3% more efficient than kerosene combustion, as referenced in[47]. A sensitivity analysis of the efficiency of individual components is scheduled to be conducted in the subsequent chapter.

Parameter	Value	Component	Symbol	Efficiency
Payload [kg]	7500	Gas Turbine (Kerosene)	$\eta_{GT,k}$	0.282
Range [km]	926	Gas Turbine (Hydrogen)	η_{GT,H_2}	0.290
Mach Number	0.4	Gearbox	η_{GB}	0.95
Aspect Ratio	12	Electric motor	η_{em1}	0.95
Cruise Altitude [m]	7000	PMAD	η_{PMAD}	1.00
Take-off Distance [m]	1400	H ₂ Storage and Distribution	$\eta_{H_2 SD}$	0.95
Landing Distance [m]	1200	Fuel Cell	η_{FC}	0.50
Time to Climb [min]	17.5	Battery specific energy	SE_{bat}	340 Wh/kg
Climb Altitude [m]	5400	Hydrogen fuel system	GI_{H_2}	0.35
L/D max	19.76			

Table 9.1: TLAR of Case Study Aircraft

Table 9.2: Parallel Powertrain Efficiency Parameters

9.2. Power Ratio Design Space Analysis

For this analysis, since the power control ratios remain fixed along the entire flight mission, these coefficients also represent the cumulative energy splitting (i.e., Φ_{Bat} would account for the overall battery energy ratio over the total energy) and partially overlap the definition of the energy degree of hybridization. In fact,

$$\Phi_{Bat} = \frac{P_{Bat}}{P_{Bat} + P_{H_2} + P_k} = \frac{E_{Bat}}{E_{Bat} + E_{Fuel}} = EDOH_{Fuel} \quad (9.1)$$

Below are the KPI results plotted on Φ_{Bat} , Φ_{H_2} graphs, depending on the H_{2split} parameter. The colors represent the indicator itself, e.g., TOM, OEM, etc.

Take-Off Mass In the absence of a fuel cell ($H_{2split} = 0$), TOM is solely dependent on the battery power ratio Φ_{Bat} . This dependence arises from the significantly lower specific energy of batteries compared to both hydrogen and kerosene:

$$SE_{bat} \ll SE_k < SE_{H_2} \quad (9.2)$$

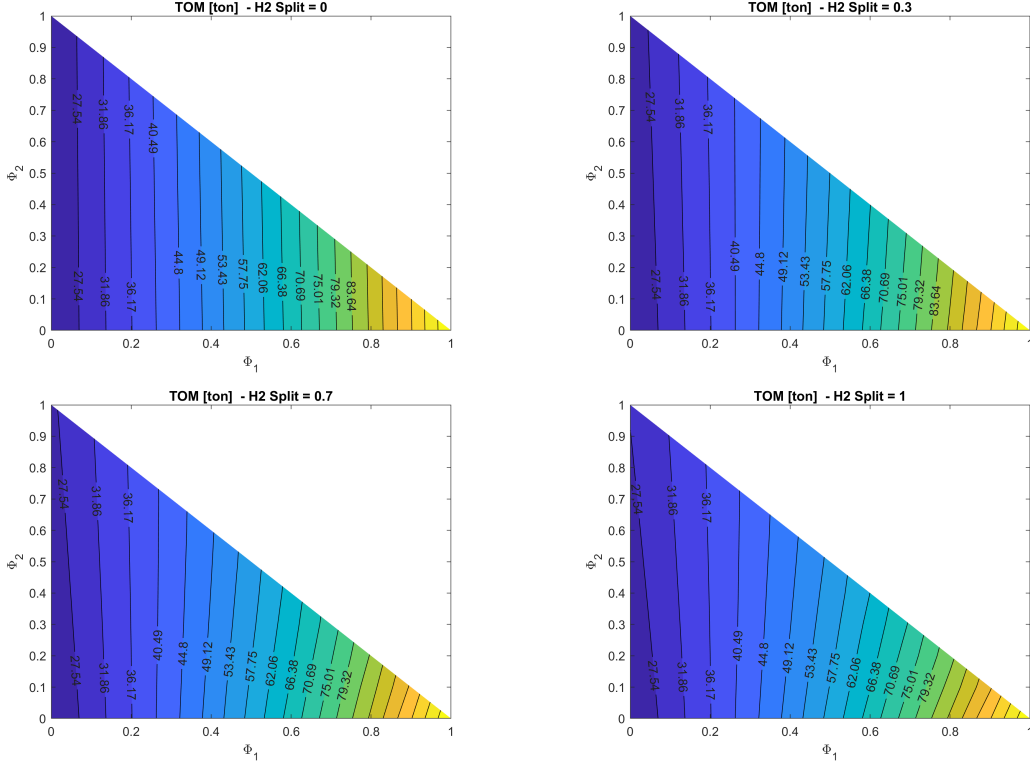
Notably, a fully battery-powered aircraft weighs approximately four times more than a conventional kerosene-powered aircraft. As illustrated in Fig. 9.4, the fuel DOH has a negligible influence in this scenario. The added weight of the hydrogen fuel system and fuselage stretch is offset by the lighter fuel mass, a consequence of hydrogen's higher specific energy compared to kerosene.

Conversely, increasing the proportion of hydrogen directed to the fuel cell leads to a greater dependence on Φ_{H_2} . This trend is evident when considering the lower and upper ranges of Φ_{Bat} . For $\Phi_{Bat} \approx 0 \div 0.3$, increasing Φ_{H_2} results in a corresponding increase in TOM. This is attributable to the combined weight of the fuel cell and the electric motor, due to their differing specific powers:

$$SP_{GT} > SP_{FC} + SP_{em} \quad (9.3)$$

Iso-TOM lines slope change is mitigated by the higher efficiency of the group fuel cell and electric motor in comparison to the gas turbine. This results in a lower demand for fuel. However, within the range $0.7 < \Phi_{Bat} < 1.0$, as the gas turbine engine's contribution diminishes, increasing Φ_{H_2} reduces the battery requirement and consequently the overall weight. This reduction is due to the difference in specific energy between batteries and hydrogen.

Take Off Mass

Figure 9.4: TOM results for varying H_2 split fractions

Wing Span As the WS requirements remains fixed across the power ratio design space, and the same way for aspect and taper ratio, wing span trend (Fig. 9.5) can be perfectly overlapped to TOM. It is interesting to note that totally combustion aircraft (either kerosene or hydrogen) is characterised by a half of the wing span ($\approx 26m$) respect to full battery aircraft ($\approx 55m$).

Zero Fuel Mass An analysis of the Zero Fuel Mass (ZFM) (Fig. 9.6) reiterates the trends observed previously for the TOM. In the full hydrogen combustion case ($H_{2split} = 0$), the weight of the hydrogen fuel system, while not negligible, has a relatively small impact on the overall weight. This is reflected in the slightly negative slope of the iso-ZFM lines. Conversely, when hydrogen is completely directed to the fuel cell ($H_{2split} = 1$), the combined weight of the fuel cell and electric motor becomes significant. As discussed earlier, a weight reduction is expected with increasing Φ_{H_2} for battery power ratios within the range $0.7 < \Phi_{Bat} < 1.0$, due to the decreased battery requirement.

Energy Consumption Regarding total energy consumption (Fig. 9.8), the results are strongly influenced by the overall powertrain efficiency, which is clearly dependent on the efficiency and usage of individual components.

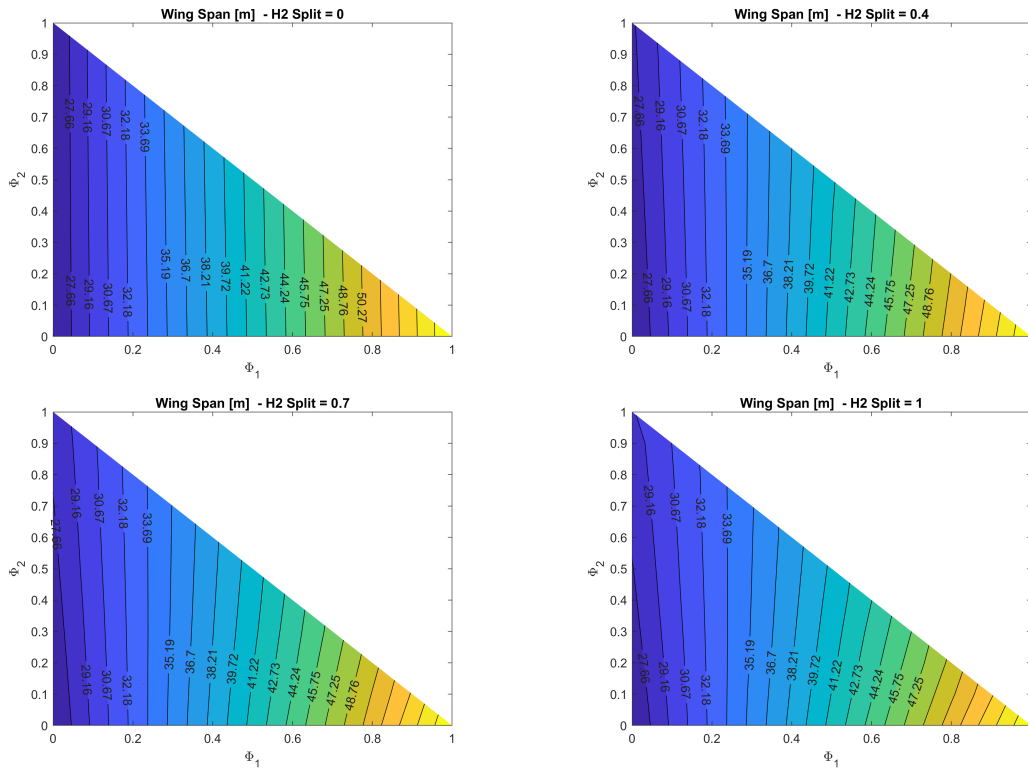
For $\Phi_{Bat} \approx 0 \div 0.3$, hydrogen combustion results in a slightly higher energy consumption (+3%) compared to the conventional configuration. Despite a more efficient combustion process and comparable TOM, hydrogen combustion aircraft exhibit slightly higher energy demands due to the increased ZFM and liquid hydrogen boil-off losses, $\eta_{H_2 SD}$.

Battery-electric aircraft, although exhibiting a higher overall powertrain efficiency², consume 1.4 times more energy than conventional kerosene aircraft, despite a four-times higher TOM.

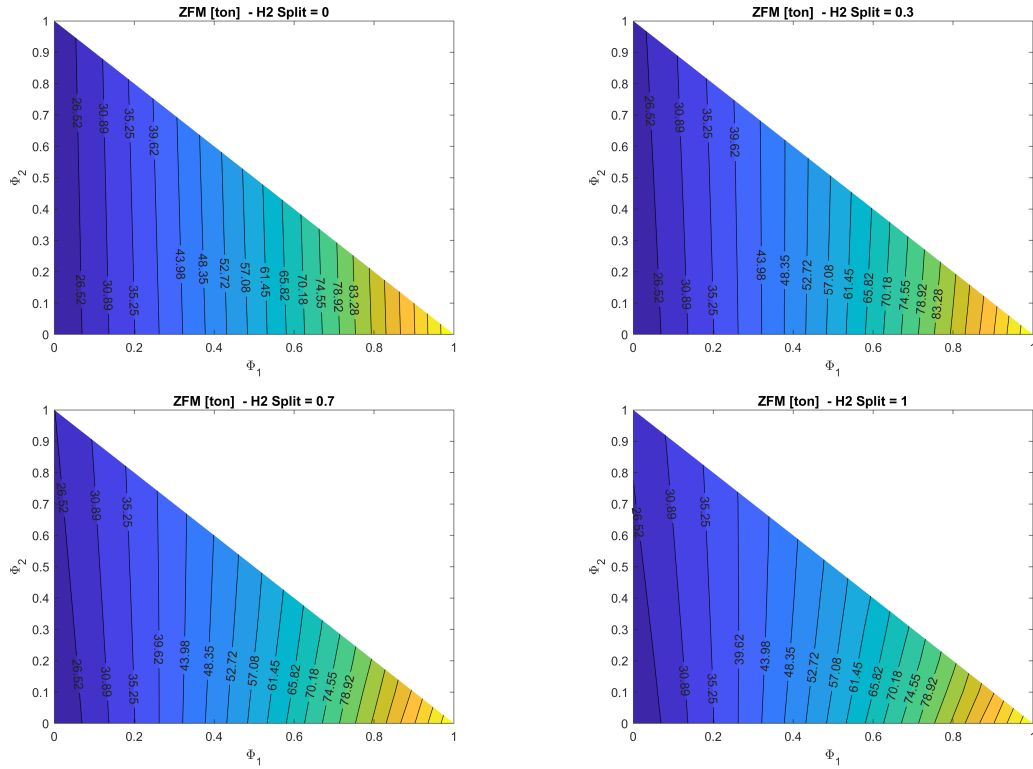
The effect of the ratio η_{PT}/TOM on total energy consumption across the power ratio design space is noteworthy (Fig. 9.7). Surprisingly, plotting the total energy consumption normalised over conventional

²Referring to Fig. 5.2, overall powertrain efficiency is defined as $\eta_{PT} = \frac{P_{s1}}{P_k + P_{H_2} + P_{bat}}$.

Wing Span

Figure 9.5: Wing span for varying H_2 split fractions

Zero Fuel Mass

Figure 9.6: ZFM results for varying H_2 split fractions

kerosene fuelled aircraft E_{NORM} , the resulting relationship is practically bijective, regardless of how that efficiency is achieved. The resulting interpolating function is:

$$E_{NORM} = a \cdot \log \left(b \cdot \frac{\eta_{PT}}{TOM} \right) \quad (9.4)$$

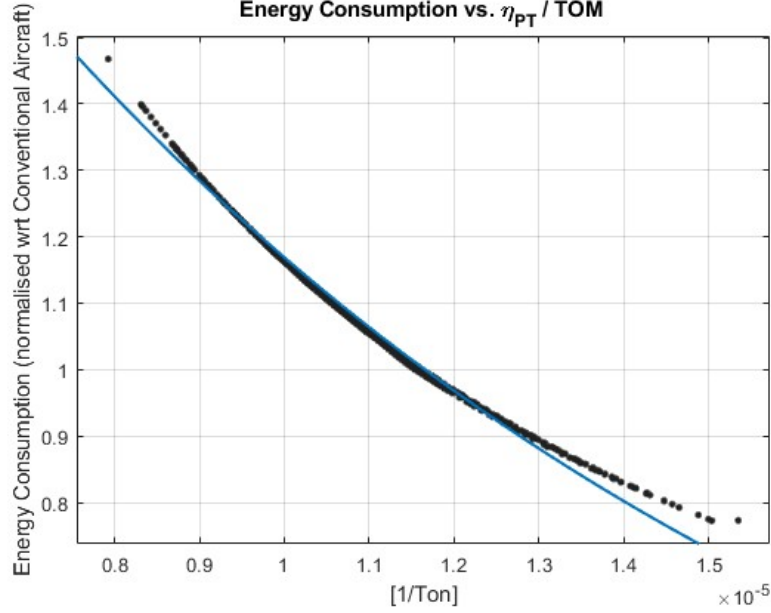


Figure 9.7: Effect of η_{PT}/TOM on total energy consumption

Conversely, as the fuel cell's contribution to the powertrain increases, the iso-total energy lines acquire a positive slope. This phenomenon can be attributed to the varying efficiencies associated with the fuel cell and the gas turbine.. In fact,

$$\eta_{FC} > \eta_{GT}$$

Notably, a region of minimum energy consumption can be identified for $H2_{split} = 1$, $\Phi_{Bat} \approx 0 \div 0.2$, and $\Phi_{Bat} \approx 0.7 \div 1$. This suggests that a fully electric aircraft powered solely by the fuel cell, or by a fuel cell combined with a small battery contribution, or even a combination of fuel cell and kerosene combustion, could reduce the total energy consumption.

Energy Mass Fraction As hypothesized previously, EMF exhibited in Fig. 9.9 varies between approximately 0.01 and 0.04 for aircraft configurations without batteries, and reaches approximately 0.6 for fully battery-powered aircraft. This substantial range underscores the importance of including the EMF as a critical factor in the calculation of the Overall Equipment Mass (OEM) (see Eq. 6.7). Furthermore, for aircraft without batteries, the EMF for fully hydrogen fuel cell aircraft is one-quarter that of conventional kerosene aircraft, due to hydrogen's higher specific energy.

Kerosene Mass and CO₂ Emissions Fig. 9.10 illustrates the normalized kerosene consumption results, relative to conventional kerosene aircraft. Since kerosene is the sole chemical species in the considered powertrain capable of emitting CO₂, identical trends would be observed for CO₂ emissions. Kerosene consumption decreases linearly with increasing Φ_{Bat} or Φ_{H2} , albeit at different rates. This indicates that while the added weight of the batteries is substantial, it does not necessitate a proportionally larger kerosene load to compensate for the batteries themselves. Indeed, kerosene usage decreases more rapidly for hydrogen-powered aircraft than for battery-powered aircraft. This is because the TOM does not exhibit as sharp an increase as observed in battery-powered aircraft.

Energy Consumption

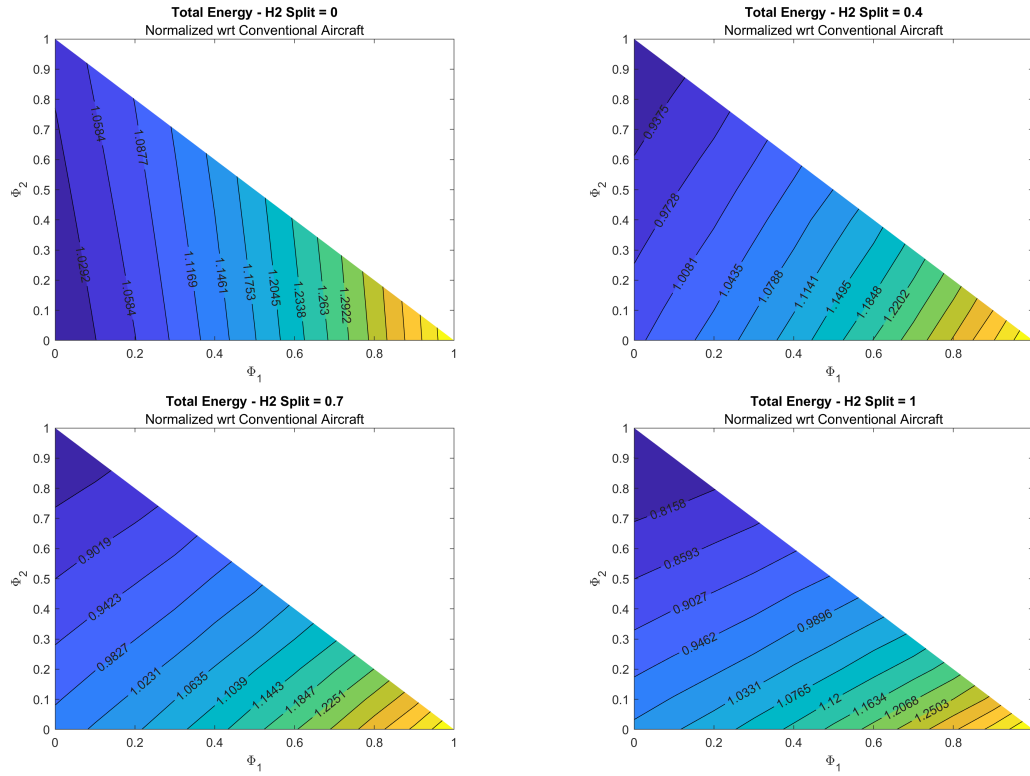


Figure 9.8: Total energy consumption results for varying H₂ split fractions (normalised to the energy consumption for conventional kerosene aircraft)

Energy Mass Fraction

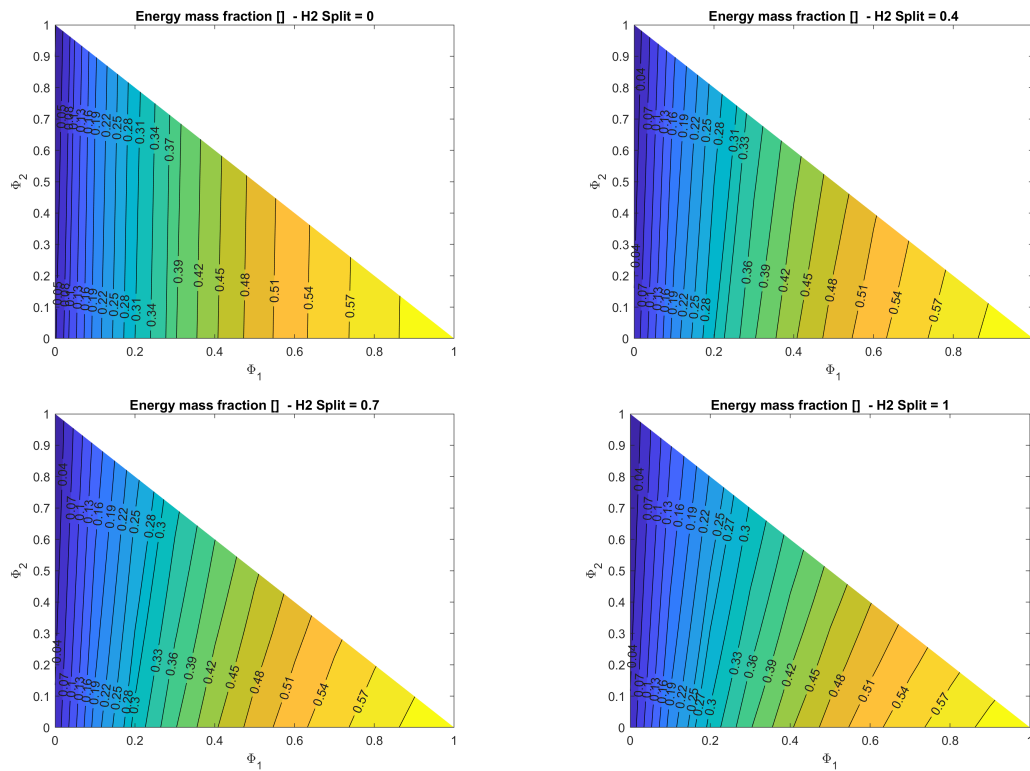


Figure 9.9: Energy mass fraction results for varying H₂ split fractions

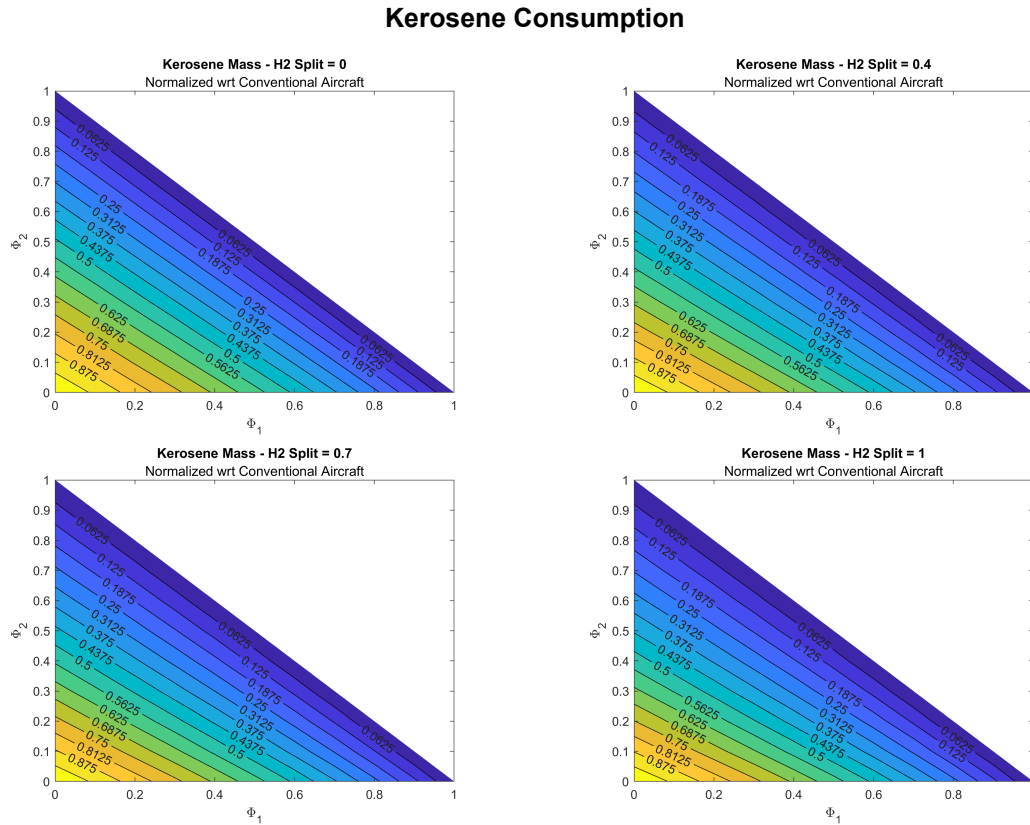


Figure 9.10: Kerosene consumption results for varying H_2 split fractions (normalised to the kerosene consumption for conventional kerosene aircraft)

NO_x Emissions Since NO_x emissions are determined solely by the quantity and type of fuel combusted, an examination of Fig. 9.11 reveals that emissions peak for the conventional kerosene aircraft. Conversely, fully hydrogen combustion enables a reduction of approximately 60% in these emissions, even though the Emission Index (EI) for hydrogen is higher than that of kerosene. This is because the total mass of hydrogen burned is lower than that of kerosene, resulting in lower NO_x emissions.

As H_{2split} increases, less hydrogen is directed to the gas turbine, causing the iso- NO_x lines to change both slope and magnitude with increasing Φ_{H_2} . At $H_{2split} = 1$, both $\Phi_{Bat} = 1$ and $\Phi_{H_2} = 1$ correspond to the absence of NO_x emissions.

Cumulative (direct) emissions In conclusion, Fig. 9.12 presents the cumulative emissions, from which the following conclusions can be drawn. First, it is evident that several configurations can be employed to reduce overall direct emissions compared to conventional kerosene-powered aircraft. As expected, the fully battery-electric aircraft exhibits zero direct emissions. Analysis of hydrogen's impact reveals that its combustion results in a 75% reduction in emissions compared to conventional kerosene. A more significant reduction is observed with the integration of a fuel cell, which, due to the absence of NO_x emissions and a halved H_2O Emission Index (compared to H_2 combustion), results in near-zero emissions.

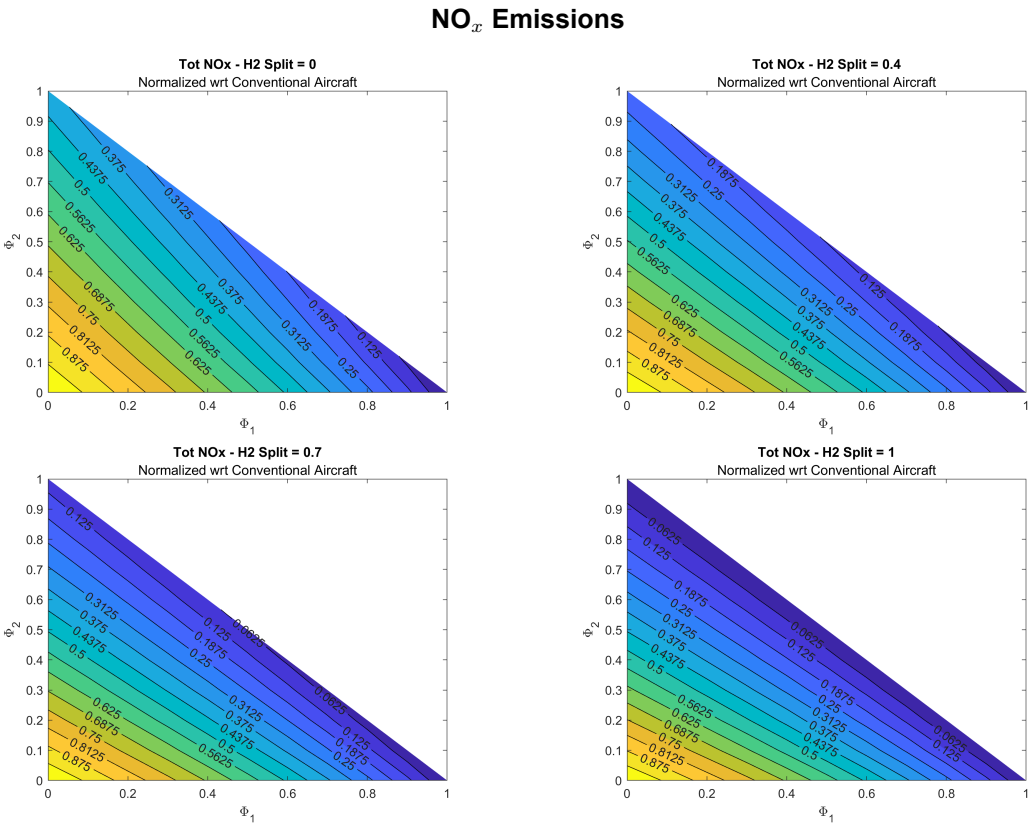


Figure 9.11: NO_x emissions result for varying H₂ split fractions (normalised to NO_x emissions for conventional kerosene aircraft)

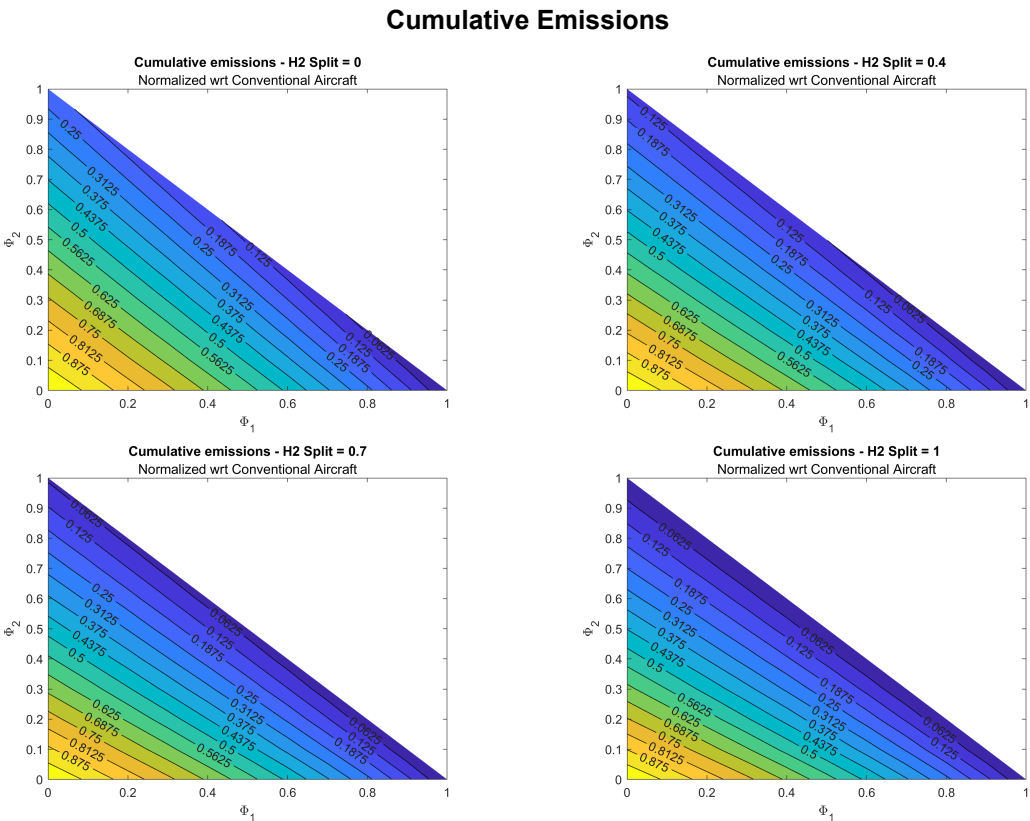


Figure 9.12: Cumulative emissions results for varying H₂ split fractions (normalised to the emissions for conventional kerosene aircraft)

10

Analysis of Future Trends for Double-Hybrid Aircraft Drivers

In the previous chapter, several key drivers for a Double-Hybrid Aircraft were outlined, including battery specific energy and component efficiency. In this final chapter, a study of potential future trends for some of these drivers is conducted. The focus is twofold: first, to examine how the minimum energy consumption point shifts within the power ratio design space (Fig. 9.1), and second, to analyse how the Key Performance Indicators (KPIs) associated with this new minimum energy consumption point change relative to the baseline technology.

10.1. Brake Specific Fuel Consumption

Kerosene-powered aircraft, and consequently gas turbine engines, have seen a dramatic reduction in specific fuel consumption over the last decade due to increased compression ratios and turbine inlet temperatures. A sensitivity analysis was performed to evaluate the effect of a 50% reduction in BSFC, relative to the baseline.

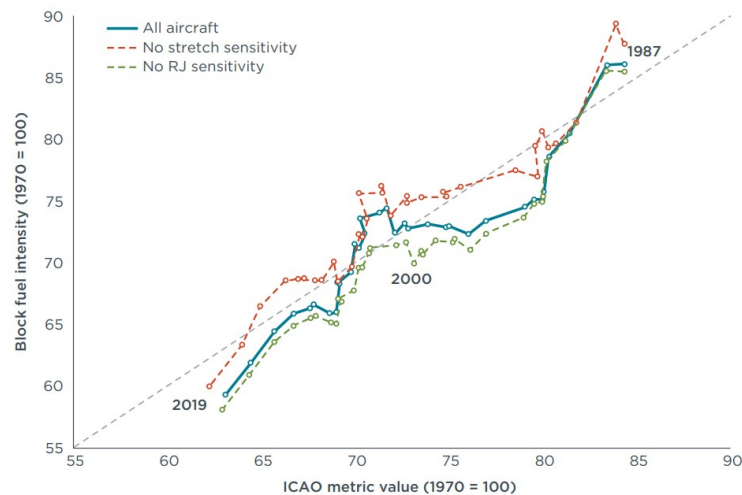


Figure 10.1: Block fuel trend in the last 50 years for kerosene aircraft. Source: [54]

The following table and figure present the minimum energy consumption points across the power ratio design space.

It is notable that the combination of the three parameters remains the same as the baseline, representing the most efficient configuration, until the gas turbine becomes more efficient than the fuel cell. As

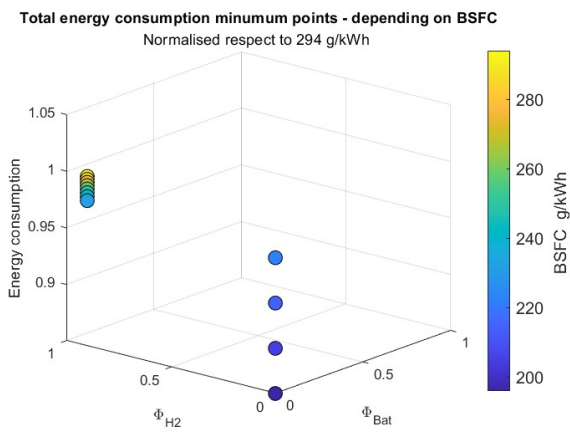


Figure 10.2: Total energy consumption minimum points-depending on brake specific fuel consumption - represented in power control parameters diagram

BSFC [g/kWh]	Φ_{Bat}	Φ_{H2}	$H2_{Split}$
294	0	0.9	1
285	0	0.9	1
276	0	0.9	1
267	0	0.9	1
258	0	0.9	1
249	0	0.9	1
241	0	0.9	1
232	0	0.9	1
223	0	0	0
214	0	0	0
205	0	0	0
196	0	0	0

Table 10.1: Power control parameters for minimum energy consumption, depending on brake specific fuel consumption of the gas turbine engine

observed in the previous chapter, considering a pure gas turbine configuration, conventional kerosene-fuelled aircraft result in lower energy consumption compared to hydrogen combustion aircraft.

Analysing KPI trends, beyond the obvious overall energy consumption reduction, a similar trend is observed for both power ratio combinations individually. This trend consists of a general reduction in Take-Off Mass (TOM), wingspan, and energy mass fraction. Beyond this trend within a constant power ratio combination, the transition point between the two power ratio combinations is of particular interest. As shown in Fig. 10.3, cumulative emissions and energy mass fraction exhibit a significant jump due to the switch from hydrogen to kerosene, while TOM and wingspan show a noticeable decrease, albeit smaller in magnitude compared to the first two indicators.

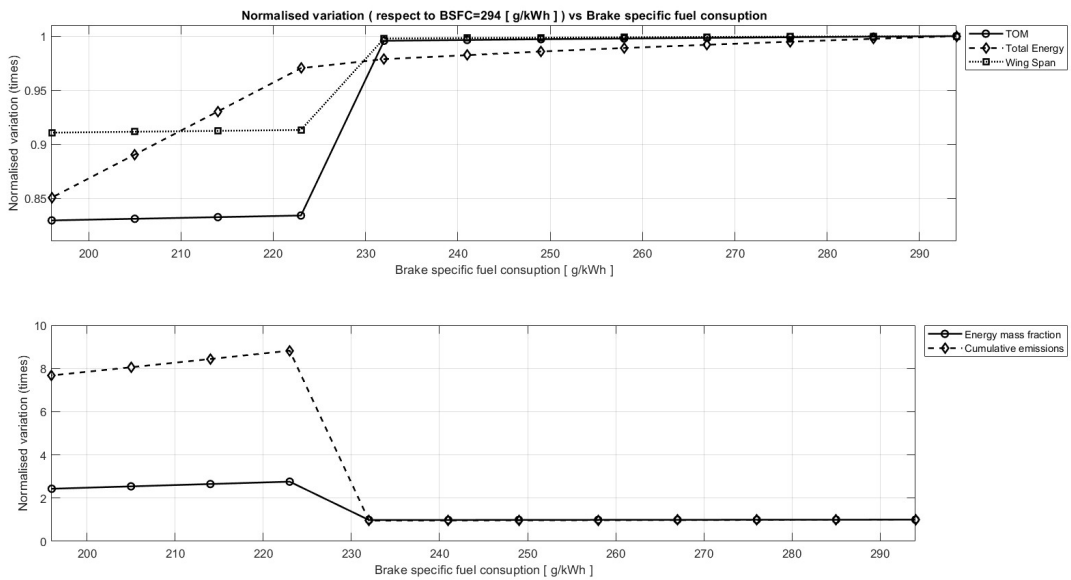


Figure 10.3: KPIs variation depending on BSFC, respect to $BSFC = 294 \text{ g/kWh}$

10.2. Fuel Cell Efficiency

In Section 4.4, the fuel cell sizing process and performance evaluation were examined. In particular, Fig. 4.12 shows the overall efficiency of the fuel cell system, ranging from 55% to 35% depending on power output and flight conditions. Considering future developments in this technology, a sensitivity analysis was conducted, varying fuel cell efficiency between 35% and 60%.

Decreasing fuel cell system efficiency relative to the baseline (50%), its use remains advantageous in terms of energy consumption until the difference between gas turbine and fuel cell efficiency decreases to a point where carrying the hydrogen fuel system is no longer beneficial. Conversely, with higher efficiency than the baseline, the most energy-efficient powertrain becomes a fully fuel cell-based system.

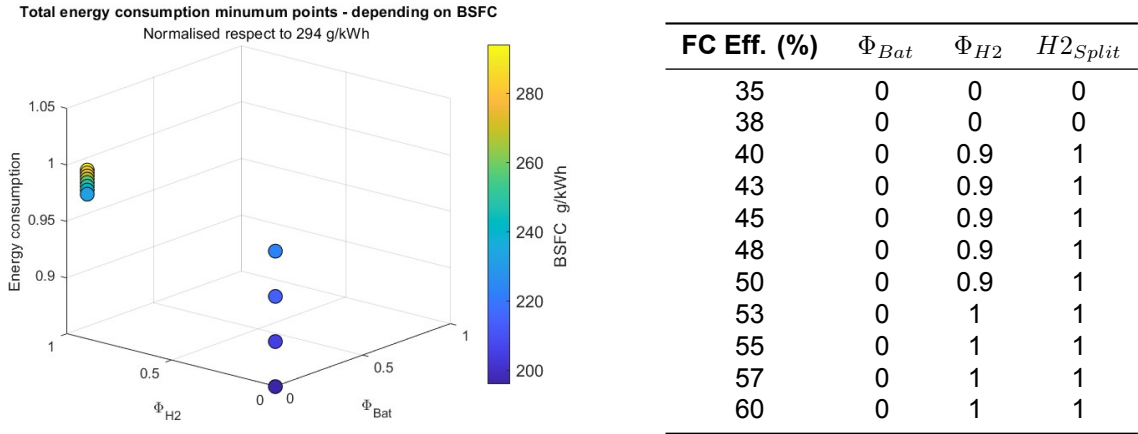


Figure 10.4: Total energy consumption minimum points- depending on fuel cell efficiency - represented in power control parameters diagram

Table 10.2: Power control parameters for minimum energy consumption, depending on fuel cell efficiency

Analysing the KPIs, a similar trend to the BSFC analysis is observed. Conventional kerosene-fuelled configurations exhibit significantly higher cumulative emissions, energy consumption, and energy mass fraction, but lower TOM and wingspan. When the aircraft is fully fuel cell-powered, total energy consumption is lowest, and consequently, total emissions drop due to the absence of kerosene combustion, as does the energy mass fraction. No relevant changes are observed regarding TOM and wingspan.

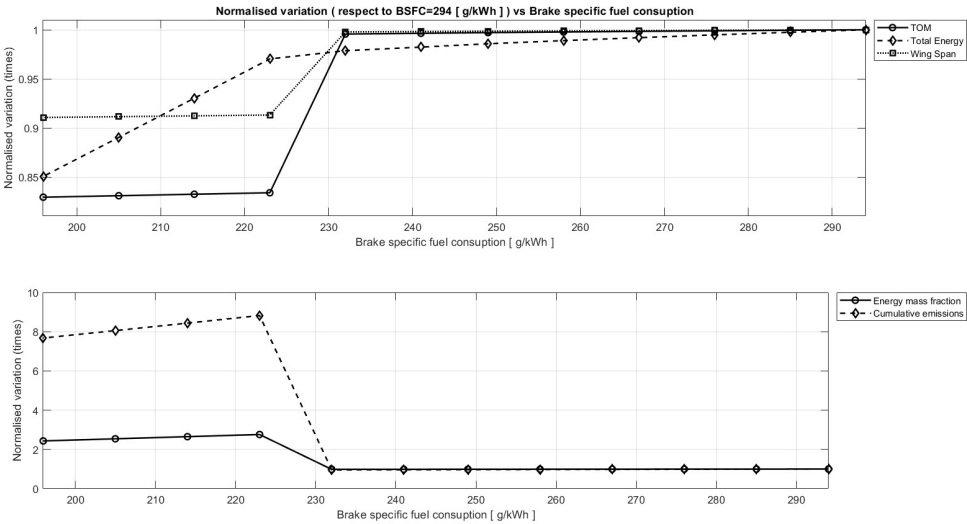


Figure 10.5: KPIs variation depending on Fuel cell efficiency, respect to $\eta_{FC} = 50\%$

10.3. Battery Specific Energy

Perhaps the most compelling sensitivity analysis result concerns battery specific energy. As reported by Ricci [40], a near-linear improvement in battery specific energy is expected in the coming years. The baseline value for battery specific energy in this work is 340 Wh/kg, corresponding to the reported 2024 value. A sensitivity analysis is carried out, considering a 50% improvement in battery specific energy, equivalent to 510 Wh/kg.

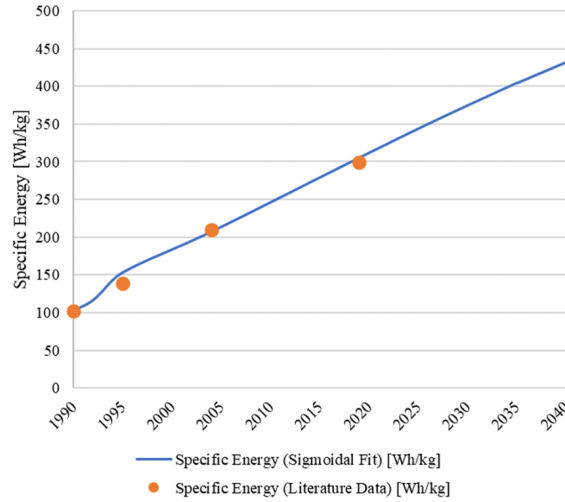


Figure 10.6: Specific Energy [Wh/kg] trend of EV Lithium-Ion Batteries (Blue line) from literature data (Orange dots). Source: [40]

As shown in Fig. 10.7, the minimum energy consumption power ratio combinations gradually increase the battery power ratio Φ_{Bat} until reaching a specific energy that enables a fully battery-electric configuration to be more energy efficient. While the specific energy of batteries, even in the best-case scenario, remains much lower than that of hydrogen, the overall propulsive efficiency (η_{PT}) of a fully battery-electric aircraft is double that of the baseline fuel cell aircraft.

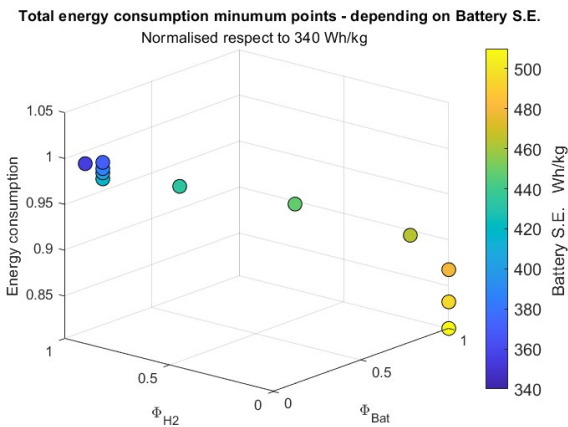


Figure 10.7: Total energy consumption minimum points-depending on battery specific energy - represented in power control parameters diagram

S.E. Bat. [Wh/kg]	Φ_{Bat}	Φ_{H2}	$H2_{Split}$
340	0	0.9	1
355	0	0.9	1
371	0.1	0.9	1
386	0.1	0.9	1
402	0.1	0.9	1
417	0.1	0.9	1
433	0.3	0.7	1
448	0.6	0.4	1
464	0.9	0.1	1
479	1	0	0
495	1	0	0
510	1	0	0

Table 10.3: Power control parameters for minimum energy consumption, depending on battery specific energy

Regarding KPI analysis, several interesting trends are observed:

- Cumulative emissions drop as soon as kerosene is no longer used, reaching zero for the fully battery-electric configuration.
- TOM increases every time the battery power ratio Φ_{Bat} rises. However, increasing the battery specific energy, while Φ_{Bat} remains constant, decreases TOM as battery weight decreases.

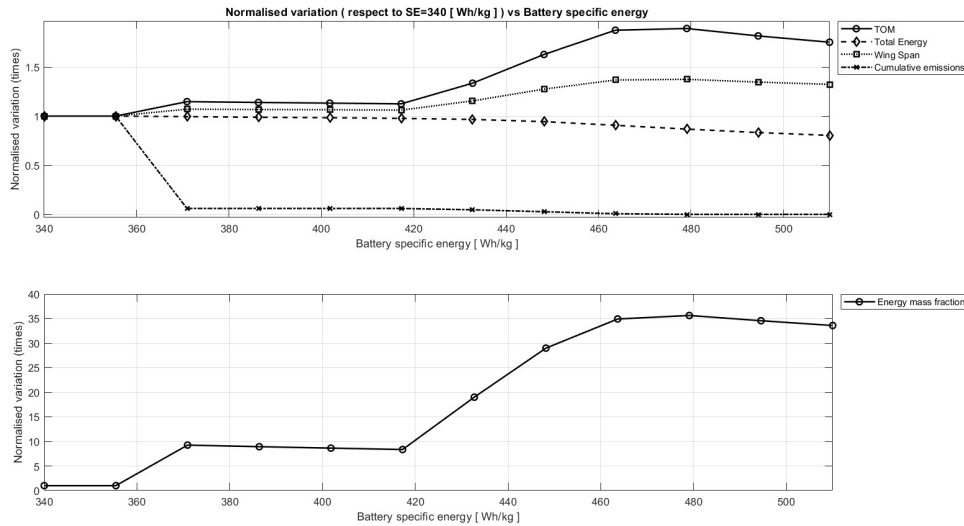


Figure 10.8: KPIs variation depending on Battery Specific Energy, respect to $SE_{Bat} = 340 Wh/kg$

- Energy mass fraction (EMF) follows the same trend as TOM, but with larger changes, as the energy mass increases more sharply than TOM when adding batteries to the aircraft (see Fig. 10.8).

10.4. Gravimetric Index

The Gravimetric Index (GI) is the most common metric for evaluating hydrogen fuel system weight during conceptual design. Due to the limited number of hydrogen-powered aircraft currently in operation, its uncertainty remains relatively high. This sensitivity analysis evaluates the GI's impact on overall aircraft KPIs, considering a 50% improvement or reduction relative to the baseline value of $GI = 0.3$.

Total energy consumption minimum points - depending on Gravimetric Index
Normalised respect to 0.35

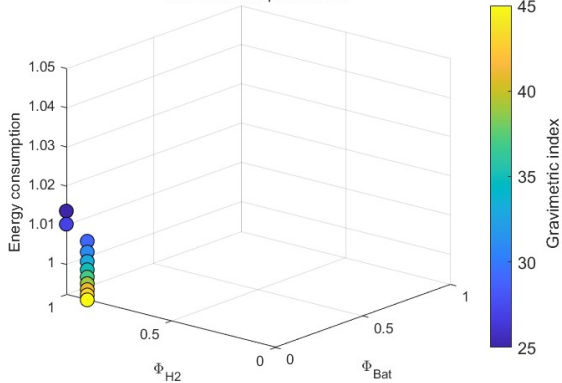


Figure 10.9: Total energy consumption minimum points depending on gravimetric index of the hydrogen fuel system - represented in power control parameters diagram

GI	Φ_{Bat}	Φ_{H2}	$H2_{Split}$
0.25	0	1	1
0.27	0	1	1
0.29	0	0.9	1
0.31	0	0.9	1
0.33	0	0.9	1
0.35	0	0.9	1
0.37	0	0.9	1
0.39	0	0.9	1
0.41	0	0.9	1
0.43	0	0.9	1
0.45	0	0.9	1

Table 10.4: Power control parameters for minimum energy consumption, gravimetric index of the hydrogen fuel system

The results are both interesting and somewhat counter-intuitive. As shown in Fig. 10.4, the total energy consumption variation is on the order of a few percentage points, increasing or decreasing as the GI increases or decreases, respectively. This is because the weight of the stored hydrogen (approximately 300 kg) is two orders of magnitude lower than the Take-Off Mass (TOM). Consequently, the additional or reduced weight of the hydrogen fuel system (approximately 200 kg) does not have a large impact on the overall energy consumption.

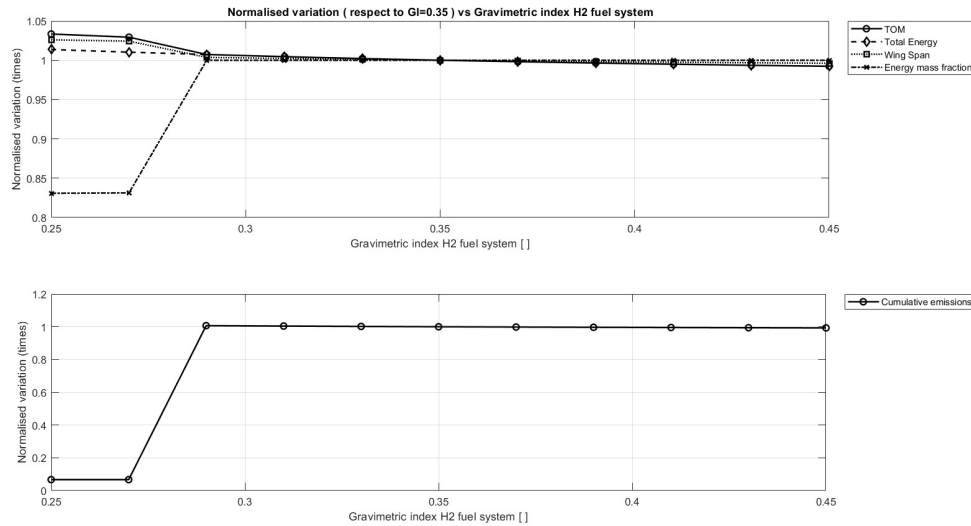


Figure 10.10: KPIs variation depending on Gravimetric Index, respect to $GI = 0.35$

Secondly, it is observed that as the GI decreases, below a certain threshold, the most fuel-efficient solution becomes the full hydrogen fuel cell configuration. This result is counter-intuitive and depends on two factors:

- i As observed in Fig. 9.8, when the $H2_{split}$ parameter is equal to or nearly equal to one, the minimum energy consumption can be associated with a range of configurations, not just a single one. This range spans from a fully hydrogen fuel cell aircraft to a combination involving kerosene combustion and batteries.
- ii In this study, the fuel cell is considered significantly more energy-efficient than the gas turbine engine. As the GI decreases and TOM increases, the added weight is compensated for by the higher energy efficiency of the fuel cell system.

Overall, this sensitivity analysis, rather than focusing solely on how the least energy-consuming configuration shifts across the power ratio design space, is more insightful in showing that for this type of aircraft with a relatively low hydrogen weight, the gravimetric index does not have a large impact on either energy consumption or KPIs parameters (Fig. 10.10).

Conclusion and Future Development

Conclusion This thesis demonstrates that the introduction of a Double-Hybrid Powertrain (combining hydrogen and kerosene combustion with fuel cell and battery technologies) on board a regional aircraft can significantly reduce both energy consumption and environmental impact.

First, it has been shown that 28 different powertrain configurations can be defined with these components, compared to the nine configurations identified in existing literature. Furthermore, an additional powertrain operating mode was defined, expanding upon those previously reported.

Regarding powertrain modelling, the double-hybrid powertrain introduces twice the number of Degree of Hybridization (DOH) parameters, along with an additional parameter to determine the hydrogen split between the fuel cell and gas turbine engine. This increased number of DOH parameters adds complexity and increases the likelihood of encountering singular cases in the powertrain system equations due to the inherent definition of DOH itself.

In terms of the conceptual design process, once the DOH parameters are defined, the main challenge lies in developing a method to define constraint diagrams for each powertrain component and an equation to estimate the Operative Empty Mass (OEM) that accounts for the different energy densities of the various power sources.

A sensitivity analysis across the power ratio design space revealed that a minimum energy consumption region is identified where the fuel cell provides approximately 80-90 percent of the total power, with the remaining assigned to either kerosene or battery. This solution would also reduce dramatically environmental impact, while only slightly increasing TOM compared to conventional kerosene-fuelled aircraft. Although not the primary focus of this study, this configuration would also allow the powertrain to be more responsive to abrupt energy requirement transients. Additionally, it would enable the fuel cell system to be sized based on cruise power requirements, resulting in a lighter and more efficient fuel cell system.

A fully battery-electric aircraft configuration would only become the ideal solution in terms of energy efficiency with substantial improvements in battery energy density, probably not achievable in the next 20–30 years.

Future Development Regarding the developed Class1 Double-Hybrid modelling and conceptual design method, the following areas are identified for future research and development:

- i **Improved Powertrain Modelling:** This study has highlighted limitations in hybrid powertrain modelling based on powertrain equations. Future models should address singularities associated with certain operating modes and facilitate easier definition of these modes.
- ii **Fuel cell and Gas-turbine engine map:** Incorporating real gas turbine engine and fuel cell efficiency maps, rather than assuming constant values throughout the mission, would enhance model accuracy.

- iii **Mission-Optimized Power Control:** Evaluating optimal power control parameters for each mission segment, rather than focusing solely on cruise, would allow for segment-specific optimization.
- iv **Distributed Propulsion:** Investigating the impact of distributed propulsion on the regional aircraft case study, including how and if it affects the minimum energy consumption region, is a promising avenue for further research.

References

- [1] R. Barron. *Cryogenic Systems*. 2nd. Oxford University Press, 1985.
- [2] Stefano Boggia and Anthony Jackson. "Some unconventional aero gas turbines using hydrogen fuel". In: *ASME Turbo Expo 2002: Power for Land, Sea, and Air*. American Society of Mechanical Engineers Digital Collection, 2002, pp. 683–690. DOI: 10.1115/GT2002-30412. URL: <http://dx.doi.org/10.1115/GT2002-30412>.
- [3] V. Bonnin and M. Hoogreef. "Sensitivity study & MDO results part 1". In: *CHYLA Workshop Southampton*. Southampton, UK, Feb. 2023. DOI: 10.5281/zenodo.7875784. URL: <https://doi.org/10.5281/zenodo.7875784>.
- [4] Marty K. Bradley and Christopher K. Droney. *Subsonic Ultra Green Aircraft Research: Phase II – Volume II – Hybrid Electric Design Exploration*. Tech. rep. Huntington Beach, California: Boeing Research and Technology, 2015.
- [5] Joseph Brand et al. "Potential Use of Hydrogen In Air Propulsion". In: *AIAA International Air and Space Symposium and Exposition: The Next 100 Years*. 2003. DOI: 10.2514/6.2003-2879. eprint: <https://arc.aiaa.org/doi/pdf/10.2514/6.2003-2879>. URL: <https://arc.aiaa.org/doi/abs/10.2514/6.2003-2879>.
- [6] Joseph Brand et al. "Potential use of hydrogen in air propulsion". In: *AIAA International Air and Space Symposium and Exposition: The Next 100 Years*. American Institute of Aeronautics and Astronautics. 2003. DOI: 10.2514/6.2003-2879. URL: <http://dx.doi.org/10.2514/6.2003-2879>.
- [7] G.D. Brewer. *Hydrogen Aircraft Technology*. 1st. Boca Raton, FL, USA: CRC Press, 1991.
- [8] CAO Aircraft Engine Emissions Databank. EASA. URL: <https://www.easa.europa.eu/en/domains/environment/icao-aircraft-engine-emissions-databank> (visited on 01/09/2024).
- [9] Durgesh Chandel et al. "Conceptual Design of Distributed Electrified Boundary Layer Ingesting Propulsors for the CHEETA Aircraft Concept". In: *AIAA Propulsion and Energy 2021 Forum*. American Institute of Aeronautics and Astronautics. 2021. DOI: 10.2514/6.2021-2879. URL: <http://dx.doi.org/10.2514/6.2021-2879>.
- [10] Maria Chiara Massaro et al. "Optimal design of a hydrogen-powered fuel cell system for aircraft applications". In: *Energy Conversion and Management* 306 (2024), p. 118266. ISSN: 0196-8904. DOI: <https://doi.org/10.1016/j.enconman.2024.118266>. URL: <https://www.sciencedirect.com/science/article/pii/S0196890424002073>.
- [11] Clean Aviation. *AMBER: Advancing Hybrid Electric Propulsion*. <https://www.clean-aviation.eu/amber-advancing-hybrid-electric-propulsion>. Accessed: 2024-09-12. Accessed 2024.
- [12] Clean Hydrogen JU. *SRIA Key Performance Indicators (KPIs)*. Online. Accessed: Nov. 30, 2023. 2023. URL: https://www.clean-hydrogen.europa.eu/knowledgemanagement/strategy-map-and-key-performance-indicators/clean-hydrogen-jusria-key-performance-indicators-kpis_en.
- [13] McKinsey Company. *Hydrogen-powered aviation: A fact-based study of hydrogen technology, economics, and climate impact by 2050*. First edition. ©Clean Sky 2 JU and ©FCH 2 JU, 2020. Luxembourg: Publications Office of the European Union, 2020. ISBN: 978-92-9246-341-0. DOI: 10.2843/766989. URL: <https://doi.org/10.2843/766989>.
- [14] Wikipedia contributors. *Proton-exchange membrane fuel cell* — *Wikipedia, The Free Encyclopedia*. Accessed: September 26, 2024. 2024. URL: https://en.wikipedia.org/wiki/Proton-exchange_membrane_fuel_cell.

- [15] G. Corchero and J.L. Montañés. "An approach to the use of hydrogen for commercial aircraft engines". In: *Proceedings of the Institution of Mechanical Engineers, Part G: Journal of Aerospace Engineering* 219.1 (2005), pp. 35–44. ISSN: 0954-4100. DOI: 10.1243/095441005X9139. URL: <http://dx.doi.org/10.1243/095441005X9139>.
- [16] A.L. Dicks and D.A.J. Rand. *Fuel Cell Systems Explained*. 3rd. Chichester, England: John Wiley & Sons Inc, 2018. ISBN: 978-1-11-870699-2. DOI: RyXRyykfNd3RRR3dyeNNk.
- [17] D. DuBois and G.C. Paynter. "Fuel Flow Method2 for Estimating Aircraft Emissions". In: *SAE Transactions* 115 (2006), pp. 1–14.
- [18] European Union Aviation Safety Agency. *Type-Certificate Data Sheet No. E.004 for CFM56-7B Series Engines*. <https://www.easa.europa.eu/en/downloads/7795/en>. Accessed: September 12, 2024.
- [19] Antonio Filippone and Nicholas Bojdo. "Statistical Model for Gas Turbine Engines Exhaust Emissions". In: *Transportation Research Part D: Transport and Environment* 59 (2018), pp. 451–463. DOI: \.
- [20] D.F. Finger et al. "A Comparison of Hybrid-Electric Aircraft Sizing Methods". In: 2020. DOI: 10.2514/6.2020-1006.
- [21] H. Funke, N. Beckmann, and S. Abanteriba. "An overview on dry low NO_x micromix combustor development for hydrogen-rich gas turbine applications". In: *International Journal of Hydrogen Energy* 44 (2019), pp. 6978–6990. DOI: 10.1016/j.ijhydene.2019.01.161.
- [22] Arturo Gomez and Howard Smith. "Liquid hydrogen fuel tanks for commercial aviation: Structural sizing and stress analysis". In: *Aerospace Science and Technology* 95 (2019), p. 105438. ISSN: 1270-9638. DOI: <https://doi.org/10.1016/j.ast.2019.105438>. URL: <https://www.sciencedirect.com/science/article/pii/S1270963818304139>.
- [23] Mohammed Hassan et al. "Framework Development for Performance Evaluation of the Future National Airspace System". In: June 2015.
- [24] R.G. Helenbrook and J.Z. Colt. *Development and validation of purged thermal protection systems for liquid hydrogen fuel tanks of hypersonic vehicles*. Tech. rep. Prepared for Langley Research Center, National Aeronautics and Space Administration, Washington, D.C. Buffalo, NY: Bell Aerospace, 1977.
- [25] Philip G. Hill and Carl R. Peterson. *Mechanics and Thermodynamics of Propulsion*. 1992.
- [26] Hydrogen Aero. *Hydrogen Aero Product Information*. <https://hydrogen.aero/product/>. Accessed: September 26, 2024.
- [27] International Council on Clean Transportation (ICCT). *Performance analysis of evolutionary hydrogen-powered aircraft*. White Paper. A4-v4. International Council on Clean Transportation (ICCT), 2022. URL: <https://theicct.org/wp-content/uploads/2022/01/LH2-aircraft-white-paper-A4-v4.pdf>.
- [28] A. T. Isikveren et al. "Pre-design strategies and sizing techniques for dual-energy aircraft". In: *Aircraft Engineering and Aerospace Technology: An International Journal* 86.6 (2014), pp. 525–542. DOI: 10.1108/AEAT-08-2014-0122.
- [29] Tim Kadyk et al. "Analysis and design of fuel cell systems for aviation". In: *Energies* 11.2 (2018), p. 375. DOI: 10.3390/en11020375.
- [30] L. M. Lorenz and M. M. Cameron. "Introduction." In: *CABI* (2013), pp. 1–9. DOI: 10.1079/9781845939861.0001. URL: <https://doi.org/10.1079/9781845939861.0001>.
- [31] magniX. *magniX Powertrains*. <https://www.magnix.aero/powertrains>. Accessed: September 12, 2024.
- [32] Maria Chiara Massaro et al. "Potential and technical challenges of on-board hydrogen storage technologies coupled with fuel cell systems for aircraft electrification". In: *Journal of Power Sources* 555 (2023), p. 232397. ISSN: 0378-7753. DOI: <https://doi.org/10.1016/j.jpowsour.2022.232397>. URL: <https://www.sciencedirect.com/science/article/pii/S037877532201374X>.

- [33] Jayant Mukhopadhyaya and Dan Rutherford. *Performance analysis of evolutionary hydrogen-powered aircraft*. Accessed: 2022-01-26. Jan. 2022. URL: <https://theicct.org/publication/aviation-global-evo-hydrogen-aircraft-jan22/>.
- [34] Engineering National Academies of Sciences and Medicine. *Commercial Aircraft Propulsion and Energy Systems Research: Reducing Global Carbon Emissions*. Washington, DC: The National Academies Press, 2016. ISBN: 978-0-309-44096-7. DOI: 10.17226/23490. URL: <https://nap.nationalacademies.org/catalog/23490/commercial-aircraft-propulsion-and-energy-systems-research-reducing-global-carbon>.
- [35] R. O'Hayre et al. *Fuel Cell Fundamentals*. 3rd. Chichester, England: John Wiley & Sons Inc, 2016. ISBN: 978-1-5231-1024-7.
- [36] G. Onorato, P. Proesmans, and M.F.M. Hoogreef. "Assessment of hydrogen transport aircraft: Effects of fuel tank integration". In: *CEAS Aeronautical Journal* (2022). Flight Performance and Propulsion - Aerospace Engineering, TU Delft. DOI: 10.1007/s13272-022-00601-6.
- [37] T. Oom Ortiz de Montellano. "Structural Analysis of a New Integral Tank Concept for Hydrogen Storage On-board Commercial Aircraft". Master's thesis. MA thesis. Delft University of Technology, 2024. URL: <http://resolver.tudelft.nl/uuid:8ab68eb3-77dc-4acf-9768-6b379b8ef24d>.
- [38] Francesco Orefice et al. "Aircraft Conceptual Design of Commuter Aircraft Including Distributed Electric Propulsion". In: *AIAA 2020 (American Institute of Aeronautics and Astronautics)*. AIAA SciTech Forum. 2020. DOI: 10.2514/6.2020-2627. URL: <https://doi.org/10.2514/6.2020-2627>.
- [39] PowerCell Website. *p-stack-v-222*. Online. Accessed: 11/09/2024. URL: <https://powercellgroup.com/fuel-cell-stacks/>.
- [40] V. Ricci, P. Romano, and N. Stampone. "Estimate of Economic Impact of EVs Li-ion Batteries Recovery". In: *Clean Energy and Sustainability* 1.1 (2023), p. 10005. DOI: 10.35534/ces.2023.10005.
- [41] Rotrex Website. *EK40 fuel cell compressor*. Online. Accessed: September 11, 2024. URL: <https://rotrex-fuel-cell-compressor.com/fuel-cell-compressors/>.
- [42] M. A. Saez Ortuño et al. "Climate Assessment of Hydrogen Combustion Aircraft: Towards a Green Aviation Sector". In: *AIAA SciTech Forum and Exposition, 2023*. AIAA SciTech Forum 2023 Article AIAA 2023-2513. 2023. DOI: 10.2514/6.2023-2513. URL: <https://doi.org/10.2514/6.2023-2513>.
- [43] M. Schmelcher and J. Haßy. "Hydrogen fuel cells for aviation? A potential analysis comparing different thrust categories". In: *ISABE 2022*. Ottawa, Canada, Sept. 2022.
- [44] P. Sharke. "H2 tank testing". In: *Mechanical Engineering - CIME* 126.4 (2004).
- [45] SkySpark Project. *SkySpark Project Website*. Accessed: September 5, 2024. URL: <http://www.skyspark.eu/web/ita/index.php>.
- [46] E. Torenbeek. *Advanced aircraft design: conceptual design, analysis and optimization of subsonic civil airplanes*. John Wiley & Sons, 2013.
- [47] D. Verstraete et al. "Hydrogen as an aero engine fuel". In: *17th International Symposium on Airbreathing Engines (ISABE)*. ISABE-2005-1212, Munich, Germany. 2005.
- [48] Dries Verstraete. "The Potential of Liquid Hydrogen for Long Range Aircraft Propulsion". Doctoral dissertation. PhD thesis. Cranfield University, 2009. URL: <http://hdl.handle.net/1826/4089>.
- [49] Nicole Viola et al. *Slide Package 11: Propellant System Design*. Politecnico di Torino, Dipartimento di Ingegneria Meccanica e Aerospaziale, Team 1, Course: Design of Integrated Aerospace Systems. Oct. 2023.
- [50] R. de Vries. "Hybrid-Electric Aircraft with Over-the-Wing Distributed Propulsion: Aerodynamic Performance and Conceptual Design". [Dissertation (TU Delft)]. Dissertation. Delft University of Technology, 2022. DOI: 10.4233/uuid:ef87dc11-e7b2-4726-a41f-28588d64c58d. URL: <https://doi.org/10.4233/uuid:ef87dc11-e7b2-4726-a41f-28588d64c58d>.

- [51] Jason R. Welstead and James L. Felder. "Subsonic Ultra Green Aircraft Research: Phase II – Volume II – Hybrid Electric Design Exploration". In: *2016 AIAA SciTech Conference*. Work of the US Gov. Public Use Permitted. San Diego, CA, United States: American Institute of Aeronautics and Astronautics, Jan. 2016. URL: <https://ntrs.nasa.gov/citations/20160007674>.
- [52] Andrew S. White et al. "System-Level Utilization of Low-Grade, MW-Scale Thermal Loads for Electric Aircraft". In: *AIAA Aviation 2022 Forum*. American Institute of Aeronautics and Astronautics. 2022. DOI: 10.2514/6.2022-3291. URL: <http://dx.doi.org/10.2514/6.2022-3291>.
- [53] R. E. Wolleswinkel et al. "A new perspective on battery-electric aviation, Part I: Reassessment of achievable range". In: *AIAA SciTech Forum (AIAA 2024-1489)*. American Institute of Aeronautics and Astronautics Inc. (AIAA). 2024. DOI: 10.2514/6.2024-1489.
- [54] Xinyi Sola Zheng and Dan Rutherford. *Fuel Burn of New Commercial Jet Aircraft: 1960 to 2019*. Tech. rep. International Council on Clean Transportation (ICCT), 2019. URL: <https://theicct.org/publication/fuel-burn-of-new-commercial-jet-aircraft-1960-to-2019/>.